California State University, Monterey Bay

Digital Commons @ CSUMB

Capstone Projects and Master's Theses

Spring 2016

Tracking Icebergs and Sea Ice in the Mid-Pleistocene Bering Sea Suggests Sea Ice Affects Ice Sheet Growth

Vera Jesser Lawson
California State University, Monterey Bay

Follow this and additional works at: https://digitalcommons.csumb.edu/caps_thes

TRACKING ICEBERGS AND SEA ICE IN THE MID-PLEISTOCENE

BERING SEA SUGGESTS SEA ICE AFFECTS ICE SHEET GROWTH

_____

A Thesis

Presented to the

Faculty of the

Moss Landing Marine Laboratories

California State University Monterey Bay

_____

In Partial Fulfillment

of the Requirements for the Degree

Master of Science

in

Marine Science

_____

by

Vera Jesser Lawson

May 2016

CALIFORNIA STATE UNIVERSITY MONTEREY BAY

The Undersigned Faculty Committee Approves the

Thesis of Vera Jesser Lawson:

TRACKING ICEBERGS AND SEA ICE IN THE MID-PLEISTOCENE

BERING SEA SUGGESTS SEA ICE AFFECTS ICE SHEET GROWTH

_____
Ivano W. Aiello, Chair
San Jose State University, Moss Landing Marine Laboratories

_____
Kenneth H. Coale
San Jose State University, Moss Landing Marine Laboratories

_____
A. Christina Ravelo
University of California Santa Cruz, Ocean Sciences Department

_____
Kris Roney, Dean
Associate VP for Academic Programs and Dean of Undergraduate and Graduate Studies

_____
Approval Date

DEDICATION

I was four when my father took me on my first geology field trip; he was looking for gravel to build a road through the Chapare in the Bolivian jungle. It was he who years later in the early 70's took me to a lecture on plate tectonics by a visiting lecturer on the Princeton University campus. I also remember one day when he came home from work amazed at learning that an underwater landslide had sequentially and quickly broken telegraph lines in the Atlantic. As a civil engineer with a master's degree in soils, he instilled in me a curiosity about the physical world around me. I would have loved to have discussed this thesis with him because I now realize we would have had a lot to talk about. Sadly, he passed away the year before I began attending classes at Moss Landing Marine Laboratories. This thesis is dedicated to the memory of my father, Richard W. B. Jesser, Sr.

"God thunders wondrously with his voice;

he does great things that we cannot comprehend.

For to the snow he says, 'Fall on the earth',

likewise to the downpour, his mighty downpour.

He seals up the hand of every man,

that all men whom he made may know it.

Then the beasts go into their lairs,

and remain in their dens.

From its chamber comes the whirlwind,

and cold from the scattering winds.

By the breath of God ice is given,

and the broad waters are frozen fast.

He loads the thick cloud with moisture;

the clouds scatter his lightning.

They turn around and around by his guidance,

to accomplish all that he commands them

on the face of the inhabitable world."

Elihu the son of Barachel the Buzite

Job 37:5-12, English Standard Version

ABSTRACT

Tracking Icebergs and Sea Ice in the Mid-Pleistocene Bering Sea
Suggests Sea Ice Affects Ice Sheet Growth
by
Vera Jesser Lawson
Master of Science in Marine Science
California State University Monterey Bay, 2016

Ice sheets are losing volume and regions of sea ice cover are shifting; these changes in Arctic and sub-Arctic regions amplify climate change through positive feedback mechanisms. A history of sea ice cover and iceberg activity in high latitude seas would help to predict climate change. Sea ice and icebergs entrain and dump sediment into the oceans; both transport sand, but glacial ice is much more likely to entrain gravel (>2 mm) than sea ice. This study uses siliciclastics >63 μm from Bering Sea Site U1343 to track icebergs and sea ice during the Mid-Pleistocene, a period of change in global climate cycles. Fine sand (63<<250 μm) averages 10% of the bulk sediment at U1343 from 910 to 860 ka. A new method uses a ratio (fine sand/gravel count) to indicate the more likely presence of sea ice. Icebergs are likely present during Marine Isotope Stage (MIS) 23 and in the latter part of MIS 22 when four pulses of gravel-size ice rafted debris come before the deglaciation. A period of low ice rafted debris in MIS 22 when the sea level is decreasing rapidly is interpreted as a time of more open water. Sea ice is suggested at the coldest time in MIS 22 and at the start of the deglaciation, consistent with the Sea Ice Switch (Gildor and Tziperman 2000) hypothesis for the Mid-Pleistocene climate transition. Abundant fine sand in MIS 21 suggests the presence of sea ice in the early interglacial.

TABLE OF CONTENTS

LIST OF TABLES

LIST OF FIGURES

ACKNOWLEDGEMENTS

CHAPTER 1

INTRODUCTION

The extent and location of sea ice covering Arctic and sub-Arctic seas, and the volume of ice on continents is changing. Arctic sea ice shows a decline of 3% per decade between 1979 and 2012 (NSIDC 2012). However, the Antarctic sea ice extent may be increasing; it set a new record maximum each year in 2012, 2013 and 2014 (NSIDC 2015). The Intergovernmental Panel on Climate Change (IPCC 2013) reports the loss of ice mass in Greenland and Antarctic ice sheets, and the retreat of most glaciers worldwide. These changes in the cryosphere may change earth's climate through positive feedback mechanisms (Holland and Bitz 2003) that are particularly strong in the North Pacific (Dethloff et al. 2006). A study of past changes in sea ice cover in the Bering Sea in relation to global continental ice sheet volume would serve to inform models used to predict what is presently happening to earth's climate. Evidence for past melting of continental ice sheets and for past sea ice extent is found in deep marine sediments that hold siliciclastics (silica bearing rock fragments and minerals) from the continent and continental shelf that were entrained, transported, and released by ice (Heinrich 1988).

SEDIMENT ENTRAINMENT IN ICE

ENTRAINMENT BY GLACIERS

Glaciers scrape landscapes, entrain sediments and dump debris. Glacial cirques, hanging valleys, U-shaped valleys, and fjords are landforms that are the result of alpine glaciation. Most of the sediment removed from these areas is transported by subglacial processes, but some is entrained in ice by various mechanisms (Alley et al. 1997). In a study on the erosion processes of a fast flowing alpine glacier, Herman et al. (2015) found that abrasion processes dominate, and that sediments come primarily from underneath the glacier. Erosion increases nonlinearly with the glacier's velocity, which increases with slope and rain events. According to Herman et al. (2015), this may explain why glacial erosion in the Pleistocene is most pronounced in mountainous regions in the

mid-latitudes. At higher latitudes where glaciers occur at lower elevations and glacier tongues extend to the coastline, tidewater glaciers calve icebergs laden with sediment into the sea.

ENTRAINMENT BY SEA ICE

Sea ice entrains, transports and releases sediment from the continental shelf. Cold winds chill and stir up the sea water during the fall freeze-up and in mid-winter over polynyas. Small sticky disks of frazil ice, 1 to 5 mm in diameter and 1 to 100 μm thick (Kempema et al. 1989) form and stay suspended in the turbulent waters. Where the water column is <40 m deep, convective cells transport clay- and silt-size bottom sediments upward from the nepheloid layer. These sediment particles adhere to the frazil ice which floats to the upper water column where the slushy mixture hardens into turbid ice (Dethleff and Kuhlmann 2009). This suspension freezing mechanism primarily entrains the clay- and silt-size particles which are the bulk of the sediment in sea ice (Reimnitz et al. 1998).

Coarser grains are entrained by anchor ice, "ice that grows on a submerged substrate in quiet or super-cooled water and remains attached to that substrate", as defined by Reimnitz et al. (1987). Anchor ice forms during winter storms which super-cool the water column down to a maximum depth of 20 m. Frazil ice disks in the turbulent water stick and remain on the heavier, sand-size sediment on the shallow sea floor. The ice mass grows and entrains whatever is on the bottom. These anchor ice masses detach, float, and become incorporated into the sea ice, entraining sand and some coarser gravel. In this way, significant quantities of shallow shelf sediment are likely rafted by sea ice to the outer shelf and beyond (Reimnitz et al. 1987). The relative contribution of debris rafted by frazil ice and anchor ice is not well understood (Polyak et al. 2010).

In the Arctic, the ice pack is 99% sea ice and 1% iceberg ice (Clark et al. 1980), so the total mass of sediment entrained by sea ice is potentially more than by icebergs, and the contribution of sea ice rafted debris to deep marine sediments over ablation areas is significant (Nürnberg et al. 1994).

ICE RAFTED DEBRIS IN DEEP MARINE SEDIMENTS

THE DEEP MARINE SEDIMENTARY ENVIRONMENT

Deep marine sediments contain whatever has settled from the water column, been transported by gravity flows and geostrophic currents, and precipitated in situ (Kennett 1982). Diatoms and planktonic foraminifers are abundant in the sediment under biologically productive zones. Airborne terrigenous clay and volcanic ash vary according to the winds and the distance to the source. Proximity to the continental slope will increase the likelihood of terrigenous input from mass wasting, turbidity currents, and contour currents. Where the deep ocean is beneath the path of melting icebergs, ice rafted debris accumulates in the sediments. If sea ice ablation extends over the deep ocean, ice rafted sediment from the shallow continental shelf settles in the deep marine environment. Biochemical and chemical processes result in the growth of authigenic minerals such as pyrite in shallowly buried marine sediments (Rothwell 1989). Diagenesis of buried matter results in clumping of the sediment. In order to confirm ice rafted debris (IRD) in the sediments, inputs other than ice rafting need to be ruled out.

ICEBERG OR GLACIAL ICE RAFTED DEBRIS (GIRD)

Non-volcanic siliciclastics larger than 250 µm, when found in deep ocean sediments distant from the continental shelf and at relatively high latitudes, are generally taken to be an indication of iceberg IRD (von Huene et al. 1971; St. John and Krissek 2002). A sample source location on an offshore bathymetric high reduces the possibility of other forms of transport (St. John 2008). In a study of deep sea sediments on a rise off the continental slope, the mass accumulation rate (MAR) of the 250<<2000 µm fraction was interpreted as indicating the expansion of glacial ice in SE Greenland. This was supported by the consistency of the composition of the 250<<2000 µm fraction with that of larger dropstones found at the site (St. John and Krissek 2002). In a study of sediments in the pelagic Northern Atlantic (38°N to 68°N) farther from the continental shelf and the influence of sea ice, non-volcanic siliciclastics >63 µm were thought to be transported exclusively by icebergs (Snoeckx et al. 1999).

SEA ICE RAFTED DEBRIS (SIRD)

When tracking IRD in the Arctic and its marginal seas, rafting by sea ice in addition to icebergs needs to be considered as the sediments are dominated by discharge from sea ice (Lisitzin 2010). The >63 μm size siliciclastic fraction in deep sea cores from high latitudes, when in a pelagic setting not directly influenced by land-derived input and continental margin sedimentary processes, is considered to be IRD from icebergs and/or sea ice (Lisitzin 2002; Polyak et al. 2010). Various approaches have been used to attempt to distinguish between sea ice and iceberg rafted debris. Bischof and Darby (1997) found a different source for the detrital carbonate and siliciclastic grains in the >250 μm fraction than for the opaque Fe oxides in the 45<<250 fraction of Arctic sediments. They interpreted the Fe oxides as having been rafted by sea ice. St. John (2008) calculated MAR's for Arctic IRD fractions 150<<250 μm and >250 μm. These grain size fractions could not distinguish between the modes of transportation, and quartz grain characteristics (a petrographic method to ascertain the weathering mechanisms experienced by the quartz particles) showed a mix of sea ice and iceberg rafting (St. John 2008). In a study of Bering Sea non-volcanic siliciclastic deep sea sediments, Gorbarenko et al. (2010) considered the >150 μm fraction to be IRD, and used the count of siliciclastic grains per gram of dry bulk sediment to quantify the IRD. They suggested that the weight % of the >63 μm fraction and the >150 μm fraction might be useful for indicating sea ice activity. In their samples ash was too abundant to make the weight % useful. Distinguishing between GIRD and SIRD is important, but is challenging (Nürnberg et al. 1994; Lisitzin 2002).

THE GLOBAL CLIMATE RECORD

THE $\delta^{18}O$ PROXY

Evidence for past climate changes is found in the ratio of stable oxygen isotopes in calcite tests of benthic foraminifera found in deep sea cores. The $\delta^{18}O$ proxy is defined as the $^{18}O/^{16}O$ ratio relative to the same ratio in a standard. The benthic $\delta^{18}O$ records from deep marine cores around the globe reveal large fluctuations thought to reflect past changes in deep sea temperature and ice sheet volume (Clark and Pollard 1998). Marine Isotope Stages (MIS), glacials and interglacials in the records, have been identified and

numbered (Kennett 1982). Glacials, when $\delta^{18}O$ is high reflecting cold deep water and high volume of glacial ice, are numbered evenly back from the present. Interglacials, the periods between the glacials when $\delta^{18}O$ is low, are given odd numbers. Fifty-seven of these records have been tuned and combined into one stack to be used for stratigraphic records, the LR04 benthic $\delta^{18}O$ stack (Lisiecki and Raymo 2005). Figure 1 shows a portion of this stack covering MIS stages 25 to 21.
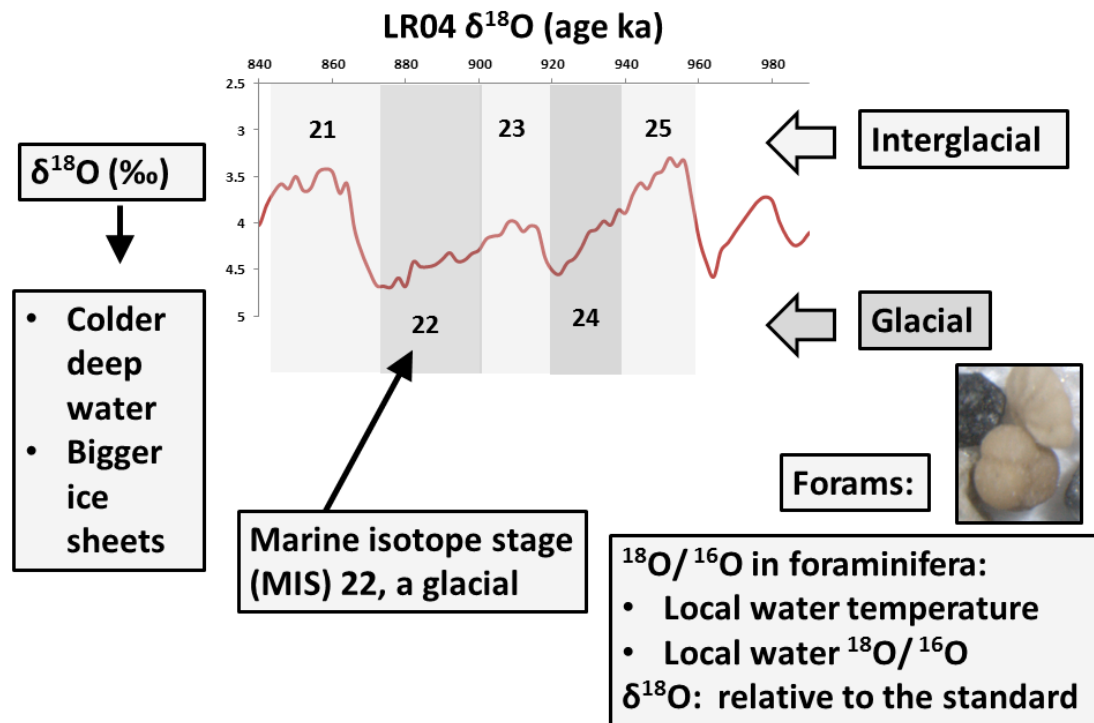
Figure 1. The $\delta^{18}O$ proxy and the LR04 benthic stack for MIS 25 to MIS 21

Benthic foraminifera incorporate oxygen from the local water into their tests in a $^{18}O/^{16}O$ ratio that is in temperature dependent equilibrium with the $^{18}O/^{16}O$ in the water. A larger fraction of the heavier oxygen isotope is incorporated into the carbonate test when the water temperature is colder. The sea water $^{18}O/^{16}O$ ratio changes as evaporation preferentially removes the lighter oxygen isotope and precipitation stores the lighter water on land, primarily in the form of snow and ice. Brennan et al. (2013) summarize the work done on understanding this proxy when they report their modeled effect of sea ice on glacial/interglacial changes in $\delta^{18}O$. Even though sea ice preferentially entrains the

heavier ^{18}O, decreasing the δ^{18}O in sea water (up to 3‰; O'Neil 1968), they found that changes in sea ice over glacial/interglacial cycles has little influence (<0.14‰) on δ^{18}O changes in sea water. The δ^{18}O from benthic foraminifera is a proxy that gives a signal that is dependent partially on deep sea temperature and partially on volume of land ice.

THE MID-PLEISTOCENE TRANSITION (MPT)

The δ^{18}O records from deep sea cores all over the globe show a marked change in cyclicity from ~100 ka to ~41 ka that takes place during the middle of the Pleistocene, between 1250 and 700 ka (Clark et al. 2006). Figure 2 is the LR04 benthic δ^{18}O stack extending back five million years (Lisiecki and Raymo 2005). This stack shows the Pliocene warm period before 2.75 Ma when the deep waters where not as enriched in ^{18}O. Significant Northern Hemisphere glaciation begins at ~2.75 Ma at the conclusion of this warm period (Ravelo et al. 2004). From 2.75 Ma to ~900 ka the record is characterized by more symmetric cycles with a ~41 ka period. A general global cooling trend extends from the Pliocene to 1.5 Ma (Ravelo et al. 2004). By 700 ka the period of the δ^{18}O cycles has fully shifted to 100 ka and the amplitude of the cycles shows the deep waters becoming even more enriched in ^{18}O during full glacials (Clark et al. 2006). Cycles in the later Pleistocene also take on an asymmetric saw-tooth pattern showing a slow build up of ^{18}O in deep waters, then a quick return to levels with more of the lighter ^{16}O isotope replenished. However, there is still a debate as to when this transition occurred, with some researchers pointing to a gradual shift (Ravelo et al. 2004) and others pointing to a change around 900 ka (Clark et al. 2006; Elderfield et al. 2012).
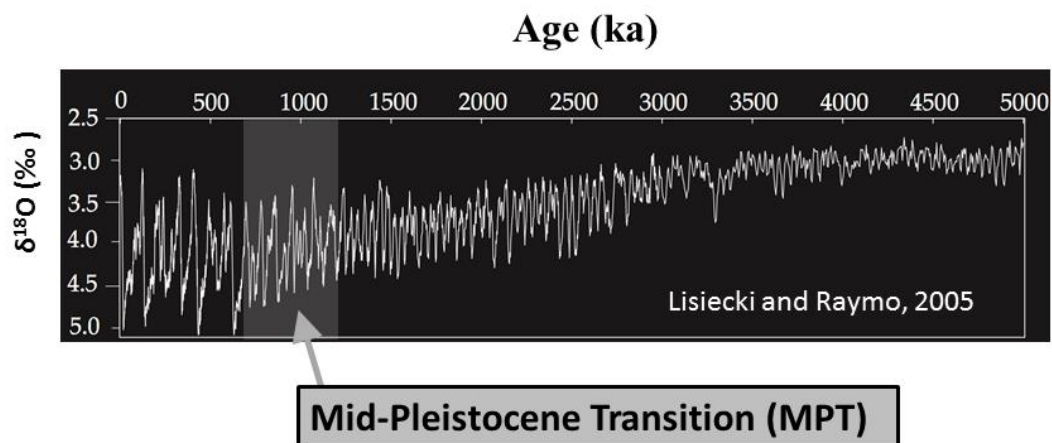
Figure 2. The LR04 benthic stack showing the Mid-Pleistocene Transition

The mechanisms that brought about the MPT are also disputed (Raymo and Huybers 2008). The forcing can be the result of changes that are internal to the earth's systems (changes in ice sheet stability, ocean circulation, deep ocean temperature, concentration of greenhouse gases, etc.) or they can be external (variation in insolation caused by changes in earth's three orbital parameters: precession which has the greatest effect, obliquity, and eccentricity which has the least effect), or a combination of both (Clark et al. 2006). Raymo, Ruddiman, and Froelich (1988) proposed that the MPT was the result of a gradual decrease in atmospheric CO_2. They suggested that increased uplift rates in tectonically active areas during the last 5 Ma enhanced continental weathering, drawing down CO_2, a green house gas which amplifies the variations in insolation. Before the MPT, obliquity (41 ka cycles) modulated the precession cycles (19 and 23 ka cycles), while after the MPT eccentricity (100 ka cycles) modulated the precession cycles. Clark and Pollard (1998), pointing out that there was no significant change in the orbital forcing over the MPT, proposed that the MPT is attributable to ice sheet erosion of regolith (the loose material overlaying bedrock). Changes in ice sheet stability result from changes in the underlying bed, increasing the potential for ice sheets to grow thicker. Gildor and Tziperman (2000; 2001) proposed that the MPT is a result of the gradual cooling of the deep ocean which activated a 'Sea Ice Switch' at the MPT. This mechanism is discussed in more depth in the next section.

THE SEA ICE SWITCH MECHANISM FOR THE MID-PLEISTOCENE TRANSITION

A proposed mechanism to drive the climate transition from 41 ka to 100 ka cycles is the Gildor and Tziperman 'Sea Ice Switch' (SIS) (2000; 2001). The development of sea ice over open water has two main effects: 1) increasing the albedo and thus cooling the climate, and 2) insulating the ocean surface from the atmosphere reducing heat loss and evaporation and thus reducing precipitation. Figure 3, simplified from Gildor and Tziperman (2003), shows the schematic relations between continental ice accumulation and ablation rates in relation to atmospheric temperature. The accumulation rates for open water conditions are different than when the water is covered with sea ice. When sea ice forms, the accumulation rates drop dramatically; this is shown in the diagram by the vertical drop between the open circles on the accumulation rate lines. As shown by comparing the two graphs, the atmospheric temperature at which sea ice forms is colder

for a warm deep ocean in which enhanced vertical mixing brings heat to the surface from deep water. The SIS mechanism is based on the changes brought about by the gradual cooling of deep water during the Pleistocene. The Warm Deep Ocean graph depicts the schematic relation in the early Pleistocene; the Cold Deep Ocean graph depicts it after the MPT.
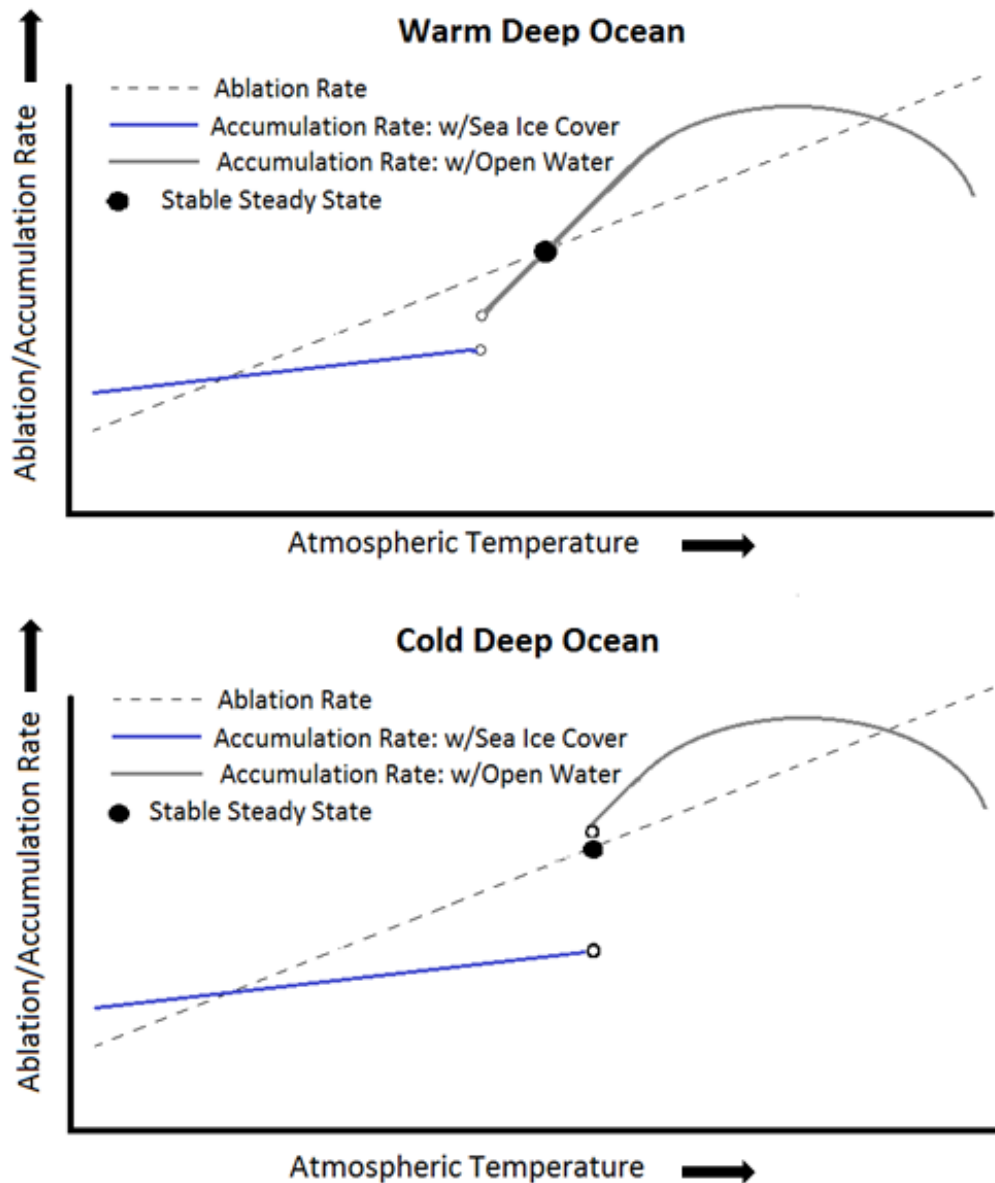
Figure 3. Sea Ice Switch schematic relations (Gildor and Tziperman 2003)

In the early Pleistocene, according to the SIS model, the climate would have cycled about the stable steady state, which occurs when the ablation rate is the same as the accumulation rate (where the lines cross in Figure 3 top schematic relation). Notice that this occurs when the accumulation rate is still in the open ocean mode. Sea ice extent would be limited during these climate cycles. The SIS model produces symmetric cycles during this period (Tziperman and Gildor 2003). After the MPT (in the bottom schematic relation) the stable steady state is at an atmospheric temperature when the accumulation rates are switching between open water and sea ice cover conditions. Tziperman and Gildor (2003) have shown that in the SIS model, climate cycles about this stable steady state are characterized by an asymmetrical saw-tooth structure, with longer periods of ~100 ka. These climate cycles do involve the presence of extensive sea ice cover.

The transition from 41 to 100 ka cycles may have involved the activation of this sea ice switch as a result of the gradual cooling of the deep ocean during the Pleistocene. If so, substantially more sea ice would be present after the MPT than before (Tziperman and Gildor 2003). The model predicts that the beginning of a deglacial should follow a time of substantial sea ice cover in a cold period (Gildor and Tziperman 2001). The SIS model could be tested by checking for the timing of the increased presence of sea ice and the start of the land deglaciation (Gildor and Tziperman 2003). This requires distinguishing and tracking the abundance of GIRD and SIRD in the sediments of a high latitude sea. Testing the SIS model in the Bering Sea is one of the goals of this research.

THE BERING SEA

The Bering Sea, a high latitude marginal sea, is an ideal place to study climate changes. The seasonal sea ice advance and retreat in the Bering Sea is greatest of all Arctic and sub-Arctic regions (Walsh and Johnson 1979), and the winter extent of sea ice is very susceptible to regime shifts in climate (Niebauer 1998). Though separated from the Pacific by the Aleutian Island Arc, deep water passes connect the Bering Sea to the Pacific and to the influence of deep water from the Southern Ocean. The shallow Bering Strait connects the Bering Sea to the Arctic which in turn influences the Atlantic. As sea level falls in a glacial cycle, this connection is certainly severed in a way that must

change the circulation in the Bering Sea and could change global circulation patterns
(Takahashi 2005).

BATHYMETRY, WATER EXCHANGE, AND CIRCULATION

      The Bering Sea (Figure 4), with a volume of 3.75×10^6 km^3 and surface area of
2.29×10^6 km^2, is the world's third largest marginal sea (Takahashi 2005). The eastern half
of the Bering Sea covers the Alaskan continental shelf which presently extends over 200
km from the coast. The Siberian shelf to the west is much narrower. A large extent of the
Alaskan shelf is less than 50 m deep. Beyond the shelf break at ~200 m depth and the
continental slope cut by some of the largest canyons on earth, the sea floor drops to an
abyssal plain with an average depth of more than 3800 m reaching to a maximum depth
of over 4100 m (Takahashi et al. 2011). The submarine Shirshov Ridge which extends
south of the Koryak Range in eastern Siberia, divides the deep ocean into the Aleutian
Basin to the east and the Komandorski Basin to the west. The Bowers Ridge, a
submerged older volcanic arc extending 300 km north from the Aleutians (Aiello and
Ravelo 2012), separates the Aleutian Basin from the Bowers Basin to the southwest.
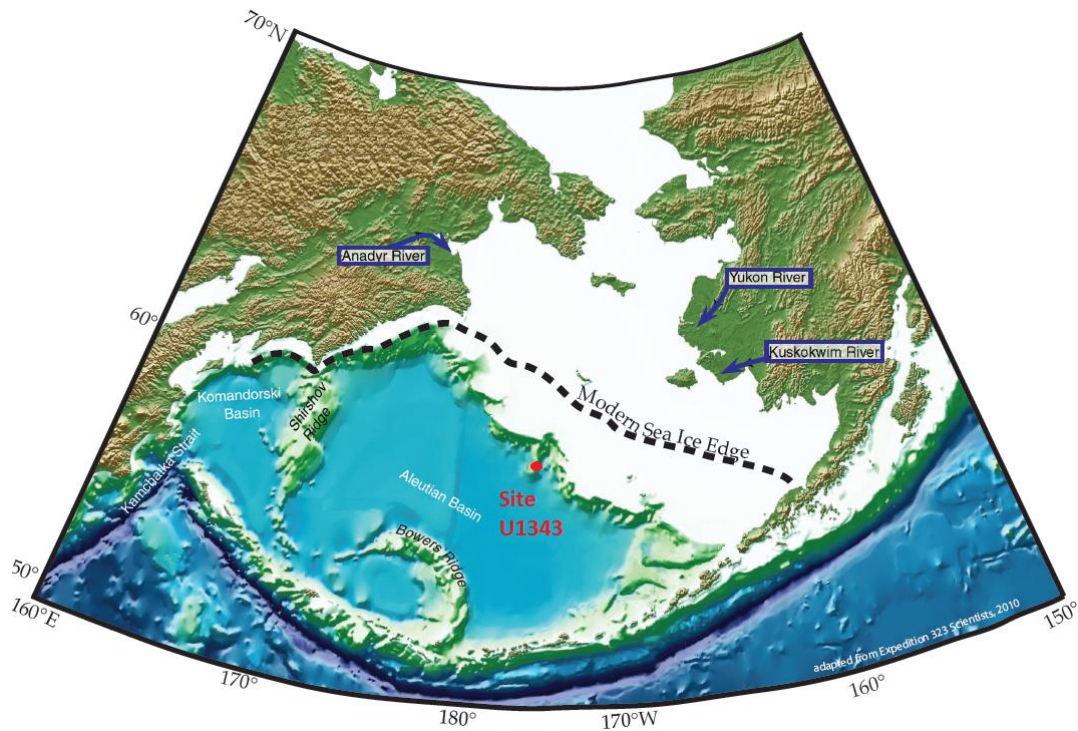
Figure 4. The Bering Sea, redrawn from Expedition 323 Scientists (2011a)

Three major rivers flow into the Bering Sea bringing fresh water and sediment to the continental shelf and beyond. The Kuskokwim and Yukon Rivers drain interior Alaska and the Anadyr River drains eastern Siberia (Figure 4). Of these the Yukon has the greatest flow, peaking in late summer when its discharge is comparable to the Mississippi River (Takahashi et al. 2011).

The Bering Sea exchanges water with the Pacific through multiple passes in the Aleutians (Figure 5), and exports water to the Arctic through the Bering Strait. Water from the Alaska Coastal Current goes through the Unimak Pass onto the Bering Shelf with a mean transport of 0.23Sv. The mean Bering Strait transport over the shelf to the Arctic Ocean is 0.85Sv (Stabeno et al. 1999). These flows are small in comparison to the exchanges between the Pacific and the Bering Sea at deeper passes. The location of the entrance of Alaskan Stream water to the Bering Sea varies depending on local and seasonal weather conditions. Water primarily enters through the Amutka Pass and the deeper Amchitka Strait, bringing relatively warm water to the southeastern Bering Sea (Takahashi et al. 2011). The Near Strait and the Kamchatka Strait, deeper passes to the west, exchange volumes of water an order of magnitude higher. The Near Strait brings flow into the Bering Sea from the Alaskan Stream and the Subarctic Current, but this flow is variable. These straits also allow for the exchange of intermediate waters. The Kamchatka Strait, at a present depth of 4420 m, allows for the exchange of deep water (Stabeno et al. 1999).

Large scale circulation in the Bering Sea (Figure 6) is generally counterclockwise, but surface currents shift with the seasons and wind curl (Stabeno et al. 1999; Takahashi 2005). Various water inputs from the Alaskan Stream, the Subarctic Current, and at times the recirculating Kamchatka Current, form the Aleutian North Slope Current (ANSC) which runs eastward north of the Aleutians. Storms track over the Aleutians more frequently in the winter, strengthening the Alaskan Stream which adds most of the water coming into the Bering Sea. Alaskan Stream surface waters are fresher, and its deeper waters are relatively warm. Strong vertical mixing is thought to occur between the 100 and 400 m isobaths off the continental shelf break near the Pribilof Islands (Hermann et al. 2002). As the ANSC approaches the continental shelf, the current mixes with upwelling water, turns northward, and becomes the Bering Slope Current (BSC) which

generally follows the shelf edge to the northwest. This current is shallower than the ANSC, but broader, so that it has similar volume transport. The flow can separate from the slope at the axis of the Zemchug canyon and head westward (Stabeno et al. 1999). Winds over the Bering Sea are stronger by an order of magnitude in the winter, and can reduce the northward transport over the shelf, sometimes shifting it weakly towards the south (Overland and Roach 1987). Frigid northeast winds can even reverse the surface flow through the Bering Strait (Stabeno et al. 1999). A western boundary current, the Kamchatka Current, completes the cyclonic Bering Sea surface circulation, flowing south through the Kamchatka Strait.
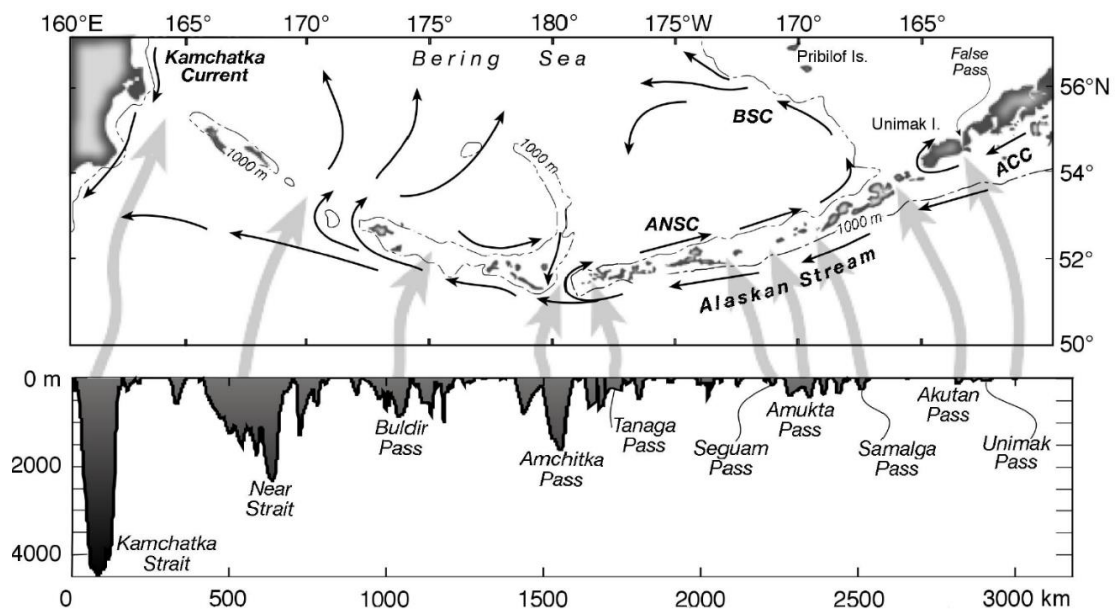
Figure 5. Passages connecting the Bering Sea to the Pacific (Stabeno, 2016)

SEA ICE GROWTH, TRANSPORT, AND ABLATION IN THE BERING SEA

Sea ice starts forming in the Bering Sea during the fall, and new sea ice continues to grow through the winter (Pease 1980; Overland and Pease 1982). Frigid northeasterly winds over the shallow shelf chill the seawater column to -1.7°C, the freezing point of seawater, and freezing begins north of St. Lawrence Island (Figure 7). As the shallow shelf waters super-cool, sea ice growth continues along the coast through the winter, reaching as far as Bristol Bay. See Figure 4 for modern sea ice extent (Wang and

Overland 2009). Polynyas persist through the winter on southwest facing coastlines. In open water on the lee of Cape Nome and St. Lawrence, St. Matthews and Nanuvak Islands, new sea ice forms though the winter.
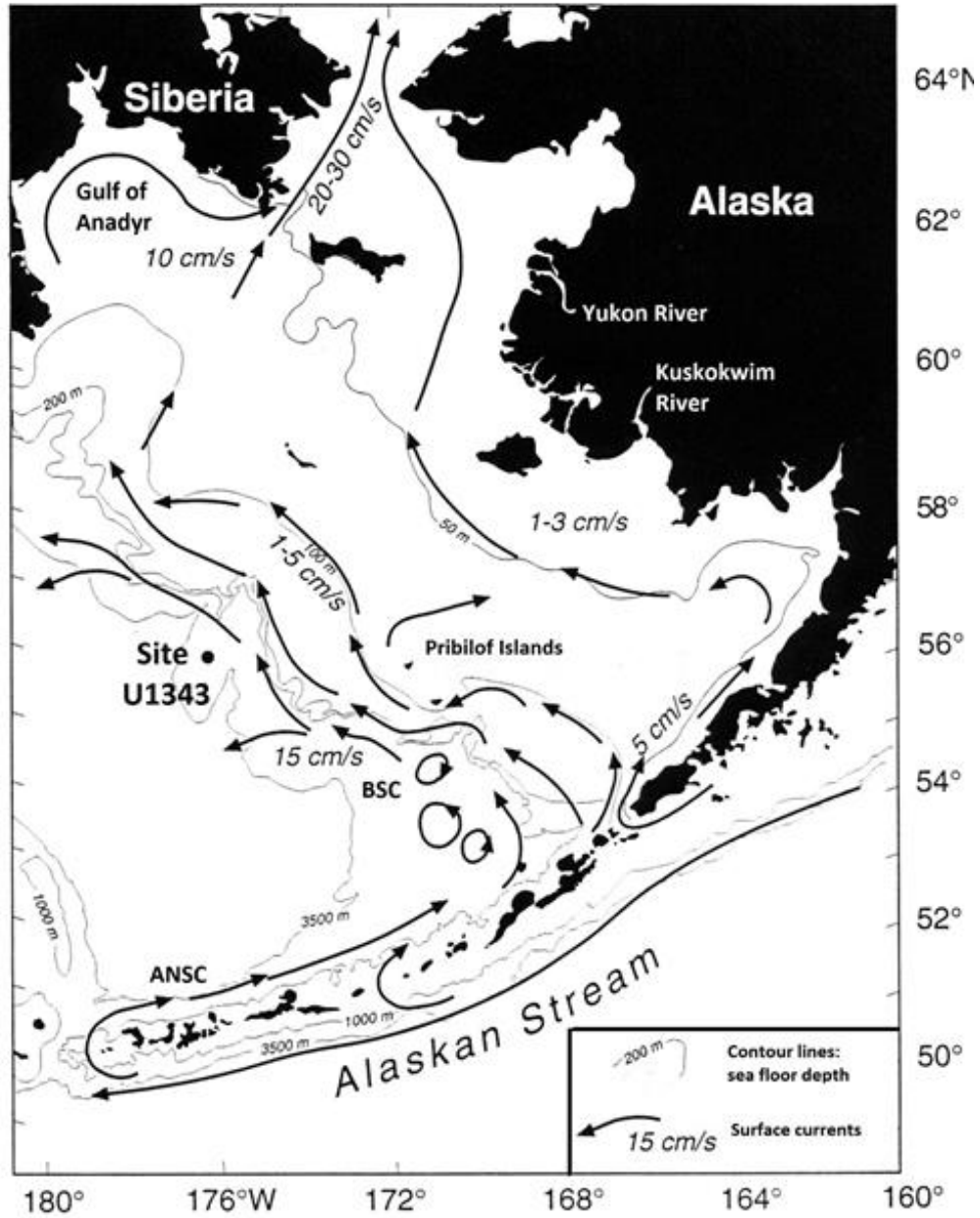
Modified (with permission) from Hermann et al. (2002)

Figure 6. Eastern Bering Sea with surface currents and sea floor depths
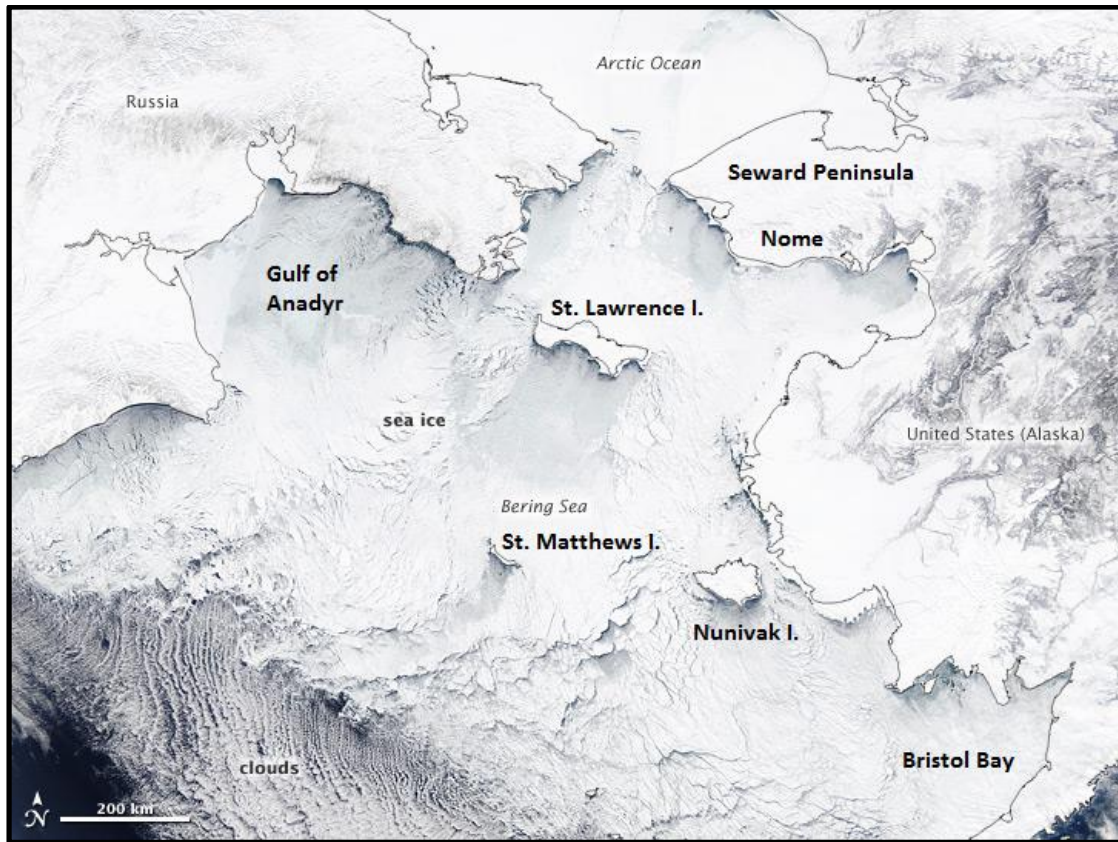
Figure 7. Bering Sea with sea ice on March 20, 2012 (NASA's Earth Observatory)

Sea ice is mainly driven by the prevailing winter winds to the southwest into warmer water. The lead sea ice flows melt, adding cold fresh water to the surface waters, and increasing the residence time of subsequent ice flows that are in thermodynamic stability with the surface water. The sea ice extent expands until it reaches water in which it is not in thermodynamic equilibrium, generally by the continental shelf break (Figure 4). By this "conveyor belt" process, sea ice in the Bering Sea can be transported 200 to 300 km beyond the growth region (Pease 1980). The entire ice pack can replace itself two to five times each season by this mechanism (Overland and Pease 1982). Over the course of a winter the sea ice can carry sediment entrained in the northern shallow shelf regions to the edge of the continental shelf and beyond.

EVIDENCE FOR FORMER GLACIATIONS AROUND THE BERING SEA

Evidence for past alpine glaciation that could impact the Bering Sea is found both on land and in the deep marine sediments. Alaska presently has the largest valley glaciers

in North America. Furthermore, during the Last Glacial Maximum (LGM), the area covered by glacial ice was ten times the present (Kaufman and Manley 2004). Moraines show the reach of the glacial ice during the LGM into the Gulf of Alaska, and during the penultimate glaciation into Bristol Bay. See figures online from Briner and Kaufman (2008) showing the extent of glacier ice in Alaska during the LGM and in the Ahklum Mountains during the penultimate glaciation, www.interscience.wiley.com/journal/jqs). Northeast Siberia west of the Bering Sea is sparsely glaciated now, but during the Pleistocene over 500,000 km^2 was glacial ice covered (Zamoruyev 2004). The Koryak Range south of the Anadyr River shows fjords from alpine glaciation reaching to the coastline that are similar to those in Alaska (Briner and Kaufman 2008). Kamchatka was cyclically glaciated during the Pleistocene, providing GIRD to the Bering Sea (Bindeman et al. 2004). Pebbles in deep marine sediments in the Northwestern Pacific are thought to have been iceberg rafted from the western Bering Sea down the eastern coast of the Kamchatka Peninsula (McKelvey et al. 1995). Dropstones from a site in the Gulf of Alaska seem to have been GIRD from southeastern Alaska that were carried in the path of the Alaskan Stream (McKelvey et al. 1995). IRD MAR records from the same Gulf of Alaska site show a large supply of sediment input coming from coastal Alaska (St. John and Krissek 1999). Icebergs carrying debris from southeastern Alaska may have entered the Bering Sea by way of the Alaskan Stream. Dropstones are commonly found in Bering Slope sediments and in Bowers Ridge sediments younger than 2.7 Ma, a time which coincides with the beginning of the Northern Hemisphere Glaciation (NHG) (Takahashi et al. 2011). Dropstones in Bering Sea site sediments increase significantly in sediments younger than 1 Ma (Takahashi et al. 2011). These may be GIRD, SIRD, or both.

EVIDENCE FOR FORMER EXTENT OF SEA ICE IN THE BERING SEA

The presence of sea ice drift in the Bering Sea is suggested by an increase in sea ice diatom and dinoflagellate forms as the global climate cooled during the NHG (Expedition 323 Scientists 2011a). Changes in radiolarian assemblages during the LGM suggest that during full glacials, low temperature and low salinity surface waters extended throughout the expanse of the Bering Sea, and that seasonal sea ice reached beyond the continental shelf to the central Aleutian Basin at Bowers Ridge (Tanaka and Takahashi 2005). Katsuki and Takahashi (2005) infer that the diatom production during

glacial periods was higher than present, but the diatom accumulation rates in the sediments were lower during glacials because of the preferential dissolution of the sea ice diatoms. Aiello and Ravelo (2012) found that interglacial (interstadial) sediments are characterized by better diatom preservation and less terrigenous siliciclastic input, while glacial (stadial) sediments are characterized by lower diatom preservation and more terrigenous siliciclastic input. This is consistent with sea ice transport of rafted debris during glacials. The weak negative correlation between grain size and sorting in the Bering Sea slope siliciclastic sediments, and pattern of the northernmost Bering Sea slope sites showing the most abundant, finest and best-sorted siliciclastic sediment, are consistent with sea ice delivery (Aiello and Ravelo 2012). The Expedition 323 Scientists (2011) found the relative abundance of the sea ice diatoms taxa increasing from 30% to 70% over the Pleistocene, with a significant increase in abundance at the mid-Pleistocene. The Meiji Drift, a sediment deposit in the northwest Pacific Ocean, contains sediments that were outwashed from the Bering Sea (VanLaningham et al. 2009). During glacial periods, when sea ice in the Bering Sea was likely, those drift sediments were heavily influenced (as much as 45%) by the Yukon River and northeast Russia sources. Tanaka and Takahashi (2005) found that the water mass structure in the western subarctic Pacific during the LGM was similar to the eastern Bering Sea (low-temperature, low salinity surface layer with sea-ice coverage) but weaker in its magnitude of development.

INTEGRATED OCEAN DRILLING PROGRAM (IODP) SITE U1343

One of the scientific objectives of the Integrated Ocean Drilling Program (IODP) Expedition 323 is "to characterize the history of continental glaciation, river discharge, and sea ice formation in order to investigate the link between continental and oceanic conditions in the Bering Sea and on adjacent land areas" (Expedition 323 Scientists 2011). Site U1343, in the middle of the Bering Sea, on a rise clearly separated from the continental shelf, and near the present extent of sea ice, was drilled to explore the history of glacial ice and sea ice in the Bering Sea.

SITE LOCATION, DRILLING, AND CORE RECOVERY

Site U1343 (Figure 8) was chosen carefully by the Expedition 323 scientists (2011). The site is at a depth of more than 1950 meters below sea level (mbsl) on the

southwest slope of a rise where it is thought to be sheltered from turbidites coming from the shelf. The shelf break and the axis of the Zhemchug canyon are more than 70 km away. The site is at least 1000 m above the floor of the canyon channel 20 km to the east. Seismic profiles at U1343 show undisturbed sediments, an essential requirement to make a time record.
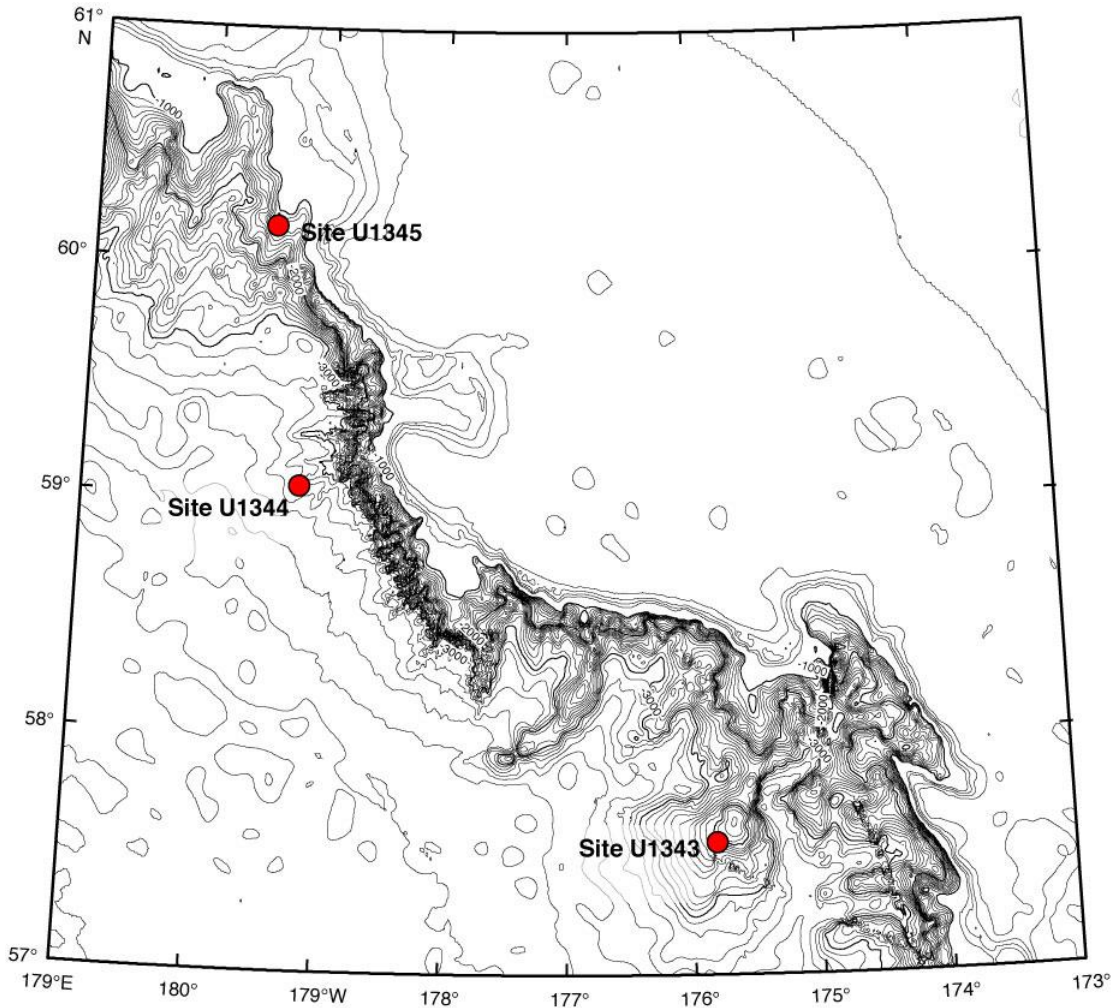
Figure 8. IOPD 323 Bering Sea slope sites (Expedition 323 Scientists 2011a)

According to IODP procedures, five holes designated A, B, C, D, and E, were drilled at Site U1343 in order to make a spliced record with the best retrieved parts from each hole. Cores, usually 9.5 m or less, are numbered from the top and labeled with a

designation for the type of piston corer used. Cores are divided into sections of 1.5 m or less which are also numbered from the top. Sample 323-U1343C-23H-3A for example, is from Expedition 323, site U1343, hole C, core 23 drilled with an advanced piston corer, and section 3. The "A" designation specifies the archived half of the section that was split. Samples distributed for use in research are from the working half of the split section and labeled with a "W". Samples are also designated by the distance in centimeters to the top of the section. Sections from the three deepest holes, A, C, and E, were used in the splice for site U1343. See Table 1 for location, water depth, penetration depth below sea floor (DSF), recovery %, and the number of cores for U1343A, U1343C and U1343E. Note that the recovery % can be more than 100% if the core expands.

Table 1. Expedition 323, Site U1343, Holes A, C, and E.

Hole	Latitude	Longitude	Water Depth (m)	Penetration DSF(m)	Recovery %	# of Cores
A	57 33.3993 N	175 49.0275 W	1964	201.5	101	22
C	57 33.3982 N	175 49.0275 W	1964	234.2	99	26
E	57 33.3814 N	175 48.9974 W	1967	744.3	94	94

SHIPBOARD DATA COLLECTION

In shipboard labs, the split cores were visually described, physical properties were measured, and siliciclastic and biogenic grains from sediment samples were observed and counted using smear slides. The data gathered was used to start to match the holes stratigraphically in order to make the splice and to get estimates for ages and linear sedimentation rates. The sediment at U1343 is mostly clayey silt alternating with diatom clayey silt and occasional sand layers. Natural gamma radiation was very variable, indicating fluctuating terrigenous input. Estimates of the age of the deepest sediments retrieved from U1343E are around ~2.4 Ma, giving an average linear sedimentation rate of 35 cm/ka. Sea ice diatom percentages and observations of sea ice related dinoflagellate taxa give some preliminary indication of changes in sea ice cover in the Bering Sea. Sites from Expedition 323 near the continental slope show a dramatic increase in sea ice diatoms between the Pliocene and the Pleistocene, with increases and the amplitude of the variability changing the most around the MPT (1.2 to 0.8 Ma) (Takahashi et al. 2011).

RESEARCH QUESTIONS

In order to understand the history of continental glaciation as well as sea ice in the Bering Sea during the MPT, patterns in sea ice and glacial ice rafted sediments need to be recognized. That is asked by the first question addressed in this thesis: Can GIRD and SIRD be tracked in U1343 deep sea sediments?

To recognize the connections between continental and oceanic conditions, a close high resolution look at the changes in both kinds of IRD is needed. The second question to be addressed is: How did SIRD and GIRD vary in the Bering Sea over millennial time scales during the MPT?

Lastly, the Bering Sea is likely to have amplified patterns of climate change in the past. Tziperman and Gildor's SIS mechanism for the MPT is based on the effects of sea ice cover on ice sheet growth. Does this IRD data set give support to the SIS mechanism for the MPT?

CHAPTER 2

METHODS

SAMPLE SOURCE

Sediments at U1343 are sampled closely to make a high resolution data set over a glacial/interglacial cycle in the Mid-Pleistocene. The samples from the working splice come from U1343C (55 samples, from U1343C-23H-3W, 8.0-10.0 cm to U1343C-23H-6W, 126.0-128.0 cm), and from U1343E (88 samples, from U1343E-25H-2W, 0.0-2.0 cm to U1343-25H-7W, 102.0-104.0 cm). The depth intervals between samples vary from 6 cm to 24 cm, averaging 9.7 cm. These amount to 143 samples over 12 meters of depth. The depths from the two holes were correlated for the splice, so depths are given in meters, core composite below sea floor (m ccsf).

The samples were first processed by Kender (personal communication, 2014) in order to extract foraminifera for micropaleontological analysis. The following method was used in Kender's lab: each scoop of sediment (~34 cm^3) was freeze dried and the dry bulk sample weighed. The samples were treated by washing with cold deionized (DI) water over a 63 μm sieve, and dried in a 40°C oven. Benthic foraminifera were picked out for δ^{18}O analysis. The remaining >63 μm fraction of the bulk sediment is the subject of this study.

THE SITE U1343 AGE MODEL

Using low resolution magnetostratigraphy and biostratigraphy, together with the high resolution δ^{18}O data from U1343, an age model for U1343 was developed by Kender (unpublished) by comparing the U1343 benthic δ^{18}O record with the LR04 benthic δ^{18}O stack (Lisiecki and Raymo 2005) (Figure 9). The records are tied at major deglaciations, at 916 ka (237.8 m ccsf), and at 866 ka (226.5 m ccsf). These tie points give sedimentation rates of 22.6 cm/ka between 916 and 866 ka, and ~35 cm/ka after 866 ka. Each sample collected using a 2 cm wide scoop, averages ~90 years for samples collected before 866 ka, and ~60 years for the period after. The average interval between samples is 400 years, varying irregularly between 270 years and 1,000 years. Samples

from U1343C (860 to 878 ka) overlap the samples from U1343E (873 to 910 ka) by 6 ka. Both are from the working splice.
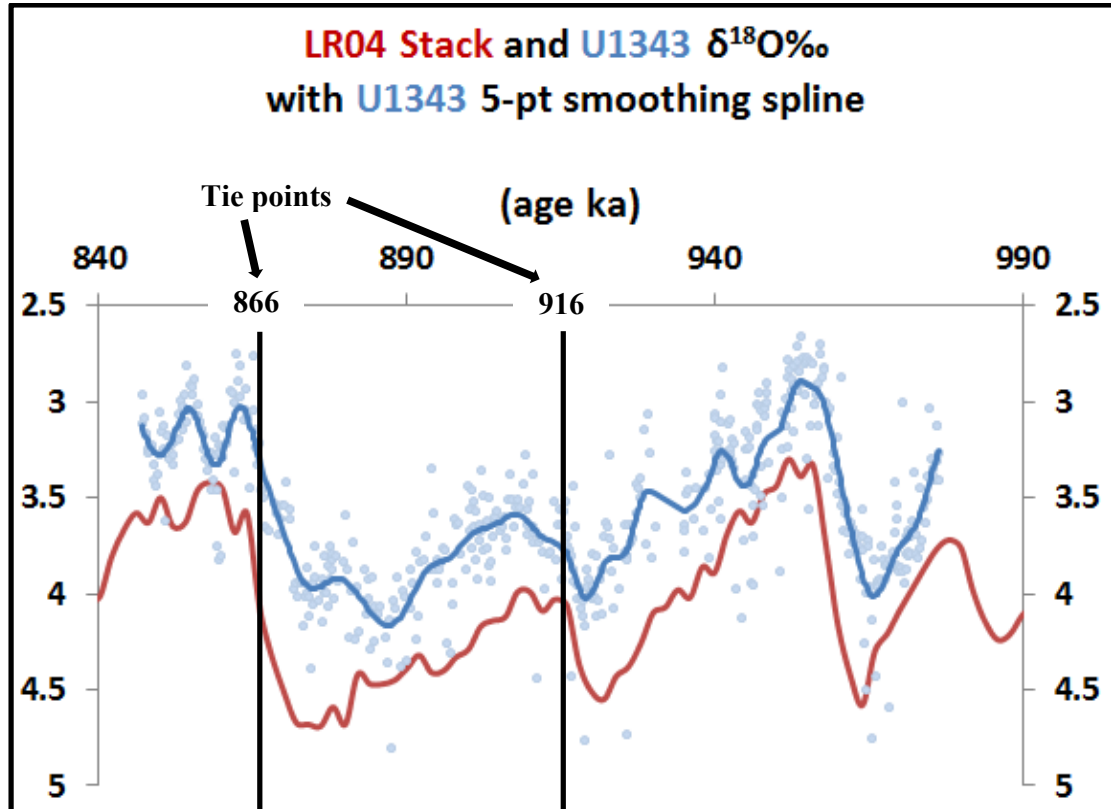
Figure 9. Kender U1343 δ¹⁸O unpublished age model and LR04 benthic δ¹⁸O stack

LABORATORY METHODS

All samples were weighed at ambient room temperature with a Mettler Toledo XS205 analytical balance using size appropriate antistatic polystyrene weighing dishes, (square, ~0.7g and hexagonal, ~1.6 g). Weights were recorded to the nearest 10^{-5} g. The dish was weighed each time and the weight of the dish subtracted out. Weighing dishes were laboratory air blown for cleaning between uses. A funnel on a stand and fine brushes were used to transfer samples to the weighing dishes and storage bags and vials.

SAMPLE PREPARATION

As discussed earlier, the samples received from Kender were initially sieved at 63 µm for the purpose of picking foraminifers and thus subjected to a relatively gentle

processing. To ensure the disaggregation of the clay- and silt-size sediments that often occur as clumps (e.g. St. John 1999), they had to be treated more aggressively before re-sieving at the same mesh size. The sample preparation adopted for this study is comparable to that of St. John (2008). After weighing the sample, 40 ml of warm (40°C) DI water and 3.0 ml of a 0.2 M solution of sodium hexametaphosphate (NaHMP) (Andreola et al. 2004) was added to the sample in a 50 ml wide mouth glass jar. The resulting concentration of the NaHMP solution is equivalent to 1g/liter of solution, the same concentration used to deflocculate clay-size particles when using the LS1230 Beckman Coulter Lazer Particle Sizer (personal communication, Aiello 2012). The jar was capped (with pin holes in the cap), vortexed manually to suspend the sediments, sonicated for 2 minutes in a FS15 bath sonicator, vortexed manually a second time, and sonicated another 2 minutes. Four samples were prepared for sieving at a time (Figure 10). The oldest four samples had slightly different treatments as they were used to explore the sediment and to test methods.

Figure 10. U1343E-25-6W, 77-79, 86-88, 96-98, 102-104 cm, 903 ka, ready to sieve

SIEVING, DRYING, AND WEIGHING

Samples were sieved using a stack of a 250 μm sieve over a 63 μm sieve over a 600 mL beaker (3" diameter, 1 ¾" high, stainless steel sieves). A sleeve of plastic packing material between the 63 μm sieve and the beaker held the sieves stable and provided a method to use suction to help filter through the finer sieve. A squirt bottle with room temperature DI water was used to rinse the jars and the sieves. The fraction caught on the >250 μm sieve was rinsed, transferred to filter paper, and allowed to drain

on a rack. The remaining 63<<250 μm fraction was rinsed over the 63 μm sieve until the water coming in to the 600 mL beaker was no longer brown but relatively clear, was transferred to coffee filter paper, and was allowed to drain (Figure 11). Water bearing the <63 μm sediments in the beaker was disposed of. The 250 μm sieves were dried and cleaned between samples. The 63 μm sieves were rinsed thoroughly with DI water between samples.

Figure 11. Set up procedure for sieving: stacks, drip bar, and drying screen

The fractions on the filter paper were dried on a screen under heat lamps, were allowed to cool to room temperature, were transferred to a weighing dish (>250 μm to the small square dish, 63<<250 μm to the hexagonal dish), and were weighed.

Medium, coarse, and very coarse sand-sizes are included in the 250<<2000 μm size range. Fine and very fine sand-sizes are included in the 63<<250 μm size range. These grain size categories follow the Wentworth size classes. For simplicity, in this paper, the 250<<2000 μm size fraction will be referred to as 'coarse', and the 63<<250 μm size fraction as 'fine'.

SEPARATING THE >2000 μm FRACTION, COUNTING GRAVELS

Within the >250 μm fraction is a component >2000 μm that includes wood chips, siliciclastics, pyritized burrows, sediment clumps, pyroclastics, and other unidentified clear material. Compare similar findings by St. John (2008). Each >250 μm sample was checked using a Leica S8 APO binocular microscope, and material >2 mm in two dimensions was removed and weighed. This weight was subtracted from the >250 μm fraction to find the weight of the 250<<2000 μm fraction. The number of siliciclastics

>2000 μm in two dimensions, not pyritized burrows, sediment clumps or pyroclastics, were counted for each sample.

CHECKING THE 250<<2000 μm FRACTION, RE-SIEVING AS NEEDED

Binocular microscope inspection of the 250<<2000 μm fraction showed that on occasion a sample had what seems to be some kind of soluble organic glue that was binding sediments together and not allowing finer particles to pass through the 250 μm sieve. Figure 12 shows two views of the same aggregate with a 5 mm grid in the background. Based on these observations, it was assessed that out of the 143 samples processed, 28 needed to be sieved again after further treatment to remove the organics. Hydrogen peroxide solution (10%, 20 mL) was added to remove the organic matter, as in the methods in Eldrett et al. (2007) and the sample in a glass jar was placed on a warm hotplate for 30 minutes. The fraction was re-sieved at 63 and 250 μm and re-weighed. The weights for the fractions were adjusted accordingly.
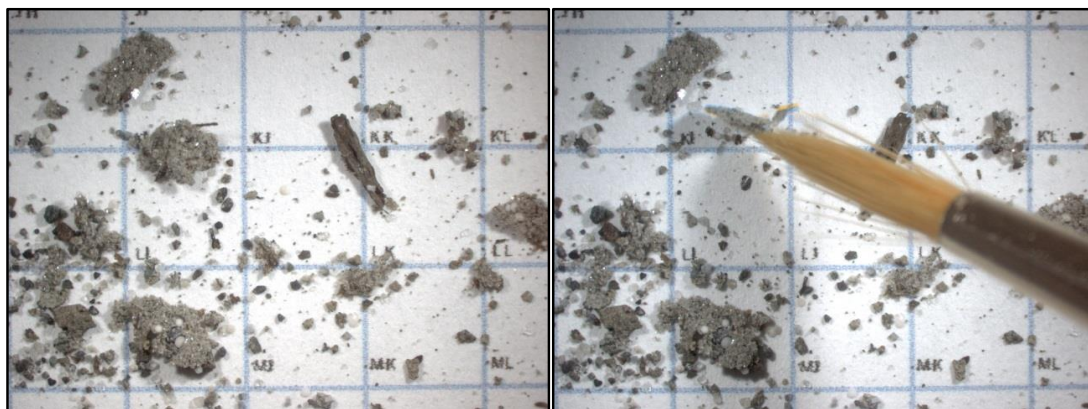
Figure 12. Organic matter binding sediments in the 250<<2000 μm fraction

CHECKING THE 63<<250 μm FRACTION FOR COMPOSITION

Binocular microscope inspection of the 63<<250 μm fraction to check its composition was done on every 4th sample. Rothwell's standard visual composition chart (1989) was used to make a visual estimate of the volume percent of biogenics when the single layer cover of the field of vision was near 100%. Eight samples that had particularly high counts of biogenics in the 250<<2000 μm fraction were also checked.

QUANTIFYING THE ICE RAFTED DEBRIS IN THE 250<<2000 μm FRACTION

Since the 250<<2000 μm fraction has components that are not necessarily ice rafted from the continent or the continental shelf (e.g. biogenics, pyroclastics and authigenics), counts were made of the various components to quantify the fraction of the mass that is clearly siliciclastic. Since the mineralogy of sea ice entrained sediments and glacial ice entrained sediments is strongly dependent on the source area of their entrainment, the count categories include various minerals and polycrystalline rock fragments (lithics). Count categories include: biogenics, plant material, pyritized burrows, pyrite nodules, sediment clumps, pyroclastics, chert, glauconite, feldspar, quartz, mica, unknown minerals, felsic lithics and mafic lithics.

IDENTIFYING COMPONENTS

The following criteria were used for identifying the components of the 250<<2000 μm coarse fraction. Unless otherwise cited, the information is from Rothwell (1989).

Biogenics

Centric and pennate diatoms are a major component of Bering Sea sediments (Aiello and Ravelo 2012), particularly beneath productive areas where upwelling water carrying nutrients mixes with warmer Bering Slope Current water off the shelf break. Radiolarian and foraminifera tests, sponge spicules, and dinoflagellate cysts are also present. The biogenic category includes any whole or partial marine remains that are not terrestrial plant material.

Plant Material

Wood chips are present at Site U1343 (Expedition 323 Scientists 2011b). When found in recent Arctic sea ice, wood chips seem to be associated with river ice (Nürnberg et al. 1994). This category includes any plant material from a continental source.

Pyritized Burrows

Burrows filled with pyrite are found in this size fraction of deep sea sediments (St. John 1999). These are straight and branched cylindrical forms in which pyrite grows in anaerobic environments (Figure 13). Biochemical processes promote the growth of

pyrite where organic sedimentation rates are high. This category includes "worm tubes" that are pyritized similarly and are found in long cylindrical pieces (Rothwell 1989).

Pyrite Nodules

This category includes all the other forms of pyrite found in the sediments whether authigenic or detrital. Pyrite is always opaque, has a brassy yellow metallic luster when reduced, as with hydrogen peroxide, and is tarnished or rusty brown when its surface is oxidized. Framboidal pyrite, with its spheroidal grains, is common in the deep ocean sediments. Pyrite can take on various forms, including irregular shapes and the shape of the organic matter in which it grows. Authigenic pyrite can be found in any shallowly buried sediments whether on the continental shelf or in the deep ocean.
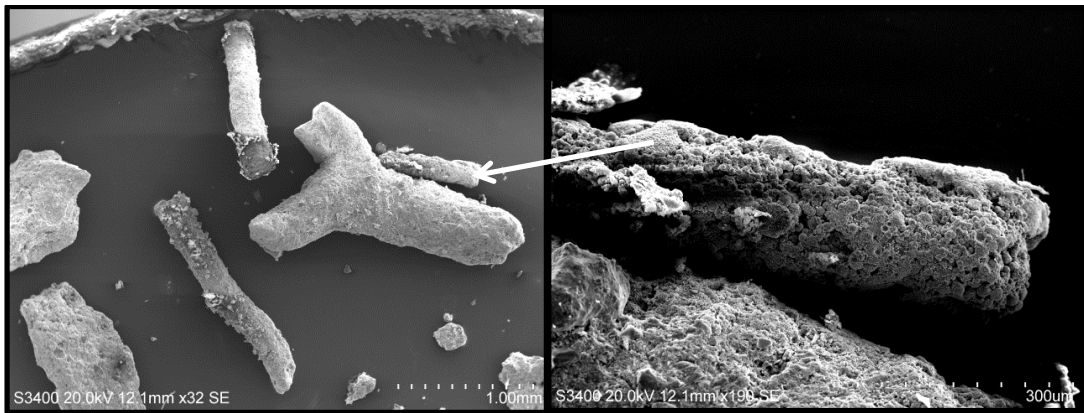
Figure 13. SEM images. Left: pyritized burrows. Right: enlarged surface w/pyrite

Sediment Clumps

These clumps of cemented marine sediment are also referred to in the literature as "clayballs" (St. John and Krissek 1999). They are broken up by ultrasonic disaggregation, but are sometimes very persistent.

Pyroclastics

These are translucent to dark brown glassy shards. They show conchoidal fracture, lines of spherical vesicles and pipe vesicles, and the absence of any crystal structure. They are readily identified by their form. In Arctic and sub-Arctic regions these can be transported by sea ice as well as through air and sea.

Glauconite

Glauconite may be detrital or authigenic. It is common in sedimentary rocks worldwide and has long term stability when not subject to folding (Dapples 1967). It grows in continental shelf sediments in quiet waters >15 m beneath regions of high primary productivity, often in association with pyrite. Like pyrite it can take the shape of organic matter such as foraminifera tests. Generally, its translucent smooth grains are ovoid or lobate, but they can be blocky and irregular. Grain color, from dark green to a pale greenish yellow, varies with grain size which is in the sand-size range but typically between 100 to 500 μm. Grains are usually aggregates of glauconite flakes and crystals such as quartz and pyrite may be imbedded. Glauconite is most often found in warm shelf seas and is generally not thought to grow in marine sediments below 500 mbsl.

Chert

Chert is diagenically recrystallized and indurated biogenic silica. It has conchoidal fracture and can come in many colors. Its fine crystal structure makes the grain appear translucent but not transparent. It is considered a lithic in Dickinson's QmFLt ternary plots for provenance (Dickinson et al. 1983). There is only one source for chert around the Bering Sea, in a belt that runs from the eastern Kamchatka Peninsula to beyond the Koryak Range (St. John and Krissek 1999).

Feldspar

Feldspars are abundant in sediments worldwide, particularly when the source area is cold and/or dry. Marine volcanics and continental weathering can supply feldspars to deep marine sediments, sources that are hard to distinguish. Feldspars are translucent and sub-translucent with a sub-vitreous luster. They are often cloudy from surface alteration of the feldspar to clay. Chipped grains may show uneven fracture and the planar cleavage which is good in two directions. These features can usually be used to distinguish feldspar from quartz. Feldspar grain size is generally <500 μm but crystals can grow larger. Grain color varies from white and pinkish to grey, depending on the chemical composition.

Quartz

Quartz is ubiquitous in detrital sediments and is nearly always continentally derived. Quartz is particularly abundant on high latitude continental shelves. North Pacific deep marine sediments are also high in quartz, similar to the Atlantic. The abundance of quartz seems to reflect the ratio of land drainage area into the basin, with shelf areas near rivers being lower in quartz since rivers tend to carry more of the finer sediments. Quartz is a main components of the >63 μm siliciclastic fraction in Arctic sea ice (Nürnberg et al. 1994). Sand-sized sediments are a significant portion of the Bering Sea shallow continental shelf (Sharma 2012). These are likely to include quartz grains.

Quartz is transparent and colorless with its common inclusions sharply defined. It has a vitreous luster and no alteration, although wind transported grains can be stained by hematite and make it appear turbid. It has a lack of cleavage, conchoidal fracture, and a large grain-size range. Horizontal striations from growth planes, and open embayments are found on the surface of grains. The transparency of the grain and the lack of alteration are distinguishing features.

Mica

Mica is continentally derived and is primarily found on the shelf, slope and rise. Muscovite, one form of mica, is resistant to weathering and fragmentation, but can be shredded to irregular flecks. Its grain size is generally less than 1000 μm and it tends to come in flakes larger than the surrounding grains. Muscovite is colorless, but biotite, another form of mica, can be greenish to brown.

Unknown Minerals

This category is for unidentified monocrystalline minerals. Biogenics and lithic fragments have their own categories.

Felsic Lithics

In high latitude sedimentary basins, polycrystalline rock fragments (i.e. lithics) are more likely associated with glacial ice than sea ice. Rock that is entrained by alpine glaciers through abrasive processes (Herman et al. 2015) more likely undergoes physical weathering, fragmenting into lithics (Taber 1943); conversely, polycrystalline rock fragments that are transported by rivers to the continental shelf are exposed to chemical

processes that weather out the more soluble minerals (Molén 2014) and dissociate the polycrystalline rocks into single mineral components. Accordingly, when lithics are in greater abundance, a continental glacial source is more likely, and the associated transport by icebergs.

Felsic lithics are grain-size rock fragments that are poorer in iron and magnesium and richer in silica bearing minerals like feldspar. They tend to be lighter in color and solidify from a cooler magma. Quartz, potassium feldspar, and muscovite are felsic minerals. Granite and rhyolite are examples of these lighter felsic rocks. Felsic lithics would more likely be continentally derived.

Mafic Lithics

Mafic lithics are grain-size rock fragments that are richer in magnesium and iron and poorer in silica bearing minerals. They tend to be darker in color and come from hotter magma like that which forms the oceanic crust. Biotite, amphiboles, and pyroxenes are mafic minerals. Basalt and gabbro are examples of these darker mafic rocks. Mafic lithics would more likely come from a marine volcanic arc.

IDENTIFYING THE IRD IN THE 250<<2000 μm COARSE FRACTION

In order to quantify the IRD, components that could have been transported by a means other than ice, or that grew in place need to be ruled out. This eliminates biogenics, plant material, pyroclastics, and authigenics that grow in deep marine sediments: the pyrite nodules, pyritized burrows, and sediment clumps. Since the U1343 site is sheltered from mass wasting and contour currents, the remaining siliciclastics are interpreted to have been transported by glacial ice or sea ice. The portion of the 250<<2000 μm coarse fraction that is siliciclastic (siliciclastic count fraction) is the sum of the chert, glauconite, quartz, feldspar, mica, unknown minerals, felsic lithics and mafic lithics, divided by the total count.

THE COUNTING PROCEDURE

Counts of 73 samples from 898 to 872 ka, which includes most of glacial MIS 22 from 900 to 866 ka (Lisiecki and Raymo 2005), were made using a Leica S8 APO binocular microscope starting at a magnification of 48x (3.0 zoom position for 3x, M_O of

1.6x, M_E of 10x). To assist in making identifications, the magnification can be increased to 128x by shifting the zoom to 8.0.

At least 200 particles of each sample were counted. For comparison, to get a statistically sound sampling of the various components in traditional petrographic point counts of sandstones in thin sections, 300 points are counted (Ingersoll et al. 1984). In this study, a 200 count minimum was chosen to maintain statistical soundness and yet consider the time needed to count many samples.

Counts were done by randomly distributing the sample through scattering it onto a plastic square dish lined with paper imprinted with a 5 mm square grid. The rows and columns of the grid were labeled alphabetically to keep track of the counting process (Figure 14). The components were identified and categories counted starting at a middle row on the left and proceeding to the right by square. Any component that was more than 50% within the square was counted. Two laboratory counters kept a running total of the counts. If the 200 total count minimum was not reached by the end of the row, a row was skipped and the count proceeded from the right to the left square by square. This continued until at least 200 particles were counted. If the sample was overwhelmed by one component, correspondingly more counts were made of that sample. The only exception to this sampling method was sample U1343E-25H-5W, 62.0-64.0 cm at 895.6 ka in which all components were counted, but only totaled 95.
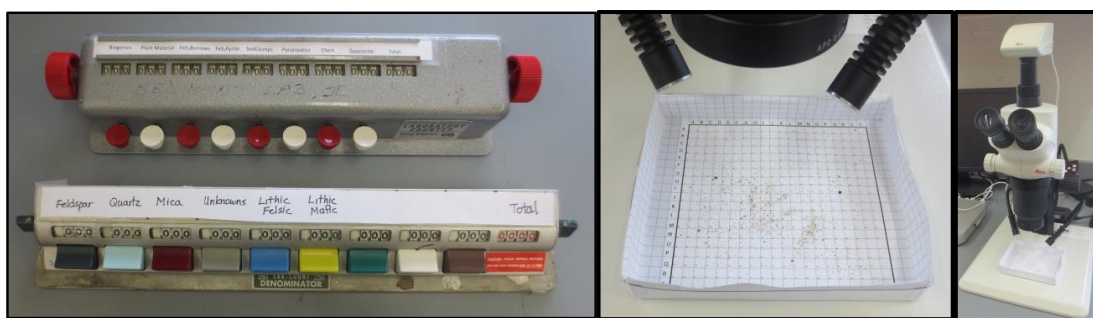
Figure 14. The counting procedure set up

ABUNDANCE AND MASS ACCUMULATION RATE CALCULATION PROCEDURE

The abundance of a fraction or component is generally its weight % of the initial dry bulk sample. (As explained before, the dry bulk samples were weighed by Kender's

lab before sieving.) This percent can be determined by weight, or estimated by count or estimated by making a visual determination of the % volume, or, as in the case of this study, by a combination thereof. Abundances were calculated for the 63<<250 μm fine fraction by using the weight of the fraction. The 63<<250 μm fine siliciclastic abundance was found by making a visual estimation of the volume % of the biogenics in the 63<<250 μm fine fraction, and adjusting the abundance accordingly. Abundances were calculated for the siliciclastic portion of the 250<<2000 μm coarse fraction using the total weight of all components of the coarse fraction and counting a subset of the fraction to get the siliciclastic count fraction. The siliciclastic abundance was found by making the assumption that all the sediment components have approximately the same density, and multiplying the siliciclastic count fraction by the weight % of the 250<<2000 μm coarse fraction.

The abundance of gravels >2 mm was determined by a count normalized by the weight of the dry bulk sample. Because the gravels vary in size and one large clast can greatly affect a weight % abundance for a sample, a normalized count was thought to be a better indication of the extent of ice transport for this size component.

Mass accumulation rates (MAR's) are used rather than relative abundances because 1) they take into account the local linear sedimentary rate (LSR), and 2) siliciclastic MAR's are independent of the LSR of other biogenic components (St. John 1999). MAR's use dry bulk density (DBD) measurements. Calculation procedures for abundances and MAR's are found in Table 2.

Table 2. Abundance (wt % and count) and MAR Calculation Procedures

Parameter	Calculation Procedure
siliciclastic count fraction	= count of siliciclastics / total count of subsample
250<<2000 μm wt%	= 250<<2000 μm sample weight / dry bulk sample weight
63<<250 μm wt%	= 63<<250 μm sample weight / dry bulk sample weight
coarse siliciclastic wt%	= 250<<2000 μm wt% x siliciclastic count fraction
fine siliciclastic wt%	= 63<<250 μm wt% x estimate of siliciclastic volume %
gravel count abundance	= count of gravels / dry bulk sample weight
coarse siliciclastic MAR	= coarse siliciclastic wt% x DBD x LSR
fine siliciclastic MAR	= fine siliciclastic wt% x DBD x LSR

OBSERVING QUARTZ GRAIN CHARACTERISTICS WITH THE SEM

In addition to compositional differences between the GIRD and SIRD on account of their varying sources, grain features will also differ according to their various weathering histories. Because quartz is hard and retains grain features, quartz grains have been used to determine transport methods (Molén 2014). Quartz grains entrained through abrasive mechanisms by alpine glaciers will show different features than grains entrained by sea ice from a shallow marine shelf environment (Dunhill 1998). The grains are observed to determine their maturity.

Quartz grains from the 63<<250 μm fraction were observed using a Hitachi Scanning Electron Microscope (SEM) at various magnifications as needed to identify grain features. Samples from 8 different times in the record were chosen: 2 in MIS 23, 4 in MIS 22, and 2 in MIS 21 (Table 3). At least 20 quartz grains randomly selected from each sample were mounted on an aluminum stub similar to methods in St. John (2008). For each grain, three principal aspects of particle shape were noted: basic form, edge roundedness, and surface texture (Boggs 2012). Power's chart of grain images for estimating roundedness of high and low sphericity grains was used (Powers 1953). The basic form of high or low sphericity was assigned a value of 1 or 2. Power's categories for edge roundedness were assigned values from 1 to 6. Surface texture, as related to freshness, was assigned categories and values from 1 to 5. Grain surfaces can be altered by solution, precipitation, and abrasion. Fresh surfaces may be exposed by breakage fracturing of a grain or by a mineral falling out leaving an embayment. Molén (2014) summarizes these processes in his work on using quartz grain features to classify diamicts like glacial till. For each of these aspects of grain shape, higher values indicate fresher, i.e. less mature grains; lower values indicate more wear and weathering, i.e. more mature grains. See Table 4 for a summary of the assigned categories and values for these aspects of particle shape.

Quartz grains that undergo glacial transport weather differently than quartz grains that undergo fluvial transport and are subsequently entrained in sea ice from a shallow continental shelf marine environment (Dunhill 1998). More angular grains with sharper edges and fresher surfaces would be more characteristic of glacial transport, and more spherical grains with worn edges and weathered surfaces would be more characteristic of

fluvial transport (Molén 2014) and residence time on the continental shelf. Dunhill's study (1998) of modern SIRD and GIRD quartz grains in the 180<<300 μm size range concluded that they could be differentiated by the absence or presence of groups of grain features; breakage blocks indicate glacial ice transport. The study found no statistical difference in in form, roundedness, or surface texture between GIRD and SIRD. However, others commonly found breakage blocks in SIRD (Tantillo et al. 2012). Though rounded quartz grains found in greater abundance on a region of the Arctic shelf have been interpreted to indicate a history of fluvial transport and subsequent resuspension and entrainment into sea ice (Nürnberg et al. 1994), it may be difficult to determine the mode of ice transport by quartz grain features.

Table 3. Source and Age of Quartz Grain Samples for SEM Analysis

Sample Source	Age (ka)	Glacial/Interglacial MIS Stage	# of quartz grains
U1343C-23H-3W, 45.0-47.0 cm	859.8	Interglacial MIS 21	23
U1343C-23H-4W, 46.0-48.0 cm	864.2	Interglacial MIS 21	24
U1343E-25H-2W, 08.0-10.0 cm	873.3	Glacial MIS 22	26
U1343E-25H-2W, 94.0-96.0 cm	877.1	Glacial MIS 22	20
U1343E-25H-3W, 30.0-32.0 cm	880.9	Glacial MIS 22	25
U1343E-25H-5W, 45.0-47.0 cm	894.9	Glacial MIS 22	23
U1343E-25H-6W, 68.0-70.0 cm	902.5	Interglacial MIS 23	31
U1343E-25H-7W, 62.0-64.0 cm	908.9	Interglacial MIS 23	26

Table 4. Categories for Quartz Grain Shape, Abbreviations, and Assigned Values

Basic Form Abbreviation & Assigned Value		Edge Roundedness Abbreviation & Assigned Value		Surface Freshness[*] Abbreviation & Assigned Value	
High Sphericity, HS 1		Well-Rounded, WR 1		>80% Altered, AL 1	
Low Sphericity, LS 2		Rounded, RN 2		60<<80% Altered, AL>F 2	
		Sub-Rounded, SR 3		40<<60% Altered, AL=F 3	
		Sub-Angular, SA 4		20<<40% Altered, AL<F 4	
		Angular, AN 5		<20% Altered, F 5	
		Very Angular, VA 6			

[*]If not Altered, it is Fresh

CHAPTER 3

RESULTS

THE SILICICLASTIC FRACTION (>63 μm) AT SITE U1343 DURING THE MPT

Even though sediment from site U1343 has deposited in a pelagic setting, the >63 μm siliciclastic component is a significant portion of the bulk sediment during the MPT. Examples of compositional variability are shown in Figure 15. More examples are shown in Appendix A. Gravels >2 mm are relatively common, with a maximum of 11 clasts in one 29 g sample (0.379 counts/g), and averaging 0.022 counts per gram of bulk sediment. The abundance (wt%) of medium, coarse, and very coarse sand-size siliciclastics, 250<<2000 μm (hereafter referred to as coarse sand), ranges from 0.023% to 0.96% of the bulk sample, averaging 0.12%. The abundance (wt%) of the fine and very fine sand-size fraction, 63<<250 μm (hereafter referred to as fine sand), ranges from 5.4% to 21.7%, averaging 10.4% of the bulk sample. The fine sand is nearly two orders of magnitude more abundant than the coarse sand and is the most significant component of the >63 μm siliciclastics. Abundances of gravel, coarse sand, and fine sand for this data set are shown in Figure 16. Tables of data used to calculate these abundances are found in Appendix B. Notice in Figure 16 that the abundances from when the splice of U1343C and U1343E overlap are fairly consistent, and if the overlap where slightly greater, they would align even more.

ABUNDANCE OF GRAVELS

Gravel-size siliciclastics are generally found throughout the record, with the exception of the intervals from 869 to 866 ka, and from 865 to 862 ka. After 869 ka gravels are less abundant than before (Figure 16). Four peaks and a more consistent presence of gravels are found in the interval between 888 and 874 ka, with the highest abundance just after 880 ka. Two peaks also occur earlier in the record at about 907 and 903 ka, with a lower abundance following from 902 to 888 ka.

ABUNDANCE OF COARSE SANDS

There are coarse siliciclastics throughout the 898 to 872 ka record (Figure 16). Before 888 ka the abundance is lower, averaging less than 0.1%, but after 888 until 875

ka the abundance is generally higher than 0.1%. Within the period of higher abundance, three lows occur at 884, 880, and 878 ka. At 875 ka the abundance decreases sharply. The period of higher abundance of the coarse sands comes in four pulses that match up with the four higher abundance peaks in the gravels. These abundances are for the coarse siliciclastics whose weight fraction of the 250<<2000 μm components is estimated by doing counts and separating out the biogenics, authigenics, and pyroclastics.
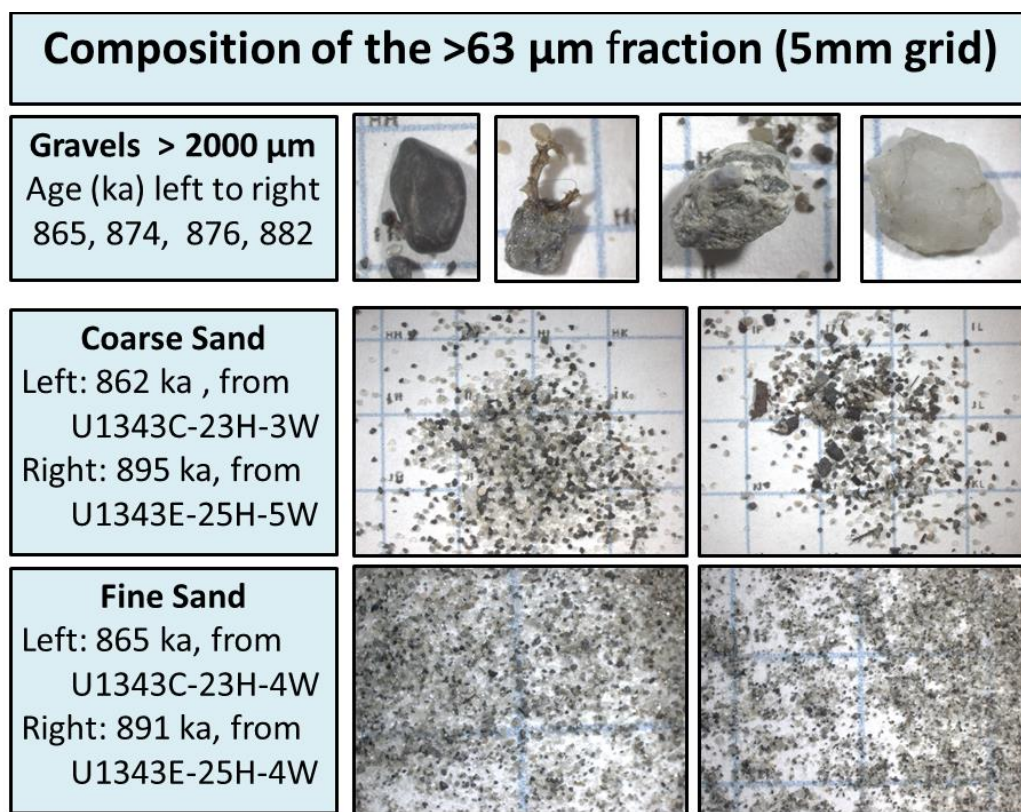
Figure 15. Examples of the composition of various sizes of the >63 μm siliciclastics

ABUNDANCE OF FINE SANDS

The visual investigation with a binocular microscope of every fourth sample of the 63<<250 μm size fraction confirmed that with few exceptions, the siliciclastics are 98% or more of the 63>>250 μm fraction (data in Appendix B). The investigation also shows that for the samples that have more than 2% biogenics, the overall abundance of the 63>>250 μm fraction is low. In other words, peaks of fine sand accumulation are

virtually all composed of siliciclastic particles. Similarly, pyroclastic counts in the 250<<2000 μm coarse fraction only show one peak at 882 ka, at a time when the fine sand abundance is at a minimum; so the peaks of fine sand are likely to have an insignificant contribution of the finer 63>>250 μm pyroclastic component. Sediment clump counts also show no pattern of contribution to the abundance of the fine sand. The 63>>250 μm fraction abundance (wt%) is a good approximation of the abundance of the fine siliciclastics at site U1343.
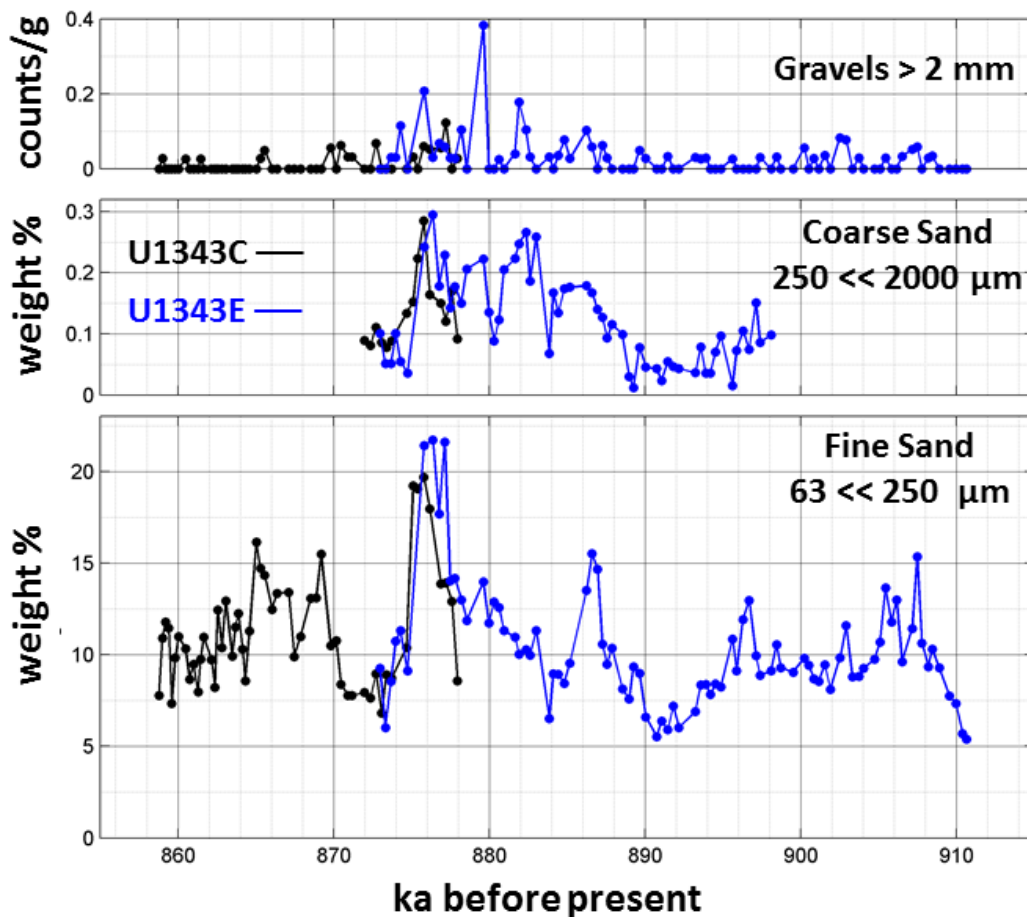
Figure 16. Abundances for gravels, coarse sands, and fine sands at site U1343

The fine sand composes a significant portion of the sediment, always more than 5%. Peaks of more than one sample are found around 906, 896, 887, 876, and 866 ka (Figure 16). The highest of these peaks is centered about 876 ka, when the abundance of this fraction is more than 20%. This peak, followed by a period of decrease in abundance

can be seen in samples from both Holes C and E. A similar peak is found at the same time in the coarse sands. Another peak around 887 ka reaches an abundance of over 15%. The abundance of the fine sand grows steadily as it approaches these two peaks, then falls steeply. After 865 ka the abundance of fine sand shows more variability, but still maintains its average around 10%. The periods from 895 to 888 ka and from 874 to 870 ka have a relatively low abundance of fine sand, <10%, and are approximately concurrent with periods of low abundance in the coarse sand and the gravels.

MASS ACCUMULATION RATES FOR COARSE SANDS AND FINE SANDS

Two dry bulk density (DBD) measurements were made for U1343 between 910 and 860 ka by Expedition 323 Scientists (2011). One DBD of 2.732 g/cm^3 corresponds to 873 ka. The other DBD of 2.625 g/cm^3 corresponds to 911ka, before the coarse sand record begins. Both were taken in the period when the linear sedimentation rate (LSR) is 22.6 cm/ka and were taken at times when the siliciclastic abundance for our record was relatively low. Using the average abundance for the fine sand (10.4%), and the average of the two DBD's (2.678 g/cm^3) gives an average fine sand MAR of 6.2 g/cm^{2}ka. The average abundance for the coarse sand (0.12%) and the DBD within that record (2.732 g/cm^3) gives an average coarse sand MAR of 0.074 g/cm^{2}ka. Table 5 gives a summary of these calculations. For MAR calculation procedures, see Table 2.

Table 5. Mass Accumulation Rates for Fine Sand and Coarse Sand

Age (ka)	DBD g/cm^3	LSR cm/ka	Coarse Sand Average Abundance wt%	Fine Sand Average Abundance wt%	Coarse Sand MAR g/cm^{2}ka	Fine Sand MAR g/cm^{2}ka
873	2.732	22.6				
911	2.625	22.6				
872-898	2.732	22.6	0.12		0.074	
860-911	2.678	22.6		10.4		6.2

Coarse Sand are the 250<<2000 μm siliciclastics; Fine Sand is the 63<<250 μm fraction

QUARTZ, GLAUCONITE, FELDSPAR, AND LITHIC ABUNDANCES

Abundances (wt%) of quartz, glauconite, feldspar, total lithics, felsic lithics and mafic lithics, calculated in the same manner as the coarse sand abundances (i.e. by

counts), are shown in Figure 17. The red vertical lines drawn on the figure at 889, 883.5, and 880 ka indicate times of relative low abundance in gravels, coarse sands, and fine sands (see Figure 16). They also separate periods of general changes in the abundance of the components. The record from 898 to 872 ka includes most of glacial MIS 22 which begins at 900 ka and ends at 866 ka (Lisiecki and Raymo 2005). Data tables for the counts are found in Appendix C. Notice in Figure 17 that the component abundances when the splice of U1343C and U1343E overlap are fairly consistent and if the overlap where slightly greater, the two different time series would align even more.
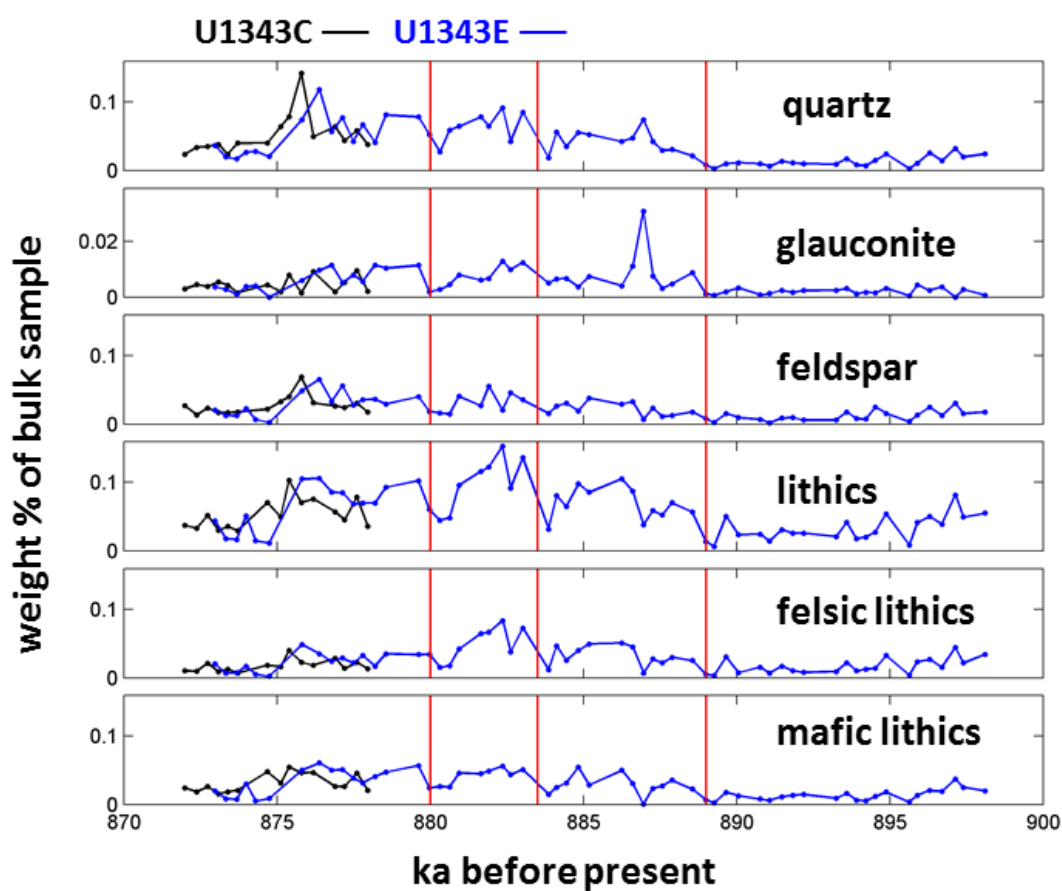
Figure 17. Abundance of siliciclastic components in 250<<2000 μm fraction

Quartz abundance from 898 to 889 ka is lower. It tends to increase over the glacial time period with a peak at 887 ka and a higher peak at 876 ka before the abundance decreases, but not to the same low level as at the beginning of the glacial.

Glauconite is much less abundant than the other components. Note the difference in the scale. It increases slightly over the course of the glacial, with a significant peak at 887 ka, at the same time when there is a peak in quartz abundance.

Feldspar abundance does not change as much across the glacial as the other components. It is comparable to the mafic lithics in this way.

Lithic abundance changes the most through the record, comparable to the changes in quartz abundance, but reaching a maximum peak between 883 and 882 ka, rather than at 876 ka.

Felsic lithics seem to be more abundant in the beginning of the glacial, compared to mafic lithics which maintain their abundance.

These relative abundances give inputs to the sediment, but they do not show changes in the relative inputs of the different components. For that, relative percent of three components will be plotted on a ternary plot, similar to Dickinson's plots for provenance (Dickinson et al. 1983). The ternary plot of quartz, feldspar, and lithics in Figure 18 shows the relative composition of these components in the coarse siliciclastics for the 4 age groups outlined by the red lines in Figure 17. The diagram also shows a linear regression line between the three components which approximates the change in relative composition in time. The ternary plot shows that the relative percentage of quartz (compared to total quartz, feldspar and lithics) increases over the glacial, even as the relative percentage of lithics decreases. The feldspar percentage is variable but generally does not change.

A different, non-standard, ternary plot has been created to describe relative changes in abundance of the mafic and felsic components within the lithic fraction: the plot shows the percentage of quartz plus glauconite at the top and mafic lithics and felsic lithics in the other two corners. Our rationale for lumping together quartz and glauconite is that they both mainly represent shelf sources: as discussed previously, single quartz crystals require chemical weathering and suggest transportation by non-glacial media, and glauconite forms in situ in the continental shelf. The plot shows a continuing decrease in the relative percent of felsic lithics even as the percentage of the sum of quartz and glauconite grains increases (Figure 19). The mafic lithics seem to have a

stable, though variable, percentage throughout the glacial. A regression line also shows these changes.
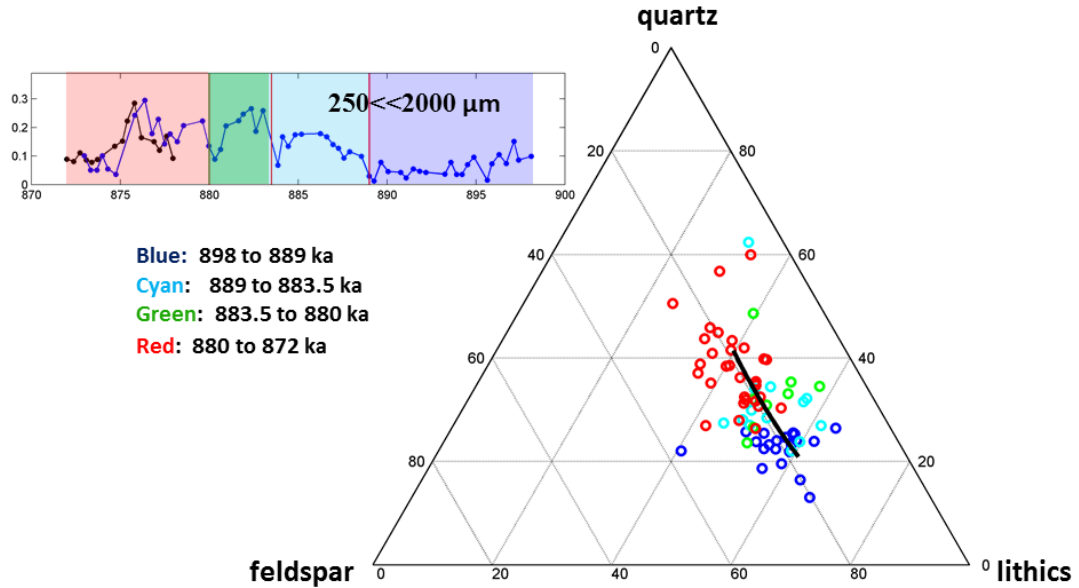
Figure 18. Quartz/Feldspar/Lithics plot for change in relative composition
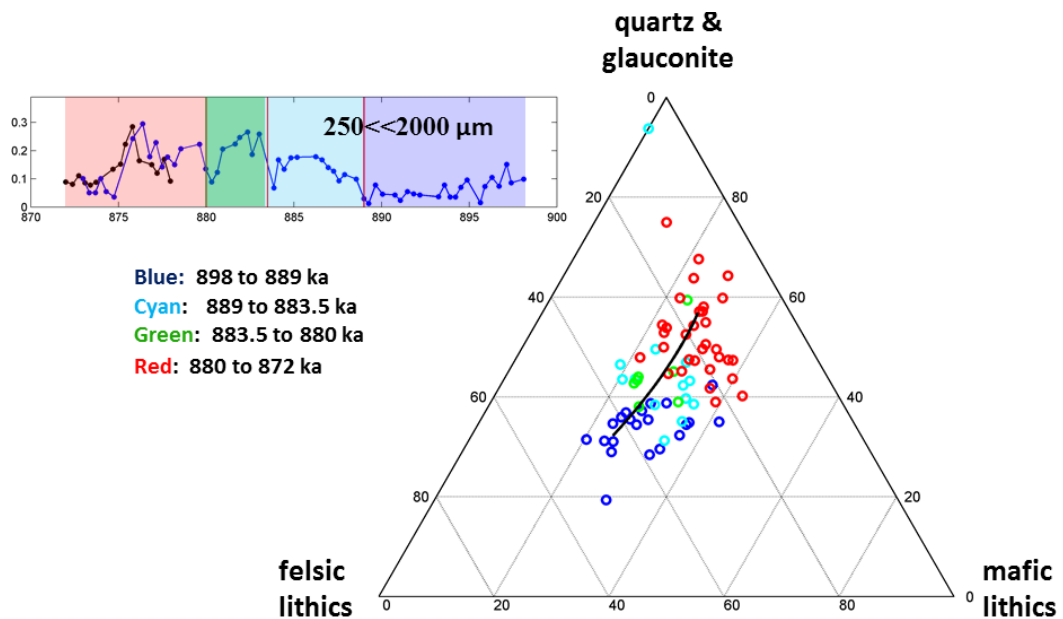
Figure 19. Ternary plot showing relative change in felsic and mafic lithics

FEATURES OF QUARTZ GRAINS FROM THE 63<<250 μm FRACTION

Over 198 grains from eight samples were checked for their form, edge roundedness and surface characteristics. The grains in the high sphericity category (107 grains) show little other difference in form than the grains in the low sphericity category (91 grains) (Figure 20). In general grain edges tend to be more angular than rounded, and the grain surfaces tend to be more altered than fresh. For the sample source, see Table 3; for the key to the categories, see Table 4. Data tables for the quartz grain characteristics are found in Appendix D.

Changes in the grain form can be noticed by averaging the assigned values for edge roundedness and for surface texture for each sample, and comparing the averages at various samples over the record (Figure 21). Grains from the younger samples tend to be more angular and less altered, and yet the relative number of high sphericity grains increases. Histograms showing the distribution of the edge angularity and surface freshness for the grains in each sample are found in Figure 22.
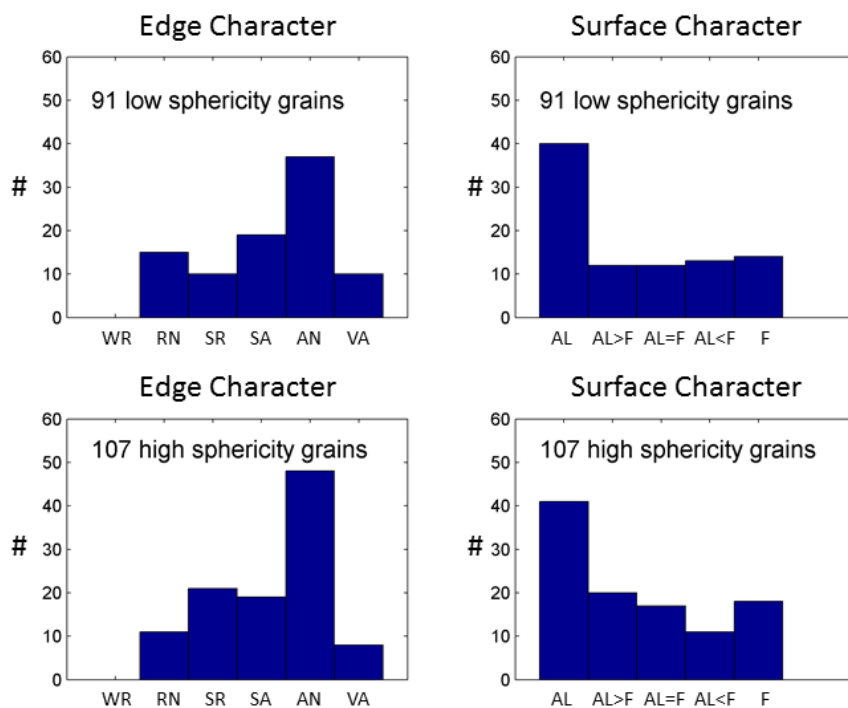
Figure 20. Distribution of quartz grain edge and surface characteristics
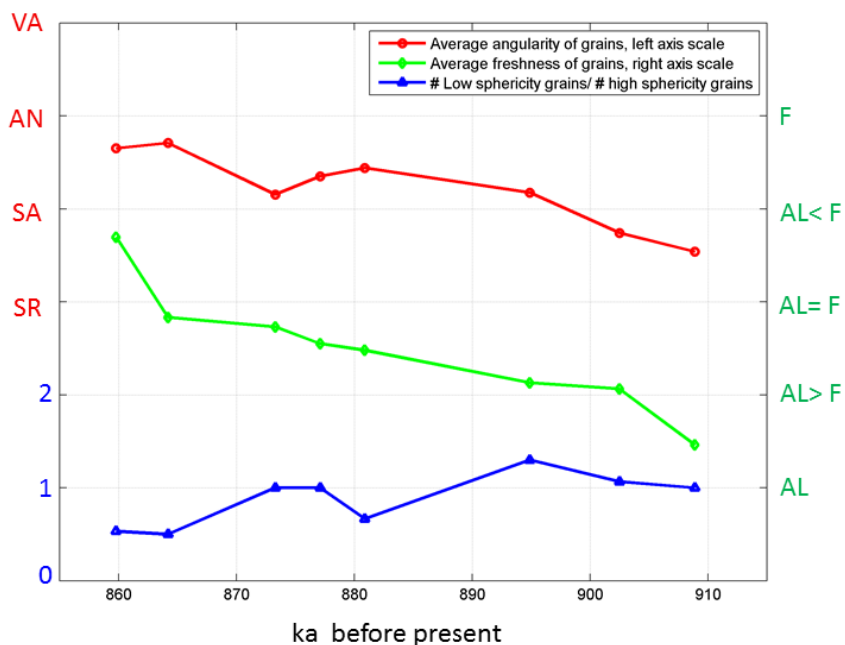
Figure 21. Change in quartz grain form, edge, and surface characteristics
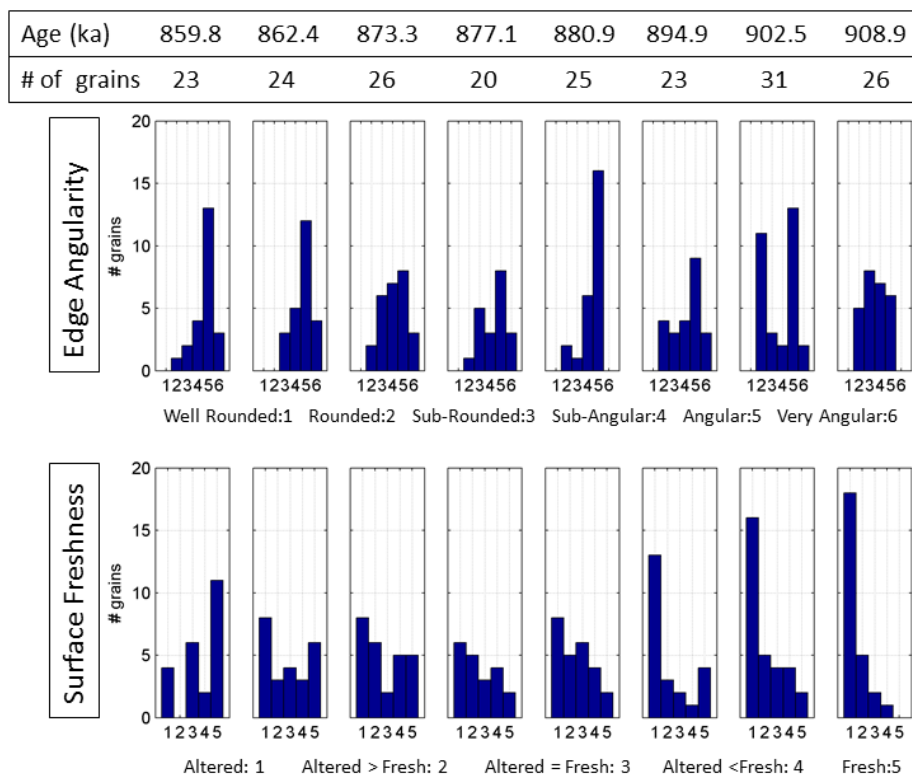
Figure 22. Histograms of quartz grain edge and surface characteristics at U1343

CHAPTER 4

DISCUSSION

TRACKING GLACIAL ICE AND SEA ICE

THE PARTICLE SIZE DISTRIBUTION OF GLACIAL AND SEA ICE SEDIMENT

The particle size distribution of the sediment in glacial ice and sea ice is somewhat similar. Both entrain mainly clay- and silt-size particles, and both have a less abundant fraction of sand-size siliciclastics (Dunhill 1998). However, sediment entrained by modern glacial ice is less sorted than sediment entrained by modern sea ice, particularly in the coarser fractions (Nürnberg et al. 1994). Although coarse sand and gravel size siliciclastics are much less frequently entrained by sea ice compared to glacial ice, modern sea ice can entrain large clasts (Nürnberg et al. 1994); so the size of a clast alone cannot be used to distinguish rafting by glacial ice from rafting by sea ice, the particle size distributions must be considered (Dunhill 1998). Laser particle size analysis of hemipelagic sediments that are a mix of biogenic and siliciclastic components and have a broad range of particle types, sizes and shapes could be difficult, especially when the goal is to describe the particle size distribution of the sand-size siliciclastic fraction. One of the reasons is that with the typical small volume of sample used for the analyses (~1g) larger particles tend to be selectively less represented.

Ternary diagrams using estimated weight percents of sand-, silt- and clay-size siliciclastic fractions of modern sea ice and glacial ice show the differences in the particle size distributions between these two types of ice rafting media (Nürnberg et al. 1994; Dethleff and Kuhlmann 2009). Actually weighing the size fractions is only possible when there is enough mass to be measured. Dunhill (1998) analyzed many modern Arctic glacial ice and sea ice samples by separating and weighing the phi interval (Wentworth scale) of the siliciclastic fractions (Figure 23). These show a better sorting for sea ice and a difference in the relative weight of the coarser sands and gravels: modern sea ice is much less likely to carry gravels >2 mm; the weight percent below phi of 1 is zero. Medium, coarse, and very coarse sand (250<<2000 μm) is only 0.2% of the total weight, fine and very fine sand (63<<250 μm) is 4.6%, silt and clay together are 95.2%. Modern

glacial ice is more likely to carry the coarser siliciclastics. Gravels >2 mm are 4.6% of the total weight, medium, coarse and very coarse sand is 7.6%, fine and very fine sand is 16.9%, and silt and clay together are 70.8%. The ratio of the coarse sand to the fine sand in Arctic glacial ice is 0.45. In Arctic sea ice the ratio is 0.04. (Percentages and ratios re-calculated based on data presented by Dunhill (1998) shown in Figure 23).

Single phi (φ) weight percent histograms from Dunhill (1998)
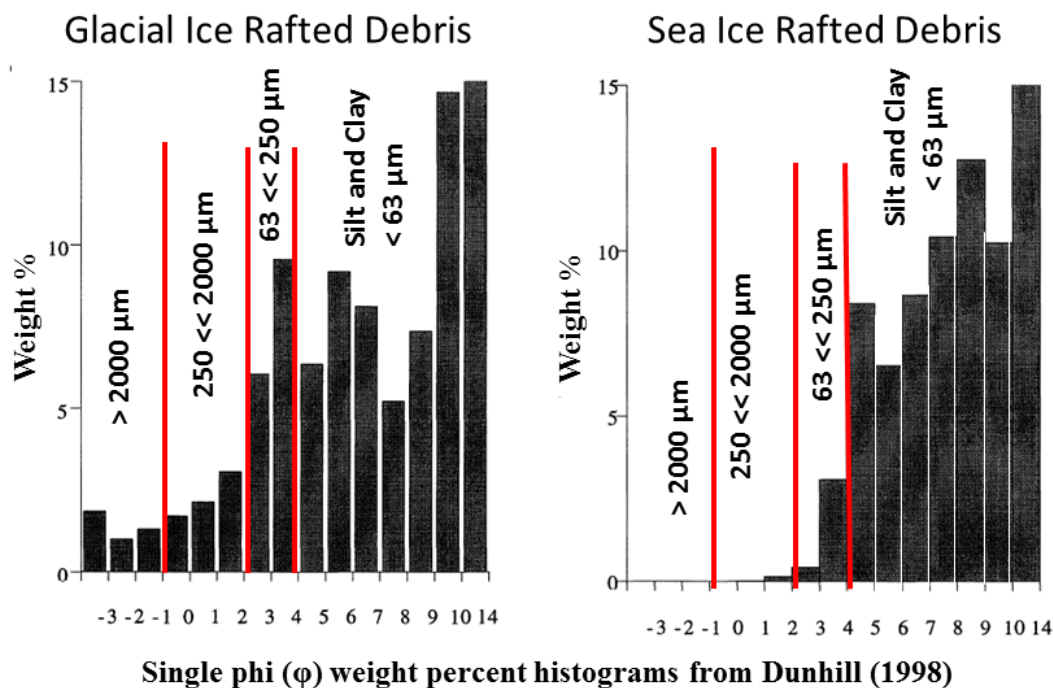
Figure 23. Grain size distributions (wt%) for glacial and sea ice rafted siliciclastics

The weight percent histograms of GIRD and SIRD in Figure 23 can be used to better interpret the relative contributions of glacial ice and sea ice to the sand-size and larger siliciclastics in the mid-Pleistocene sediments at Bering Sea site U1343. Siliciclastic sediment in glacial ice and sea ice will vary according to the entrainment mechanism, the entrainment source, and the glacial/interglacial stage. Once entrained, the sediments may be further sorted during transport by melting processes and redistribution in and on the ice (Aiello and Ravelo 2012). After ablation, as the sediments fall through the water column they will also be winnowed by currents. Keeping in mind that the weight percent histograms in Figure 23 are a rough estimate of glacial and sea ice contributions to the sediments at Bering Sea site U1343, the difference between GIRD

and SIRD in the abundance of gravel and the weight percent of the various size fractions will be used as a basis for tracking sea ice and glacial ice.

USING PARTICLE COUNTS AND PERCENT WEIGHT

According to the criteria established in the previous section, we interpret a greater abundance (count/g) of gravels (> 2 mm) as a period when glacial ice rafted debris (GIRD) is more likely. A greater abundance of the 250<< 2000 μm fraction may also point to a higher contribution by GIRD, or, alternatively, to the co-occurrence of both GIRD and sea ice rafted debris (SIRD). When the abundance of the fine sand 63<<250 μm fraction is high at a time when the presence of gravels is low or absent, then SIRD is more likely. It is worth noting that these criteria could make difficult identifying sea ice free periods when GIRD is dominant. The criteria for tracking the likely contribution of GIRD and SIRD in the sediments are summarized in Table 6. A difference in depositional pattern of the > 2 mm gravels and the 63<<250 μm fine sand fraction through time would reflect a difference in the transport mechanism.

Table 6. Tracking Glacial Ice and Sea Ice in U1343 Sediments Using IRD

	> 2000 μm Gravel	250 << 2000 μm Coarse Sand	63 << 250 μm Fine Sand
SIRD	absent	low	high
GIRD and SIRD	present	high	high
GIRD	present	low	low
No GIRD or SIRD	absent	absent	absent

Note: Sea ice rafted debris (SIRD) and Glacial ice rafted debris (GIRD).

To compare the data from Site U1343 with the grain size distributions presented by Dunhill (1998) (Figure 23) and interpret the relative contribution of SIRD vs GIRD, the mass of the 63<<250 μm fraction is divided by the count of gravels >2 mm for each sample (Figure 24): when this ratio is higher, sea ice is more likely. However, there are two caveats with this method: 1) it heavily weights gravel counts that are fairly low and infrequent, and 2) when the gravel count is zero, the method is undefined. To address the first issue, the interpretation of sea ice is based on both the aforementioned ratio and by considering the abundance (wt%) of the fine sand fraction (Table 6): higher abundance of the fine sand is a strong indication of the presence of sea ice, particularly when the >2

mm counts are low. To deal with the second issue, when the gravel count for a sample is zero, the fine sand fraction is divided by 0.8 instead of zero. This shows the effect of the low count but does not inflate the ratio.

Provenance based on petrographic composition of the 250<<2000 μm siliciclastic fraction and characteristics of 63<<250 μm quartz grains can be used to give support to the interpretation of contributions of GIRD and SIRD. We suggest that when quartz and glauconite are higher in abundance, a continental shelf source is more likely, and therefore transport occurred by sea ice rafting rather than by glacial ice rafting. The rationale for this interpretation is that both quartz grains and glauconite particles are more likely to have been entrained by ice on the continental shelf rather than in a mountainous region where entrainment by glaciers occurs. The microscopic surface features of quartz grains from the 63<<250 μm fraction can also provide further evidence in support of the interpretation of the siliciclastic fraction because of the differences in weathering history between GIRD and SIRD.

TRACKING GLACIAL ICE AND SEA ICE AT U1343 IN THE BERING SEA

PARTICLE SIZE DISTRIBUTIONS OF THE >63 μM SILICICLASTIC FRACTION

The ratio of the weight percent of coarse sand and fine sand in the Bering Sea U1343 sediments averages 0.01, suggesting a larger abundance of fine sand when compared to Arctic SIRD (0.04) and Arctic GIRD (0.45) (from Dunhill 1998). This suggests that sea ice is the primary source of the siliciclastic sand-size sediment, and that entrainment methods in the Bering Sea transport a great proportion of the finer fraction. The particle size distributions of Bering Sea sediments retrieved during IODP Expedition 323 from sites off the continental slope show higher sorting than sediment from Bowers Ridge. This is interpreted to indicate a greater sea ice input to the sediment off the continental slope (Aiello and Ravelo 2012). Expedition 323 scientists used the presence of pebbles and coarser drop stones (>4 mm) to indicate the presence of icebergs at Bering Sea sites (Takahashi et al. 2011). We will use the presence of gravels >2 mm to indicate the presence of icebergs, and the higher abundance of fine sand when the gravel counts are lower to indicate the presence of sea ice. Figure 24 shows the graph of the fine sand weight divided by the gravel count that is used to track the presence of sea ice (Recall

that when the count is 0, the fine sand is divided by 0.8). The peaks in this graph, according to our criteria, suggest times when there is more sea ice present. The peaks in the abundance of fine sand found at 906, 896, 887, 876, and 866 ka (Figure 16) that is likely to be SIRD lend support to this interpretation. The three middle red lines in Figure 24 are at times when abundance of all three particle size fractions are low (see Figures 16 and 17). The right red line is at 900 ka, which corresponds to the boundary between MIS 23 and MIS 22. The left red line at 870 ka is the middle of the local steep change in $\delta^{18}O$ (Figure 9), when the fine sand abundance is also increasing (Figure 16). Notice that the time series (black from U1343C and blue from U1343E) do not overlap very well. As mentioned previously, this may be an indication that the splice needs to overlap more and the correlated core depths below sea floor (m ccsf) need to be adjusted.
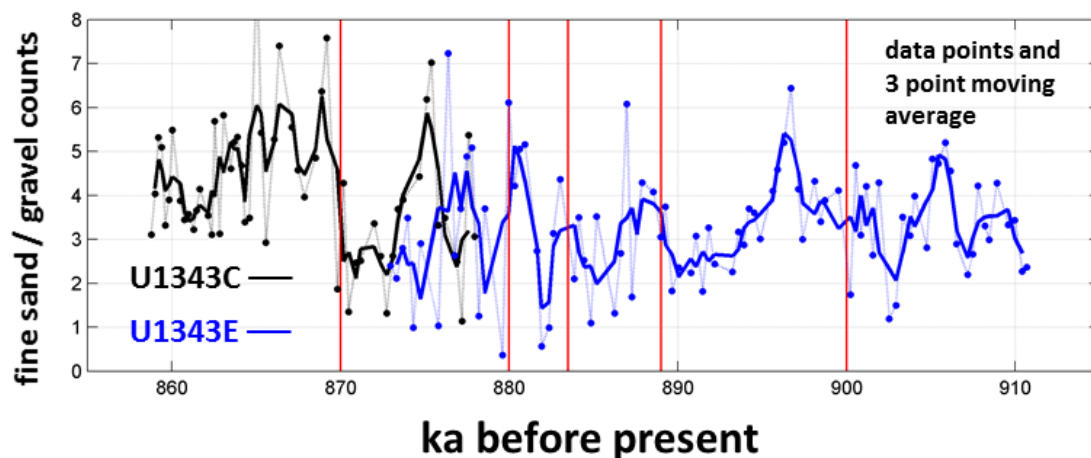
Figure 24. Tracking sea ice using the ratio: fine sand / gravel counts

PRESENCE OF ICEBERGS IN MIS 23 AND 22

According to the criteria explained earlier, iceberg presence is suggested when there is a presence of gravel (Figure 25). The shaded blue intervals in the figure are periods when iceberg presence is more likely. Accordingly, the presence of icebergs seems to be likely during interglacial MIS 23, at about 907 and 903 ka. Iceberg presence is relatively low through the early part of MIS 22. Then IRD abundance suggests four more pulses of icebergs starting in the middle of MIS 22 coming at about 885, 882, 879 and 877 ka, each pulse occurring at intervals of about 3 ka. Felsic lithic abundance in the coarse sands is also high at these times (Figure 17), with the highest in the record at 882

ka. This supports the interpretation that these IRD pulses are GIRD, from icebergs carrying continentally derived lithics. The low abundance of gravels after 874 ka is interpreted as low contribution of GIRD indicating low iceberg presence at the end of MIS 22 and into MIS 21.
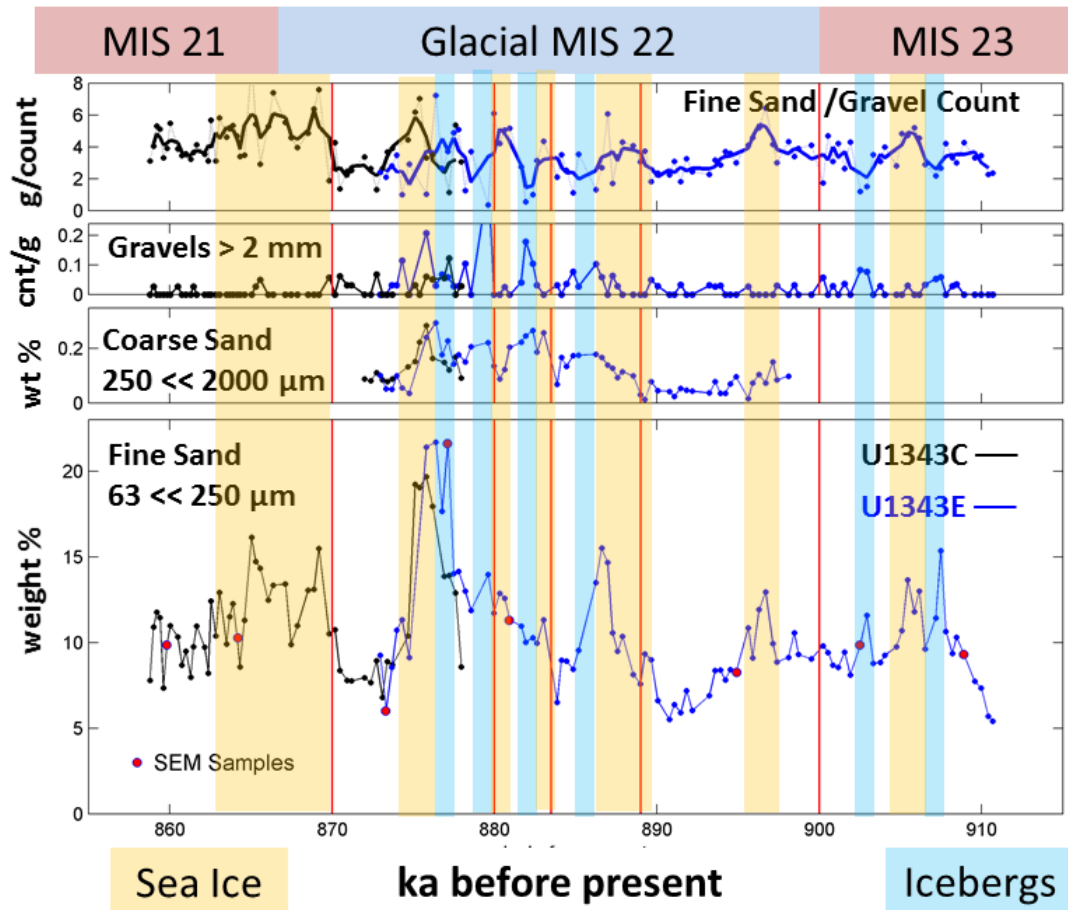
Figure 25. Tracking icebergs and sea ice at U1343

PRESENCE OF SEA ICE DURING MIS 23, 22, AND 21

As explained earlier, we suggest the presence of sea ice when the gravel abundance is low at the same time that the fine sand abundance is high (Figure 25). The shaded yellow intervals in the figure indicate the periods when sea ice presence is more likely. A period of greater sea ice occurs in MIS 23 at 906 ka, between the two iceberg pulses. Sea ice presence is indicated in early glacial MIS 22, at 897 ka, after which comes

a period of low sea ice or essentially sea ice free conditions. After 890 ka and before a pulse of icebergs, from 889 to ~887 ka there is a growing sea ice presence. Quartz and glauconite peak at this time (Figure 17), and the lithic abundance is relatively low, supporting the interpretation that this fine sand peak is a sea ice contribution to the sediment. Another evidence for the presence of sea ice is suggested by samples temporally located after the last iceberg pulse between 877 and 875 ka: during this period quartz is at its highest abundance in the coarse sands (Figure 17). The highest peak found in the fine sand is also present in the coarse sand at this time (Figure 25). Since the concurrent gravel counts peak is lower, the high abundance of both coarse and fine material suggests that the coarse sand, with a high abundance of quartz, was also entrained by sea ice. Two more periods potentially characterized by sea ice occur between 884 and 883 ka, and between 881 and 880 ka as suggested by an increase of the fine sand to gravel ratio, and in the abundance of fine sand. It is worth noting how the periods of higher possible presence of sea ice seem to alternate with the iceberg pulses. When sea ice is high, icebergs are low. However, this alternation may just be a bias related to the way the two are interpreted. The presence of sea ice just before 877 ka may be suggested between the last two iceberg pulses, but with the overlap of the time series data from both U1343C and U1343E holes, the pattern is not clear. After a period with some GIRD suggested from 875 to 870 ka, sea ice presence increases at 870 ka and remains high until at least 863 ka, into interglacial MIS 21.

IRD AND THE REGIONAL δ^{18}O U1343 RECORD DURING THE MPT

In this section the IRD evidence from Site U1343 is compared with the benthic foraminifera δ^{18}O record from Kender (unpublished) (Figures 9 and 26). Both data sets came from the same Site U1343 samples. Note the y-axis on the δ^{18}O curve; it increases downward. The blue and yellow shaded intervals indicating the more likely presence of icebergs and sea ice (based on the fine sand / gravel count ratio) are in the same positions as in Figure 25.

Evidence for icebergs and sea ice is present in the U1343 record during interglacial MIS 23. The pulses of gravels during interglacial MIS 23 interpreted as GIRD occur after the time in the isotope stage of warmest temperatures and least

continental ice volume, as indicated by the changes in the $\delta^{18}O$. This suggests calving of glacial ice even as the temperatures cool. It may be that continental ice accumulation rates are high even as the ice sheets experience ablation resulting in a slow net increase in continental ice volume near the end of the MIS 23 interglacial stage (Figure 26). The presence of sea ice is also suggested at this time and in the beginning of MIS 22. The movement of the $\delta^{18}O$ curve indicates that there is either cooling at the close of MIS 23 and/or slow growth of the continental ice volume. Possibly the sea ice cover reduces available moisture for the production of snow and/or the sea ice albedo effect contributes to decreasing temperatures.
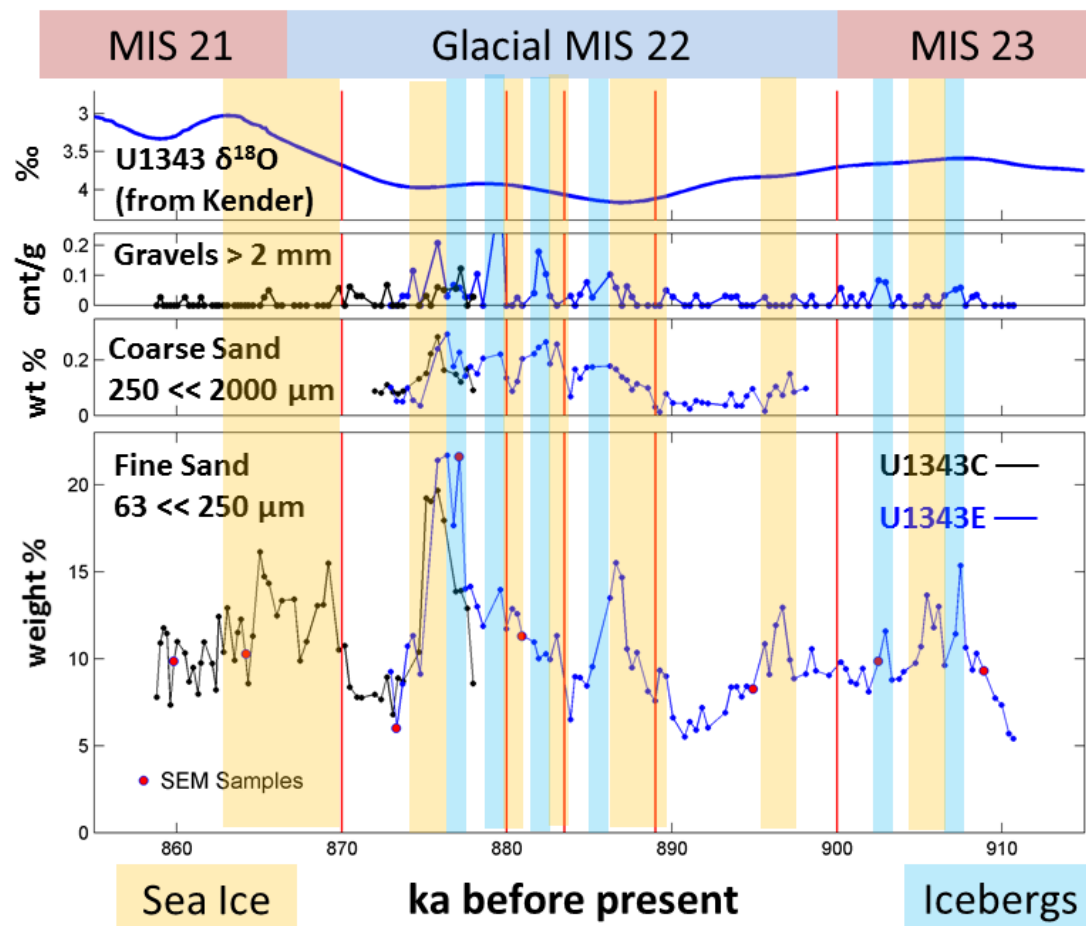
Figure 26. Icebergs and sea ice compared to the local benthic $\delta^{18}O$ record

After 897 ka, the beginning of MIS 22 is relatively iceberg and sea ice free until later in the stage when global ice volume approaches its maximum. The low abundance of both SIRD and GIRD during this time seems to be consistent with the build-up of continental ice: stable snow cover on land brings colder temperatures, and yet moisture is available from the open seas for formation of snow. Beginning shortly after 886 ka four pulses of GIRD in MIS 22 all occur when $\delta^{18}O$ is at a level indicating cold temperatures and high continental ice volume. The first of these GIRD pulses starts subsequent to the coolest period with the increased evidence of SIRD. The pulses continue through a slightly warmer period, and a fourth peak of GIRD occurs during the second coolest period, again with the increased presence of SIRD. Shortly thereafter, the deglaciation, indicated by the steep change in the $\delta^{18}O$ record, leads into MIS 21.

The timing of GIRD occurrence in relation to the transition from glacial to interglacial conditions as shown in the U1343 >63 μm siliciclastic and regional $\delta^{18}O$ records presents several similarities: 1) with meltwater events recorded in the Labrador Sea at the end of the last glacial maximum, in that one comes shortly before the deglaciation and a second comes at the deglaciation (Andrews et al. 1994); 2) with IRD events in the Pacific off Vancouver Island, in that the IRD events came in pulses near the end of the last glaciation, pulses that were interpreted as iceberg calving off the Cordilleran Ice Sheet before it retreated inland (Hendy and Cosma 2008). The similarity in the pattern of GIRD coming in pulses that culminate with the subsequent deglaciation strengthens our interpretation that the gravels from these pulses in our data set are GIRD.

There is low GIRD during MIS 21 (after 866 ka); however, SIRD is more prevalent in the record during interglacial MIS 21 than during interglacial MIS 23 (before 900 ka); and more frequent after 890 ka than before. Periods of increased SIRD (about 906, 896, 887, 876, and 866 ka) seem to occur about every 10 ka. In conjunction with these periods of higher SIRD, the regional $\delta^{18}O$ curve shows a deceleration: either slowing its increasing trend, starting to decrease, or continuing to decrease more rapidly. This is consistent with the presence of sea ice cover reducing evaporation that has the effect of either slowing the accumulation of continental ice volume or reducing its total volume from lack of additional snow. In MIS 21, the local $\delta^{18}O$ reaches the level of warmest temperatures and least continental ice volume at 863 ka, at the same time that

the IRD abundance drops. After 863 ka the decreased abundance of IRD which we have interpreted to be SIRD, together with the change in the $\delta^{18}O$ curve, suggest that the continental ice volume increases under the influence of increased open water.

IRD AND SEA LEVEL CHANGE DURING THE MPT

Elderfield et al. (2012) separated the LR04 benthic $\delta^{18}O$ stack into the deep water temperature component and the ice sheet volume component, from which they derived sea level equivalents in meters relative to the modern sea level through the MPT. Their results give absolute sea level, but do not take into account local changes such as would result from isostatic rebound (Lambeck and Chappell 2001), an effect that would be magnified in Arctic and sub-Arctic regions where ice sheets wax and wane. Their results will be used to approximate the changes in sea level by noting the age (ka) and sea level equivalent to the nearest 10 meters of the major maximums and minimums in sea level (See Table 7). The timing of the U1343 iceberg and sea ice more likely presence will be compared to these sea level shifts.

Table 7. Shifts in the Sea Level over MIS 23, 22, 21, from Elderfield et al. (2012)

Local Max or Min	Age (ka before present)	Sea Level (m relative to present)	Local Max or Min	Age (ka before present)	Sea Level (m relative to present)
Min	855.5	-10	Min	882.0	-100
Max	860.2	10	Max	884.8	-90
Min	865.7	-40	Min	888.3	-120
Max	868.0	-10	Max	893.8	-60
Min	873.9	-100	Min	910.1	-40
Max	876.6	-80			

Glacial MIS 22 is unusual because it follows an interglacial that began with a 'failed termination'(Barker et al. 2009; Elderfield et al. 2012) (See Figure 1). Interglacials before MIS 23 typically have sea level maximums that are well above the present level. During MIS 23 the maximum sea level was near -40 m. On the other hand during glacial MIS 24 the sea level did not drop much beyond -60 m and the lowest value for sea level during MIS 26 was near -40 m. The termination between MIS 24 and MIS 23 has been interpreted as a 'failed deglaciation' (Elderfield et al. 2012). Since the sea level equivalent is related to the ice volume on land, this means that during interglacial

MIS 23 the Alaskan Cordillera would have maintained a significant volume of continental ice that could produce icebergs. This observation is consistent with the evidence for GIRD found in the U1343 sediments in the latter half of interglacial MIS 23 as seen in Figure 27. The blue and yellow shaded intervals in Figure 27, representing the more likely presence of icebergs and sea ice, are in the same positions as in Figures 25 and 26.
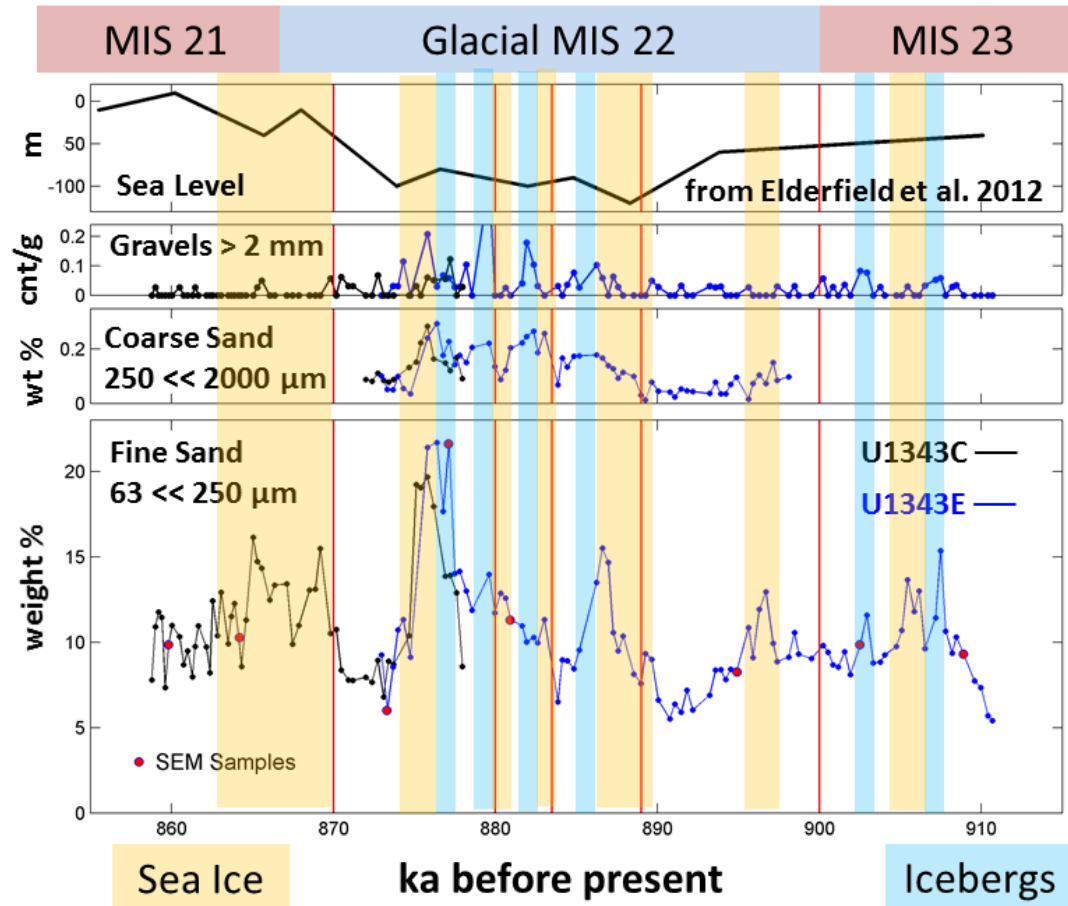
Figure 27. Icebergs and sea ice compared with sea level from Elderfield et al. (2012)

The presence of SIRD during MIS 23 and at the beginning of MIS 22 could have contributed to a slower rate of continental ice sheet buildup. This is consistent with the gradual lowering of sea level at this time (Figure 27): the cooling at the beginning of MIS 22 would have allowed ice sheets to grow, but the presence of sea ice decreased the moisture supply so the ice buildup proceeded more slowly. The subsequent period of low

SIRD and GIRD from 896 to 890 ka is likely indicating dominantly open water conditions. Evaporation from open water in a high latitude sea during a cold period would build up the continental snow and ice. In this period the sea level is decreasing faster, consistent with this interpretation. Sea ice again has an increased presence shortly after 890 ka, and before the minimum in sea level during MIS 22, in coincidence with an increase in the coarse sand fraction of the shelf derived (and sea ice rafted) quartz and glauconite components (Figure 17). Since glauconite is formed in quiet, warmer waters, deeper than 15 m (Rothwell 1989), it would be more likely to be entrained by sea ice when the sea is at lower levels.

During the latter half of MIS 22, pulses of glacial ice alternate with sea ice, as the sea level fluctuates during a low stand in the coldest part of the glacial. Before the final deglaciation and the rapid rise of sea level there is a period of increased sea ice. During the deglaciation, evidence for GIRD and SIRD is rare: seasonal sea ice is less likely to extend to the location of Site U1343 and the front of the continental ice sheets moves inland away from the coastline. Interestingly, the two intervals of low IRD during MIS 22 correspond to when the sea level is either rapidly decreasing or rapidly increasing.

As sea level reaches a maximum toward the end of the deglaciation sea ice is again present beginning at 870 ka, this time with low iceberg presence. This slows evaporation and the production of snow, resulting in the continued decrease of continental ice volume as sea level continues to rise, and ice sheets melt toward the end of MIS 22. As the presence of sea ice decreases (863 ka) and open water increases in MIS 21, sea level starts to decrease as once again as the continental ice volume builds up.

TESTING THE SEA ICE SWITCH HYPOTHESIS

Our data set from the Bering Sea lends support to the Sea Ice Switch (SIS) mechanism for the MPT that was discussed in the Introduction. IRD that our criteria suggest is SIRD is present in the coldest period of MIS 22 shortly before the first of four GIRD pulses; the SIRD continues intermittently, and is present in the second coldest period before the deglacial and termination of MIS 22. This, according to Gildor and Tziperman (2003), is what would be expected if the presence or absence of sea ice is

controlling the climate cycles. The increased presence of SIRD in interglacial MIS 21 when compared to interglacial MIS 23 is consistent with there being more sea ice after the activation of the SIS, when the gradual cooling of the deep ocean moves the stable steady state about which earth's climate fluctuates into temperatures in which the continental ice volume accumulation rates fall from the open ocean mode to the sea ice cover mode (see Figure 3). The asymmetrical shape (gradual growth, rapid decrease) of the fine sand record which seems to be coming primarily from sea ice, is similar to the saw-toothed shape of the other climate cycles during the later Pleistocene, including the $\delta^{18}O$ and sea level cycles (Lisiecki and Raymo 2005; Elderfield et al. 2012). Changes in the coarse sand composition, including the increasing quartz (Figure 18) and the decreasing felsic lithics (Figure 19), almost span the MIS 22 (900 to 866 ka). These changes are possibly the result of increased input from sea ice of quartz entrained from the shallow continental shelf, and decreased input from glacial ice of felsic lithics entrained in alpine regions. SIRD would be more prevalent after the SIS was activated, GIRD would be more prevalent before. It would be interesting to see how the petrographic composition changes over the course of many glacial/interglacial cycles: whether the petrographic composition also cycles, or if it shows a different trend. Extending this data set over several glacial/interglacial cycles may clarify the support for the SIS mechanism for the MPT.

REFINING THE METHOD OF TRACKING ICEBERGS AND SEA ICE

One of the difficulties of using the ratio of fine sand abundance to gravel count for an indication of the increased presence of sea ice is that the gravel counts are low. If there was a grain size smaller than 2 mm that would still most likely be GIRD, counts above that size that would be a more reliable indicator. Kender (unpublished data) counted terrigenous siliciclastics > 800 μm from this same data set, from ~895 to ~860 ka. For comparison, both count records, normalized by the dry bulk sample weight, are shown in Figure 28. Four pulses of IRD come between 888 and 874 ka in both the >800 μm and the >2 mm count records. These pulses are most likely from GIRD, and show up more clearly in the >800 counts. There is a difference in the two records from 870 to 866 ka. This period is relatively high in IRD of grain size 800<<2000 μm, yet the numbers of

gravels > 2 mm are low. Since glacial ice is less sorted than sea ice in the coarser particle sizes, and the distribution in this period shows more sorting in these sizes, these siliciclastics are more likely transported by sea ice. Perhaps counting very coarse sand-size siliciclastics >1000 μm (Wentworth scale), or even >1500 μm would work better than using counts >2 mm for the fine sand / gravel count ratio used to track the presence of glacial ice and sea ice. The source of the SIRD will affect the grain size, and sea ice is able to raft siliciclastics of large dimensions. As sediment is sea ice rafted from the shallow continental shelf floor, what is left behind will become coarser, and so the grain size that is rafted will vary in time, especially if it is not replaced by additional riverine terrigenous sediment. The fuzzy size division between GIRD and SIRD may vary from location to location, and even from time to time, so the best approach may be to sieve and count several different very coarse sand and gravel size fractions and check the results.

I recommend wet-sieving the bulk sample using 63 μm, 250 μm, and 2 mm mesh sieves to get the weight % of the 63<<250 μm fraction, the 250<<2000 μm fraction, and the >2 mm fraction. Then I would dry-sieve the 250<<2000 μm fraction at 1000 μm and 1500 μm to get a count of siliciclastics of those sizes. The siliciclastic counts of the appropriate size fraction verified after further investigation could then be added to the gravel counts >2 mm to get a count of the siliciclastics that are most likely GIRD. That count could then be divided into the fine sand to get a value that more clearly reflects the presence of SIRD.
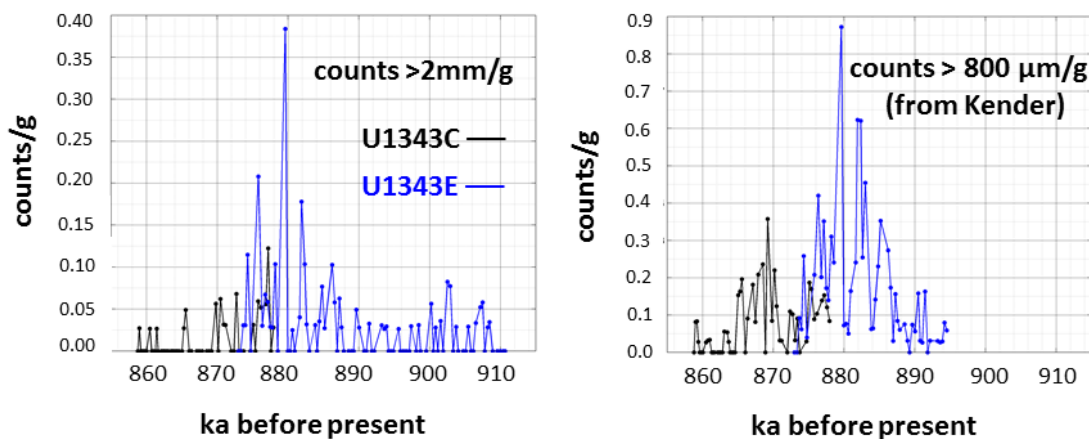
Figure 28. Comparing >2 mm counts with > 800 μm counts

CHAPTER 5

CONCLUSIONS

In order to understand the history of continental deglaciations and sea ice extent, patterns in iceberg and sea ice rafted debris need to be recognized. An important methodological result of this study has been the development of an approach to reconstruct the presence and absence of two different kinds of IRD. The method is based on the difference in the entrainment of fine sand ($63<<250$ μm), coarse sand ($250<<2000$ μm), and gravels (>2 mm) by glacial ice and sea ice. Icebergs are much more likely than sea ice to entrain gravels. Sea ice has the potential to entrain and transport volumes of fine sand. When gravels are present, the IRD suggests the presence of glacial ice. When fine sand abundance is high at the same time that gravel counts and coarse sand abundance are low, the IRD suggests the presence of sea ice. When gravels are present, coarse sand abundance is high, and fine sand abundance is high, the IRD suggests input from both sea ice and glacial ice. Petrographic composition is used to give support to this method of reconstructing the presence and/or absence of icebergs and sea ice. According to these newly established criteria, we have found evidence for icebergs and sea ice in Bering Sea sediments from interglacial MIS 23, glacial MIS 22, and interglacial MIS 21.

In order to understand the connections between continental and oceanic conditions, we need to look at the changes in the presence of both kinds of IRD. Using a high resolution IRD record and the previously established criteria to track icebergs and sea ice, the following are indicated:

- Icebergs are present in the Bering Sea during interglacial MIS 23 as well as glacial MIS 22. The end of MIS 22 and beginning of MIS 21 show little presence of icebergs.
- Icebergs come in four pulses between 885 and 877 ka, during the time in MIS 22 when temperatures are coldest and continental ice volume is greatest.
- Sea ice is present off the continental slope of the Bering Sea at times in MIS 23, MIS 22, and MIS 21. Periods of increased sea ice presence seem to come every 10 ka.

- Sea ice is present from 889 to 887 ka, at the time in MIS 22 when temperatures are coldest and continental ice volume is greatest; sea ice is also present from 877 to 875 ka, after the last iceberg pulse and at the beginning of the deglaciation.

- Sea ice is present from 870 to 863 ka at the end of the MIS 22 termination and into the beginning of interglacial MIS 21.

- Sea ice has a greater presence in interglacial MIS 21 than in MIS 23.

- Two periods of low icebergs and sea ice are indicated in MIS 22: from 896 to 890 ka at a time when sea level is falling (continental ice volume is building up), and from 875 to 870 ka at the time when sea level is rising during the deglaciation (continental ice is melting away from the shoreline during a warm period).

As summarized in the bullet points above, this data set does suggest that sea ice cover has an effect on ice sheet growth. The times of fastest growth of ice sheet volume (when the sea level is lowering) come when a decreased presence of sea ice is indicated. But does this IRD data set give support to the SIS mechanism (Gildor and Tziperman 2000) for the MPT?

The greater presence of sea ice in interglacial MIS 21 compared to interglacial MIS 23 may be an indication that the climate has entered the 'sea ice switch' that according to the SIS model would shift the period of climate cycles to 100 ka (Gildor and Tziperman 2001). This data set (starting in MIS 23, through glacial MIS 22, and extending into MIS 21) is not long enough to make this conclusion. However, it does lend support to the SIS mechanism for the MPT in the way the ice sheet volume changes in relation to the increases and decreases in the likely presence of sea ice cover. Changes in the petrographic composition of the coarse sand and in the weathering of quartz grains continue through glacial MIS 22. It would be interesting to see how the composition changes over the course of many glacial/interglacial cycles: whether the composition and weathering also cycles, or if they show a different trend. Extending this data set over several glacial/interglacial cycles may clarify the support for the SIS mechanism.

REFERENCES

Aiello IW, Ravelo AC. 2012. Evolution of marine sedimentation in the Bering Sea since the Pliocene. Geosphere 8:1231–1253.

Alley RB, Cuffey KM, Evenson EB, Strasser JC, Lawson DE, Larson GJ. 1997. How glaciers entrain and transport basal sediment: physical constraints. Quat. Sci. Rev. 16:1017–1038.

Andreola F, Castellini E, Manfredini T, Romagnoli M. 2004. The role of sodium hexametaphosphate in the dissolution process of kaolinite and kaolin. J. Eur. Ceram. Soc. 24:2113–2124.

Andrews JT, Erlenkeuser H, Tedesco K, Aksu AE, Jull AJT. 1994. Late Quaternary (Stage 2 and 3) meltwater and Heinrich events, Northwest Labrador Sea. Quat. Res. 41:26–34.

Barker S, Diz P, Vautravers MJ, Pike J, Knorr G, Hall IR, Broecker WS. 2009. Interhemispheric Atlantic seesaw response during the last deglaciation. Nature 457:1097–102.

Bindeman IN, Ponomareva V V, Bailey JC, Valley JW. 2004. Volcanic arc of Kamchatka: a province with high-δ18O magma sources and large-scale 18O/16O depletion of the upper crust. Geochim. Cosmochim. Acta 68:841–865.

Bischof JF, Darby DA. 1997. Mid- to Late Pleistocene ice drift in the Western Arctic Ocean: evidence for a different circulation in the past. Science 277:74–78.

Boggs S. 2012. Principles of Sedimentology and Stratigraphy. 5th ed. Upper Saddle River: Pearson Prentice Hall.

Brennan CE, Meissner KJ, Eby M, Hillaire-Marcel C, Weaver AJ. 2013. Impact of sea ice variability on the oxygen isotope content of seawater under glacial and interglacial conditions. Paleoceanography 28:388–400.

Briner J, Kaufman D. 2008. Late Pleistocene mountain glaciation in Alaska: key chronologies. J. Quat. Sci. 23:659–670.

Clark DL, Whitman RR, Morgan KA, Mackey SD. 1980. Stratigraphy and glacialmarine sediments of the Amerasian Basin, central Arctic Ocean. In: Geological Society of America Special Papers. p. 57.

Clark PU, Archer D, Pollard D, Blum JD, Rial JA, Brovkin V, Mix AC, Pisias NG, Roy M. 2006. The middle Pleistocene transition: characteristics, mechanisms, and implications for long-term changes in atmospheric pCO2. Quat. Sci. Rev. 25:3150–3184.

Clark PU, Pollard D. 1998. Origin of the Middle Pleistocene Transition by ice sheet erosion of regolith. Paleoceanography 13:1–9.

Dapples EC. 1967. Diagenesis of sandstones. In: Larsen G, Chilingar C V, editors. Diagenesis in sediments. Amsterdam: Elsevier. p. 91–125.

Dethleff D, Kuhlmann G. 2009. Entrainment of fine-grained surface deposits into new ice in the southwestern Kara Sea, Siberian Arctic. Cont. Shelf Res. 29:691–701.

Dethloff K, Rinke A, Benkel A, Køltzow M, Sokolova E, Kumar Saha S, Handorf D, Dorn W,

Rockel B, von Storch H, et al. 2006. A dynamical link between the Arctic and the global climate system. Geophys. Res. Lett. 33:L03703.

Dickinson WR, Beard LSUE, Brakenridge GR, Erjavec JL, Ferguson C, Inman KF, Knepp REXA, Lindberg FA, Ryberg PT. 1983. Provenance of North American Phanerozoic sandstones in relation to tectonic setting. Geol. Soc. Am. Bull. 7606.

Dunhill G. 1998. Comparison of sea-ice and glacial-ice rafted debris: Grain size, surface features, and grain shape. USGS.

Elderfield H, Ferretti P, Greaves M, Crowhurst SJ, McCave IN, Hodell DA, Piotrowski AM. 2012. Evolution of ocean temperature. Science 337:704–709.

Eldrett JS, Harding IC, Wilson PA, Butler E, Roberts AP. 2007. Continental ice in Greenland during the Eocene and Oligocene. Nature 446:176–179.

Expedition 323 Scientists. 2011a. Expedition 323 summary. In: Takahashi K, Ravelo AC, Alvarez Zariklan CA, editors. Proceedings of the Integrated Ocean Drilling Program, Vol. 323: Toyko. Vol. 323. Integrated Ocean Drilling Program Management International Inc. p. 53.

Expedition 323 Scientists. 2011b. Site U1343. In: Takahashi K, Ravelo AC, Alvarez Zarikian CA, editors. Proceedings of the Integrated Ocean Drilling Program, Vol. 323: Toyko. Vol. 323. Integrated Ocean Drilling Program Management International Inc. (Proceedings of the IODP). p. 111.

Gildor H, Tziperman E. 2000. Sea ice as the glacial cycles' climate switch: role of seasonal and orbital forcing. Paleoceanography 15:605–615.

Gildor H, Tziperman E. 2001. A sea ice climate switch mechanism for the 100-kyr glacial cycles. J. Geophys. Res. 106:9117–9133.

Gildor H, Tziperman E. 2003. Sea-ice switches and abrupt climate change. Philos. Trans. A. Math. Phys. Eng. Sci. 361:1935–1942; discussion 1942–1944.

Gorbarenko SA, Wang P, Wang R, Cheng X. 2010. Orbital and suborbital environmental changes in the southern Bering Sea during the last 50kyr. Palaeogeogr. Palaeoclimatol. Palaeoecol. 286:97–106.

Heinrich H. 1988. Origin and consequences of cyclic ice rafting in the Northeast Atlantic Ocean during the past 130,000 years. Quat. Res. 29:142–152.

Hendy IL, Cosma T. 2008. Vulnerability of the Cordilleran Ice Sheet to iceberg calving during late Quaternary rapid climate change events. Paleoceanography 23:PA2101.

Herman F, Beyssac O, Brughelli M, Lane SN, Leprince S, Adatte T, Lin JYY, Avouac J-P, Cox SC. 2015. Erosion by an alpine glacier. Science 350:193–195.

Hermann AJ, Stabeno PJ, Haidvogel DB, Musgrave DL. 2002. A regional tidal/subtidal circulation model of the southeastern Bering Sea: Development, sensitivity analyses and hindcasting. Deep. Res. Part II Top. Stud. Oceanogr. 49:5945–5967.

Holland MM, Bitz CM. 2003. Polar amplification of climate change in coupled models. Clim. Dyn. 21:221–232.

von Huene R, Larson E, Crouch J. 1971. Preliminary study of ice-rafted erratics as indicators of glacial advances in the Gulf of Alaska. Proc. Deep Sea Drill. Program, Vol. 18:835–842.

Ingersoll R V., Bullard TF, Ford RL, Grimm JP, Pickle JD, Sares SW. 1984. The Effect of Grain Size on Detrital Modes: A Test of the Gazzi-Dickinson Point-Counting Method. J. Sediment. Res. Vol. 54:103–116.

IPCC. 2013. Summary for Policymakers. In: Stocker TF, Qin D, Plattner GK, Tignor M, Allen SK, Boschung J, Nauels A, Xia Y, Box V, Midgley PM, editors. Climate Change 2013: The Physical Science Basis. Contribution of Working Group I to the Fifth Assessment Report of the Intergovernmental Panel on Climate Change. Cambridge: Cambridge University Press. p. 33.

St. John K. 2008. Cenozoic ice-rafting history of the central Arctic Ocean: Terrigenous sands on the Lomonosov Ridge. Paleoceanography 23:PA1S05.

St. John KEK. 1999. Data report: Site 918 IRD mass accumulation rate record, late miocene-Pleistocene. In: Larsen HC, Duncan RA, Allan JF, Brooks E, editors. Proceedings of the Ocean Drilling Program, Scientific Results. Vol. 163. p. 163–166.

St. John KEK, Krissek LA. 1999. Regional patterns of Pleistocene ice-rafted debris flux in the North Pacific. Paleoceanography 14:653–662.

St. John KEK, Krissek LA. 2002. The late Miocene to Pleistocene ice-rafting history of southeast Greenland. Boreas 31:28–35.

Katsuki K, Takahashi K. 2005. Diatoms as paleoenvironmental proxies for seasonal productivity, sea-ice and surface circulation in the Bering Sea during the late Quaternary. Deep. Res. Part II Top. Stud. Oceanogr. 52:2110–2130.

Kaufman DS, Manley WF. 2004. Pleistocene Maximum and Late Wisconsin glacier extents across Alaska, USA. In: Ehlers J, Gibbard P, editors. Quaternary Glaciations: Extent and Chronology. Part II: North America. Amsterdam: Elsevier. p. 9–27.

Kempema EW, Reimnitz E, Barnes PW. 1989. Sea ice sediment entrainment and rafting in the Arctic. J. Sediment. Res. Vol. 59:308–317.

Kender S. (unpublished work, University of Nottingham).

Kennett J. 1982. Marine Geology. Englewood Cliffs, NJ: Prentice-Hall, Inc.

Lambeck K, Chappell J. 2001. Sea level change through the last glacial cycle. Science 292:679–86.

Lisiecki LE, Raymo ME. 2005. A Pliocene-Pleistocene stack of 57 globally distributed benthic δ18O records. Paleoceanography 20.

Lisitzin AP. 2002. Sea-ice and iceberg sedimentation in the ocean, recent and past. Berlin: Springer-Verlag.

Lisitzin AP. 2010. Marine ice-rafting as a new type of sedimentogenesis in the Arctic and novel approaches to studying sedimentary processes. Russ. Geol. Geophys. 51:12–47.

McKelvey B, Chen W, Arculus R. 1995. Provenance of Pliocene-Pleistocene ice-rafted debris,

Leg 145, Northern Pacific Ocean. In: Rea DK, Basov LA, Scholl DW, Allan JF, editors. Proceedings of the Ocean Drilling Program, Scientific Results. Vol. 145.

Molén MO. 2014. A simple method to classify diamicts by scanning electron microscope microtextures. Sedimentology 61:2020–2041.

Niebauer HJ. 1998. Variability in Bering Sea ice cover as affected by a regime shift in the North Pacific in the period 1947-1996. J. Geophys. Res. 103.

NSIDC (National Snow and Ice Data Center) Scientists. 2012. February ice extent low in the Barents Sea, high in the Bering Sea. Arct. Sea Ice News Anal.

NSIDC (National Snow and Ice Data Center) Scientists. 2015. Antarctic sea ice at its 2015 maximum. Arct. Sea Ice News Anal.

Nürnberg D, Wollenburg I, Dethleff D, Eicken H, Kassens H, Letzig T, Reimnitz E, Thiede J. 1994. Sediments in Arctic sea ice: Implications for entrainment, transport and release. Mar. Geol. 119:185–214.

O'Neil JR. 1968. Hydrogen and oxygen fractionation between ice and water. J. Phys. Chem. 72:3683–3684.

Overland JE, Pease CH. 1982. Cyclone climatology of the Bering Sea and its relation to sea ice extent. Mon. Weather Rev. 110:5–13.

Overland JE, Roach AT. 1987. Northward flow in the Bering and Chukchi Seas. J. Geophys. Res. 92:7097–7105.

Pease CH. 1980. Eastern Bering Sea ice processes. Mon. Weather Rev. 108:2015–2023.

Polyak L, Alley RB, Andrews JT, Brigham-Grette J, Cronin TM, Darby DA, Dyke AS, Fitzpatrick JJ, Funder S, Holland M, et al. 2010. History of sea ice in the Arctic. Quat. Sci. Rev. 29:1757–1778.

Powers MC. 1953. A new roundness scale for sedimentary particles. J. Sediment. Petrol. 23:117–119.

Ravelo AC, Andreasen DH, Lyle M, Olivarez Lyle A, Wara MW. 2004. Regional climate shifts caused by gradual global cooling in the Pliocene epoch. Nature 429:263–7.

Raymo ME, Huybers P. 2008. Unlocking the mysteries of the ice ages. Nature 451:284–285.

Raymo ME, Ruddiman WF, Froelich PN. 1988. Influence of late Cenozoic mountain building on ocean geochemical cycles. Geology 16:649–653.

Reimnitz E, Kempema E, Barnes PW. 1987. Anchor ice, seabed freezing, and sediment dynamics in shallow Arctic seas. J. Geophys. Reseach 92:671–678.

Reimnitz E, McCormick M, Bischof J, Darby DA. 1998. Comparing sea-ice sediment load with Beaufort Sea shelf deposits: is entrainment selective? J. Sediment. Res. 68:777–787.

Rothwell RG. 1989. Minerals & metalloids in marine sediments: an optical identification guide. London: Elsevier Ltd.

Sharma GD. 2012. The Alaskan shelf: hydrographic, sedimentary, and geochemical

environment. Spinger Science & Business Media.

Snoeckx H, Grousset F, Revel M, Boelaert A. 1999. European contribution of ice-rafted sand to Heinrich layers H3 and H4. Mar. Geol. 158:197–208.

Stabeno PJ. 2016. (email communication).

Stabeno PJ, Schumacher JD, Ohtani K. 1999. The physical oceanography of the Bering Sea. In: Loughlin TR, Ohtani K, editors. Dynamics of the Bering Sea: A Summary of Physical, Chemical, and Biological Characteristics, and a Synopsis of Research on the Bering Sea. Fairbanks: University of Alaska Sea Grant. p. 1–28.

Taber S. 1943. Perennially frozen ground in Alaska: its origin and history. Bull. Geol. Soc. Am. 54:1433–1548.

Takahashi K. 2005. The Bering Sea and paleoceanography. Deep Sea Res. Part II Top. Stud. Oceanogr. 52:2080–2091.

Takahashi K, Ravelo AC, Alvarez Zarikian C. 2011. IODP Expedition 323–Pliocene and Pleistocene Paleoceanographic Changes in the Bering Sea. Sci. Drill.:4–13.

Tanaka S, Takahashi K. 2005. Late Quaternary paleoceanographic changes in the Bering Sea and the western subarctic Pacific based on radiolarian assemblages. Deep. Res. Part II Top. Stud. Oceanogr. 52:2131–2149.

Tantillo B, St. John K, Passchier S, Kearns L. 2012. Can sea ice-rafted debris be distinguised from iceberg-rafted debris based on grain surface features? In: Geological Society of America Southeastern Section 61st annual meeting.

Tziperman E, Gildor H. 2003. On the mid-Pleistocene transition to 100-kyr glacial cycles and the asymmetry between glaciation and deglaciation times. Paleoceanography 18:1–8.

VanLaningham S, Pisias NG, Duncan RA, Clift PD. 2009. Glacial–interglacial sediment transport to the Meiji Drift, northwest Pacific Ocean: Evidence for timing of Beringian outwashing. Earth Planet. Sci. Lett. 277:64–72.

Walsh JE, Johnson CM. 1979. An Analysis of Arctic Sea Ice Fluctuations, 1953–77. J. Phys. Oceanogr. 9:580–591.

Wang MY, Overland JE. 2009. A sea ice free summer Arctic within 30 years? Geophys. Res. Lett. 36:L07502.

Zamoruyev V. 2004. Quaternary glaciations of north-eastern Asia. In: Quaternary Glaciations: Extent and Chronology/ Part III: South America, Africa, Asia, Australasia, Antarctica; p. 321–324.

APPENDIX A

**MORE EXAMPLES OF COMPOSITION OF
63<<250 μm, 250<<2000 μm, and >2 mm
FRACTIONS**
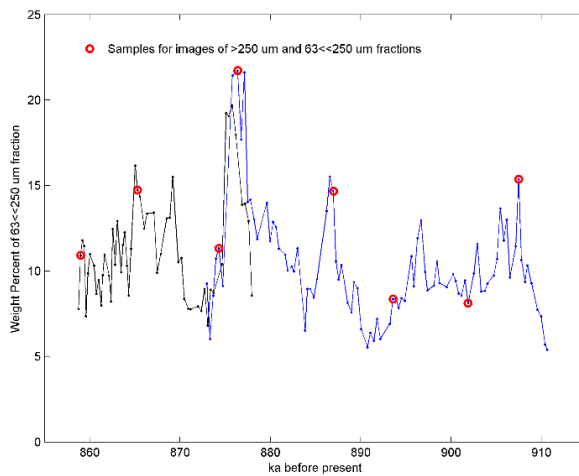
Sample source for examples of samples indicated on the graph to the left.

The examples of the fine and coarse fractions are from the same sample.

The examples on the left are of coarse sand >250 um. They also include all components including gravels.

The examples on the right are of fine sand 63>>250 um. Samples photographed on a 5 mm grid.
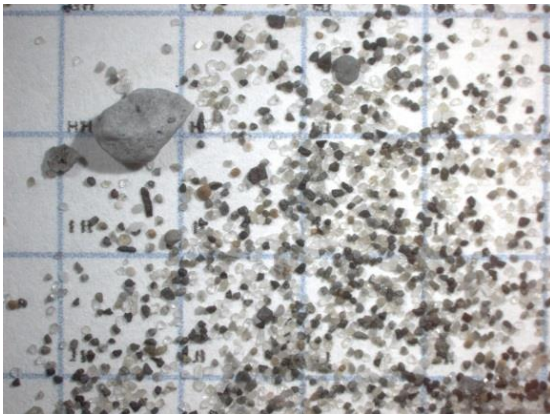
U1343C-23H-3 W 16.0—18.0 cm, MIS 21, 859.0 ka, 11% fine sand. (no image of fine sand).
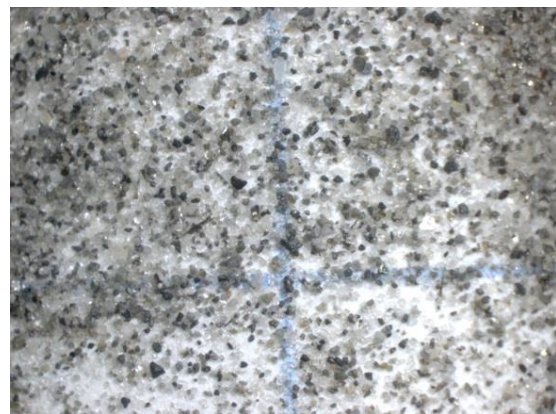
U1343C-23H-4 W 77.0--79.0 cm, MIS 21, 865.3 ka, 15% fine sand, "high sea ice".
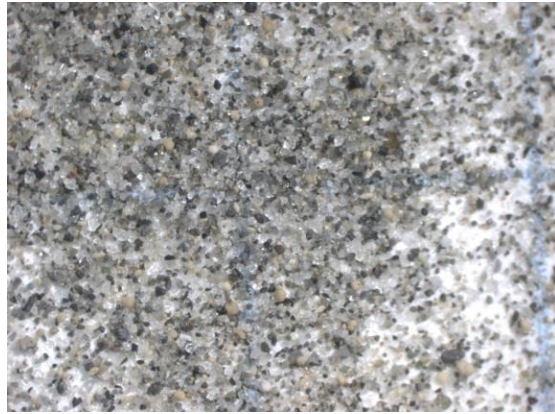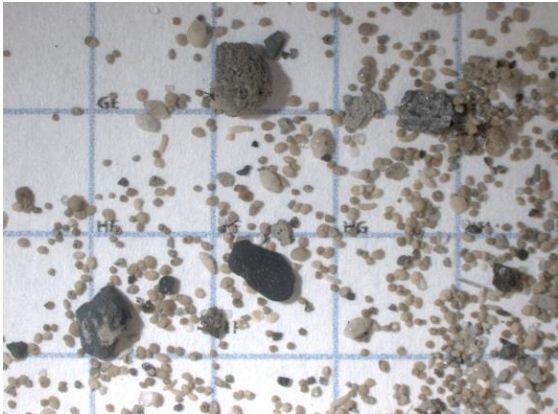
U1343E-25H-2 W 30.0--32.0 cm, MIS 22, 874.3 ka, 11% fine sand, "high foraminifera count".
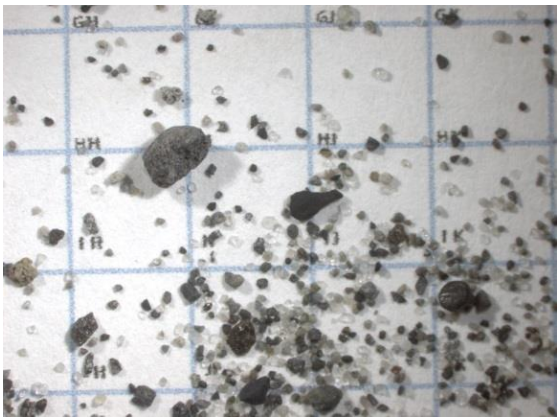
U1343E-25H-2 W 77.0--79.0 cm, MIS 22, 876.4 ka, 22% fine sand, "top of the highest fine sand peak".
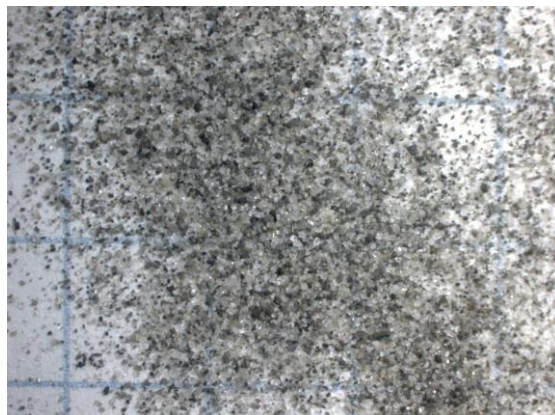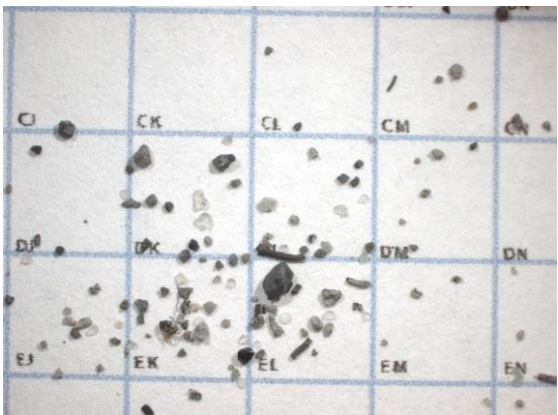
U1343E-25H-4 W 16.0--18.0 cm, MIS 22, 887.0 ka, 15% fine sand, "top of a high fine sand peak".
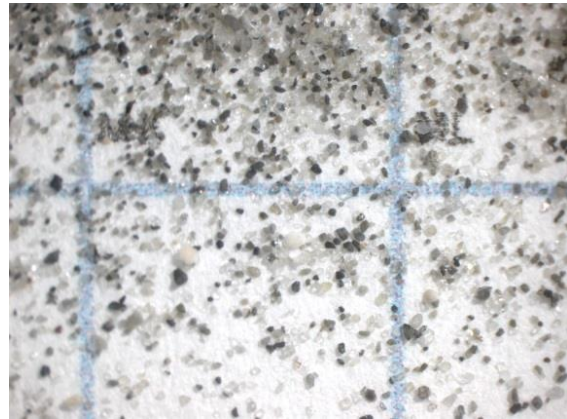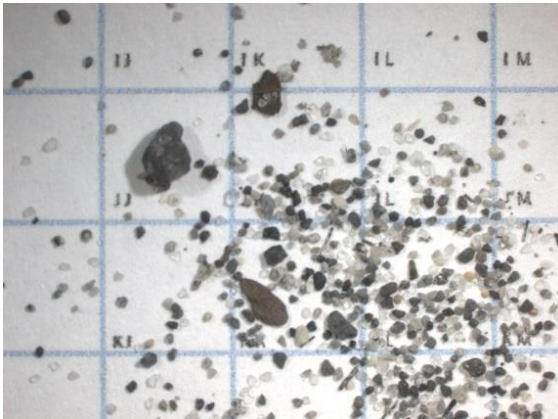
U1343E-25H-5 W 16.0--18.0 cm, MIS 22, 893.6 ka, 8% fine sand, "at the beginning of the faster drop in sea level".
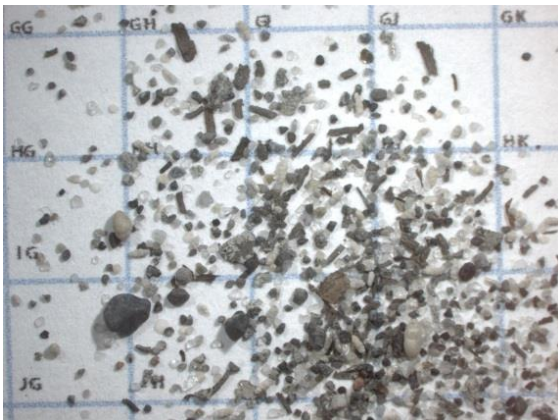
U1343E-25H-6 W 54.0--56.0 cm, MIS 23, 901.9 ka, 8% fine sand, "during slow drop in sea level".
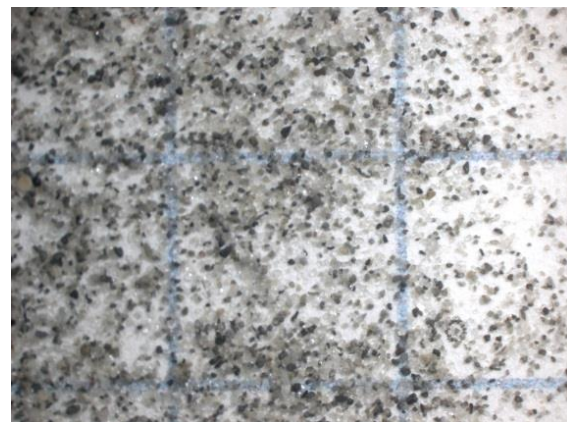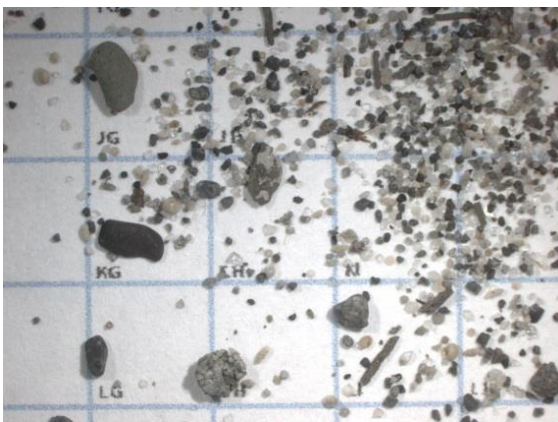
U1343E-25H-7 W 30.0--32.0 cm, MIS 23, 907.5 ka, 15% fine sand, "near high sea level".

APPENDIX B

DATA FOR CALCULATING THE ABUNDANCES
OF GRAVEL, COARSE SAND, AND FINE SAND

MPA Ref. #	IODP Expedition 323 Site U1343 Sample Source	Depth (m ccsf)	Age Model Sev Kender	Bulk Sample Weight	Weight 63<<250 um	Percent Biogenics	Weight 250<<2000 um	Count #>2mm	Clear Stuff
60121	U1343C-23H-3 W, 8.0--10.0 cm	224.10	858.77996	31.91	2.48427		0.05704	0	0
60122	U1343C-23H-3 W, 16.0--18.0 cm	224.18	859.00853	37.01	4.03867	0	0.11432	1	0
60123	U1343C-23H-3 W, 23.0--25.0 cm	224.25	859.20853	36.14	4.25615		0.15430	0	0
60124	U1343C-23H-3 W, 30.0--32.0 cm	224.32	859.40853	35.58	4.07940		0.14394	0	0
60125	U1343C-23H-3 W, 37.0--39.0 cm	224.39	859.60853	36.04	2.65008		0.04499	0	0
60126	U1343C-23H-3 W, 45.0--47.0 cm	224.47	859.83710	31.63	3.11605	0	0.08499	0	0
60127	U1343C-23H-3 W, 52.0--54.0 cm	224.54	860.03710	39.99	4.39081		0.10378	0	0
60129	U1343C-23H-3 W, 68.0--70.0 cm	224.70	860.49425	37.54	3.87483		0.08946	1	0
60130	U1343C-23H-3 W, 77.0--79.0 cm	224.79	860.75139	31.81	2.75846		0.06087	0	0
60131	U1343C-23H-3 W, 86.0--88.0 cm	224.88	861.00853	30.08	2.85295	1	0.04336	0	0
60132	U1343C-23H-3 W, 96.0--98.0 cm	224.98	861.29425	32.26	2.57618		0.05129	0	0
60133	U1343C-23H-3 W, 102.0--104.0 cm	225.04	861.46567	37.47	3.65461		0.06907	1	0
60134	U1343C-23H-3 W, 109.0--111.0 cm	225.11	861.66567	30.22	3.31171		0.05409	0	0
60136	U1343C-23H-3 W, 126.0--128.0 cm	225.28	862.15139	29.04	2.82932	0.5	0.05983	0	0
60137	U1343C-23H-3 W, 134.0--136.0 cm	225.36	862.37996	30.21	2.48357		0.03778	0	0
60138	U1343C-23H-3 W, 140.0--142.0 cm	225.42	862.55139	36.55	4.54698		0.06263	0	0
60139	U1343C-23H-4 W, 0.0--2.0 cm	225.52	862.83710	24.09	2.49990		0.04193	0	0
60140	U1343C-23H-4 W, 8.0--10.0 cm	225.60	863.06567	36.06	4.66367	0.5	0.07479	0	0
60142	U1343C-23H-4 W, 23.0--25.0 cm	225.75	863.49425	37.14	3.68591		0.05783	0	0

60143	U1343C-23H-4 W, 30.0--32.0 cm	225.82	863.69425	36.18	4.16852		0.05273	0	0
60144	U1343C-23H-4 W, 37.0--39.0 cm	225.89	863.89425	34.78	4.26409		0.06309	0	0
60145	U1343C-23H-4 W, 46.0--48.0 cm	225.98	864.15139	36.41	3.74797	0	0.09339	0	0
60146	U1343C-23H-4 W, 52.0--54.0 cm	226.04	864.32282	31.65	2.71208		0.07176	0	0
60147	U1343C-23H-4 W, 62.0--64.0 cm	226.14	864.60853	24.72	2.79344		0.05736	0	0
60149	U1343C-23H-4 W, 77.0--79.0 cm	226.29	865.03710	45.75	7.39284		0.24323	0	0
60150	U1343C-23H-4 W, 86.0--88.0 cm	226.38	865.29425	36.83	5.42379	0.5	0.10168	1	0
60151	U1343C-23H-4 W, 96.0--98.0 cm	226.48	865.57996	40.79	5.85269		0.10683	2	0
60152	U1343C-23H-4 W, 102.0--104.0 cm	226.54	866.05746	33.78	4.21845		0.09748	0	0
60153	U1343C-23H-4 W, 109.0--111.0 cm	226.61	866.36719	44.35	5.92324		0.07270	0	0
60155	U1343C-23H-4 W, 126.0--128.0 cm	226.78	867.11941	33.07	4.43710	0.5	0.08200	0	0
60156	U1343C-23H-4 W, 134.0--136.0 cm	226.86	867.47339	37.01	3.66309		0.05246	0	0
60157	U1343C-23H-4 W, 143.0--145.0 cm	226.95	867.87162	28.82	3.17016		0.02812	0	0
60158	U1343C-23H-5 W, 8.0--10.0 cm	227.10	868.53534	29.71	3.88351		0.07825	0	0
60159	U1343C-23H-5 W, 16.0--18.0 cm	227.18	868.88932	38.86	5.09507	0.5	0.06130	0	0
60160	U1343C-23H-5 W, 23.0--25.0 cm	227.25	869.19905	39.17	6.06924		0.12284	0	0
60162	U1343C-23H-5 W, 37.0--39.0 cm	227.39	869.81852	35.58	3.73805		0.06834	2	1
60163	U1343C-23H-5 W, 45.0--47.0 cm	227.47	870.17250	31.82	3.42526		0.08979	0	0
60164	U1343C-23H-5 W, 52.0--54.0 cm	227.54	870.48224	32.28	2.70494	1	0.04456	2	0
60165	U1343C-23H-5 W, 62.0--64.0 cm	227.64	870.92472	31.72	2.47119		0.03368	1	0
60166	U1343C-23H-5 W, 68.0--70.0 cm	227.70	871.19020	32.36	2.51381		0.04321	1	0
60168	U1343C-23H-5 W, 86.0--88.0 cm	227.88	871.98666	33.90	2.69108		0.03377	0	0

60169	U1343C-23H-6 W, 0.0--2.0 cm	227.97	872.38489	27.41	2.09889	0.5	0.03331	0	0
60170	U1343C-23H-6 W, 8.0--10.0 cm	228.05	872.73888	29.45	2.63786		0.04833	2	1
60171	U1343C-23H-6 W, 16.0--18.0 cm	228.13	873.09286	30.79	2.09646		0.03388	0	0
60172	U1343C-23H-6 W, 23.0--25.0 cm	228.20	873.40259	33.10	2.94755		0.03584	0	0
60173	U1343C-23H-6 W, 30.0--32.0 cm	228.27	873.71233	35.81	3.11654	0	0.05596	0	0
60175	U1343C-23H-6 W, 52.0--54.0 cm	228.49	874.68578	34.06	3.54108	2	0.11627	0	0
60176	U1343C-23H-6 W, 62.0--64.0 cm	228.59	875.12826	32.14	6.18159		0.11885	1	0
60177	U1343C-23H-6 W, 68.0--70.0 cm	228.65	875.39374	29.46	5.61557		0.07957	0	0
60178	U1343C-23H-6 W, 77.0--79.0 cm	228.74	875.79197	33.74	6.64470	0	0.10824	2	0
60179	U1343C-23H-6 W, 86.0--88.0 cm	228.83	876.19020	38.80	6.97208		0.10209	2	0
60181	U1343C-23H-6 W, 102.0--104.0 cm	228.99	876.89817	35.91	4.98548		0.06414	2	0
60182	U1343C-23H-6 W, 109.0--111.0 cm	229.06	877.20790	32.71	4.55781		0.11600	4	0
60183	U1343C-23H-6 W, 118.0--120.0 cm	229.15	877.60613	33.26	4.29277	0	0.09008	0	0
60184	U1343C-23H-6 W, 126.0--128.0 cm	229.23	877.96012	35.75	3.06389	2	0.05190	1	0
60185	U1343E-25H-2 W, 0.0--2.0 cm	228.10	872.97713	20.74	1.91947		0.03130	0	1
60186	U1343E-25H-2 W, 8.0--10.0 cm	228.18	873.33111	27.98	1.68504		0.02012	0	0
60187	U1343E-25H-2 W, 16.0--18.0 cm	228.26	873.68509	32.67	2.79673	0.5	0.03418	1	0
60188	U1343E-25H-2 W, 23.0--25.0 cm	228.33	873.99483	32.46	3.48466		0.12497	1	0
60189	U1343E-25H-2 W, 30.0--32.0 cm	228.40	874.30456	34.87	3.95154	3	0.18394	4	0
60190	U1343E-25H-2 W, 40.0--42.0 cm	228.50	874.74704	25.44	2.32335	7	0.24493	0	0
60191	U1343E-25H-2 W, 64.0--66.0 cm	228.74	875.80899	19.25	4.12420	0.5	0.05239	4	0
60192	U1343E-25H-2 W, 77.0--79.0 cm	228.87	876.38421	33.32	7.23550		0.11902	1	0

60193	U1343E-25H-2 W, 86.0--88.0 cm	228.96	876.78244	29.78	5.26497		0.07372	2	0
60194	U1343E-25H-2 W, 94.0--96.0 cm	229.04	877.13642	34.17	7.38629		0.12200	2	0
60195	U1343E-25H-2 W, 102.0--104.0 cm	229.12	877.49040	34.82	4.88513	0	0.07780	1	0
60196	U1343E-25H-2 W, 109.0--111.0 cm	229.19	877.80014	35.90	5.08599		0.08567	1	0
60197	U1343E-25H-2 W, 118.0--120.0 cm	229.28	878.19837	29.02	3.77392		0.05896	3	0
60198	U1343E-25H-2 W, 126.0--128.0 cm	229.36	878.55235	24.93	2.95953	3	0.07535	0	0
60200	U1343E-25H-3 W, 0.0--2.0 cm	229.60	879.61430	28.67	4.00907	0.5	0.08339	11	0
60201	U1343E-25H-3 W, 8.0--10.0 cm	229.68	879.96828	41.65	4.88663		0.08558	0	0
60202	U1343E-25H-3 W, 16.0--18.0 cm	229.76	880.32226	26.21	3.37630		0.04840	0	0
60203	U1343E-25H-3 W, 23.0--25.0 cm	229.83	880.63200	40.16	5.05127		0.09303	1	0
60204	U1343E-25H-3 W, 30.0--32.0 cm	229.90	880.94173	36.50	4.12992	0	0.10274	0	0
60206	U1343E-25H-3 W, 46.0--48.0 cm	230.06	881.64969	24.90	2.73259		0.08298	1	0
60207	U1343E-25H-3 W, 52.0--54.0 cm	230.12	881.91518	22.48	2.25294		0.10165	4	0
60208	U1343E-25H-3 W, 62.0--64.0 cm	230.22	882.35766	19.34	1.98707		0.06298	2	0
60209	U1343E-25H-3 W, 68.0--70.0 cm	230.28	882.62315	31.46	3.13753	0	0.07145	1	3
60210	U1343E-25H-3 W, 77.0--79.0 cm	230.37	883.02138	30.80	3.49039		0.09782	0	0
60212	U1343E-25H-3 W, 96.0--98.0 cm	230.56	883.86208	32.23	2.10193		0.02548	1	0
60213	U1343E-25H-3 W, 102.0--104.0 cm	230.62	884.12757	31.20	2.79606		0.06039	0	0
60214	U1343E-25H-3 W, 109.0--111.0 cm	230.69	884.43731	28.25	2.52330	0	0.05433	1	0
60215	U1343E-25H-3 W, 118.0--120.0 cm	230.78	884.83554	39.07	3.29787		0.09503	3	0
60216	U1343E-25H-3 W, 126.0--128.0 cm	230.86	885.18952	36.91	3.52149		0.08579	1	0
60218	U1343E-25H-4 W, 0.0--2.0 cm	231.10	886.25146	29.24	3.94954		0.06012	3	0

60219	U1343E-25H-4 W, 8.0--10.0 cm	231.18	886.60545	34.57	5.36222	0	0.08506	2	0
60220	U1343E-25H-4 W, 16.0--18.0 cm	231.26	886.95943	33.12	4.85970		0.09454	0	0
60221	U1343E-25H-4 W, 23.0--25.0 cm	231.33	887.26916	32.01	3.38287		0.06197	2	2
60222	U1343E-25H-4 W, 30.0--32.0 cm	231.40	887.57890	35.46	3.36655	0.5	0.04415	1	0
60223	U1343E-25H-4 W, 37.0--39.0 cm	231.47	887.88863	33.16	3.43126	0	0.04690	0	0
60225	U1343E-25H-4 W, 52.0--54.0 cm	231.62	888.55235	40.02	3.25982		0.05317	0	0
60226	U1343E-25H-4 W, 62.0--64.0 cm	231.72	888.99483	32.17	2.43915		0.03930	0	1
60227	U1343E-25H-4 W, 68.0--70.0 cm	231.78	889.26031	32.03	2.99381	0.5	0.01028	0	0
60228	U1343E-25H-4 W, 77.0--79.0 cm	231.87	889.65854	40.54	3.64637	0.5	0.07469	2	0
60229	U1343E-25H-4 W, 86.0--88.0 cm	231.96	890.05677	35.65	2.35609		0.02215	1	0
60231	U1343E-25H-4 W, 102.0--104.0 cm	232.12	890.76474	32.46	1.79374		0.02563	0	0
60232	U1343E-25H-4 W, 109.0--111.0 cm	232.19	891.07447	38.62	2.46178		0.02011	0	2
60233	U1343E-25H-4 W, 118.0--120.0 cm	232.28	891.47270	30.68	1.81495	0	0.02052	1	1
60234	U1343E-25H-4 W, 126.0--128.0 cm	232.36	891.82669	36.29	2.61233		0.02203	0	0
60235	U1343E-25H-4 W, 134.0--136.0 cm	232.44	892.18067	32.34	1.94892		0.03959	0	0
60237	U1343E-25H-5 W, 8.0--10.0 cm	232.68	893.24262	32.72	2.26240		0.04251	1	0
60238	U1343E-25H-5 W, 16.0--18.0 cm	232.76	893.59660	37.88	3.16642	1	0.03846	1	0
60239	U1343E-25H-5 W, 23.0--25.0 cm	232.83	893.90633	34.26	2.87225		0.01432	1	1
60240	U1343E-25H-5 W, 30.0--32.0 cm	232.90	894.21607	37.81	2.96008		0.01899	0	1
60241	U1343E-25H-5 W, 37.0--39.0 cm	232.97	894.52580	34.24	2.88054		0.02883	0	0
60242	U1343E-25H-5 W, 45.0--47.0 cm	233.05	894.87978	29.18	2.40851	1	0.03839	0	0
60244	U1343E-25H-5 W, 62.0--64.0 cm	233.22	895.63200	37.81	4.10454		0.00884	1	0

60245	U1343E-25H-5 W, 68.0--70.0 cm	233.28	895.89748	40.26	3.67016		0.03504	0	0
60246	U1343E-25H-5 W, 77.0--79.0 cm	233.37	896.29571	34.94	4.16489		0.04169	0	0
60247	U1343E-25H-5 W, 86.0--88.0 cm	233.46	896.69394	39.77	5.15355	1	0.10833	0	0
60248	U1343E-25H-5 W, 96.0--98.0 cm	233.56	897.13642	33.37	3.31721		0.05622	0	0
60249	U1343E-25H-5 W, 102.0--104.0 cm	233.62	897.40191	33.84	3.00091		0.03675	1	0
60251	U1343E-25H-5 W, 118.0--120.0 cm	233.78	898.10987	37.85	3.45855		0.05216	0	0
60252	U1343E-25H-5 W, 126.0--128.0 cm	233.86	898.46385	32.19	3.40069	1	0.06683	1	1
60253	U1343E-25H-5 W, 132.0--134.0 cm	233.92	898.72934	33.45	3.11080		0.11991	0	1
60254	U1343E-25H-6 W, 0.0--2.0 cm	234.10	899.52580	36.29	3.28630		0.07545	0	0
60256	U1343E-25H-6 W, 16.0--18.0 cm	234.26	900.23377	35.51	3.48770		0.05923	2	0
60257	U1343E-25H-6 W, 23.0--25.0 cm	234.33	900.54350	39.78	3.74791	0.5	0.06298	0	0
60258	U1343E-25H-6 W, 30.0--32.0 cm	234.40	900.85323	35.68	3.09694		0.03006	1	0
60259	U1343E-25H-6 W, 37.0--39.0 cm	234.47	901.16297	39.32	3.36289		0.04928	0	0
60260	U1343E-25H-6 W, 46.0--48.0 cm	234.56	901.56120	27.95	2.64282		0.07634	1	1
60261	U1343E-25H-6 W, 54.0--56.0 cm	234.64	901.91518	42.26	3.43090	1	0.07393	0	0
60263	U1343E-25H-6 W, 68.0--70.0 cm	234.78	902.53465	36.33	3.57923		0.14891	3	2
60264	U1343E-25H-6 W, 77.0--79.0 cm	234.87	902.93288	38.75	4.49577		0.20197	3	0
60265	U1343E-25H-6 W, 86.0--88.0 cm	234.96	903.33111	31.87	2.80294		0.05483	0	2
60266	U1343E-25H-6 W, 96.0--98.0 cm	235.06	903.77359	34.88	3.07968	0.5	0.04484	1	2
60267	U1343E-25H-6 W, 102.0--104.0 cm	235.12	904.03908	34.46	3.19018		0.05794	0	0
60269	U1343E-25H-6 W, 118.0--120.0 cm	235.28	904.74704	23.09	2.25057		0.03077	0	0
60270	U1343E-25H-6 W, 126.0--128.0 cm	235.36	905.10102	36.17	3.86745	1	0.03886	0	0

60271	U1343E-25H-6 W, 134.0--136.0 cm	235.44	905.45500	34.56	4.72298		0.10806	1	0
60272	U1343E-25H-6 W, 143.0--145.0 cm	235.53	905.85323	35.27	4.15929		0.16089	0	3
60273	U1343E-25H-7 W, 0.0--2.0 cm	235.60	906.16297	28.01	3.64043		0.06091	0	0
60274	U1343E-25H-7 W, 8.0--10.0 cm	235.68	906.51695	30.02	2.88906	0.5	0.06495	1	0
60276	U1343E-25H-7 W, 23.0--25.0 cm	235.83	907.18067	38.37	4.38971		0.11445	2	0
60277	U1343E-25H-7 W, 30.0--32.0 cm	235.90	907.49040	34.59	5.31600		0.11337	2	0
60278	U1343E-25H-7 W, 37.0--39.0 cm	235.97	907.80014	31.69	3.37383		0.03752	0	1
60279	U1343E-25H-7 W, 46.0--48.0 cm	236.06	908.19837	35.33	3.30637	0.5	0.05952	1	2
60280	U1343E-25H-7 W, 52.0--54.0 cm	236.12	908.46385	29.02	2.99381		0.03530	1	0
60281	U1343E-25H-7 W, 62.0--64.0 cm	236.22	908.90633	36.77	3.42064		0.07807	0	0
60283	U1343E-25H-7 W, 77.0--79.0 cm	236.37	909.57005	34.33	2.65864		0.06015	0	0
60284	U1343E-25H-7 W, 86.0--88.0 cm	236.46	909.96828	37.44	2.75048	0.5	0.09302	0	0
60285	U1343E-25H-7 W, 96.0--98.0 cm	236.56	910.41076	31.93	1.81963		0.05600	0	0
60286	U1343E-25H-7 W, 102.0--104.0 cm	236.62	910.67624	35.01	1.88965		0.10478	0	0

APPENDIX C

DATA FOR THE COUNTS OF COARSE
FRACTION COMPONENTS

MPA reference #	IODP Expedition 323 Site U1343 Sample Source	Depth (m ccsf)	Sev Kender Age Model (ka)	Count Data: 250<<2000 um (#)	Biogenics	Plant Material	Burrows	Pyrite	Sediment Clumps	Pyroclastics	Chert	Gauconite	Feldspar	Quartz	Mica	Unknown minerals	Felsic Lithics	Mafic Lithics	Total Count (#)
60168	U1343C-23H-5 W, 86.0--88.0 cm	227.88	871.986664		11	0	0	0	2	9	0	6	56	49	1	1	21	50	206
60169	U1343C-23H-6 W, 0.0--2.0 cm	227.97	872.384894		25	1	0	0	43	3	0	8	24	60	0	1	18	33	216
60170	U1343C-23H-6 W, 8.0--10.0 cm	228.05	872.738876		30	1	1	1	28	8	0	5	31	46	0	0	28	34	213
60171	U1343C-23H-6 W, 16.0--18.0 cm	228.13	873.092858		27	0	1	0	14	3	0	10	31	71	0	1	17	29	204
60172	U1343C-23H-6 W, 23.0--25.0 cm	228.20	873.402593		15	0	4	2	32	4	0	8	32	45	0	3	24	35	204
60173	U1343C-23H-6 W, 30.0--32.0 cm	228.27	873.712327		24	0	0	0	64	7	0	2	25	56	0	1	10	29	218
60175	U1343C-23H-6 W, 52.0--54.0 cm	228.49	874.685779		184	0	2	0	2	3	0	4	20	37	0	1	17	44	314
60176	U1343C-23H-6 W, 62.0--64.0 cm	228.59	875.128257		5	0	0	0	109	4	0	1	18	35	2	1	9	17	201
60177	U1343C-23H-6 W, 68.0--70.0 cm	228.65	875.393743		4	0	3	0	13	16	0	6	31	60	0	1	31	42	207
60178	U1343C-23H-6 W, 77.0--79.0 cm	228.74	875.791973		3	0	0	0	9	12	0	1	46	95	1	1	15	31	214
60179	U1343C-23H-6 W, 86.0--88.0 cm	228.83	876.190204		22	1	1	2	39	11	1	7	24	38	0	6	14	36	202
60181	U1343C-23H-6 W, 102.0--104.0 cm	228.99	876.898168		12	0	0	0	3	17	0	2	30	72	0	3	32	30	201
60182	U1343C-23H-6 W, 109.0--111.0 cm	229.06	877.207903		13	0	6	2	103	10	0	3	14	25	0	4	8	15	203
60183	U1343C-23H-6 W, 118.0--120.0 cm	229.15	877.606133		53	0	2	1	22	7	0	8	26	49	0	2	19	39	228
60184	U1343C-23H-6 W, 126.0--128.0 cm	229.23	877.960115		74	0	0	0	0	2	0	3	25	54	0	1	19	29	207
60185	U1343E-25H-2 W, 0.0--2.0 cm	228.10	872.977128		24	2	13	0	28	2	0	5	28	50	0	1	28	27	208
60186	U1343E-25H-2 W, 8.0--10.0 cm	228.18	873.331111		22	0	5	2	29	1	0	8	37	56	0	2	19	24	205
60187	U1343E-25H-2 W, 16.0--18.0 cm	228.26	873.685093		16	3	5	1	79	0	0	2	24	33	0	10	15	15	203
60188	U1343E-25H-2 W, 23.0--25.0 cm	228.33	873.994827		21	1	1	0	123	4	0	2	12	14	0	0	9	16	203
60189	U1343E-25H-2 W, 30.0--32.0 cm	228.40	874.304562		295	0	0	1	56	0	0	3	5	21	0	4	4	4	393
60190	U1343E-25H-2 W, 40.0--42.0 cm	228.50	874.747040		371	0	0	0	40	0	0	0	1	9	0	1	1	4	427
60191	U1343E-25H-2 W, 64.0--66.0 cm	228.74	875.808987		2	2	0	0	5	16	0	5	41	62	0	12	41	42	228
60192	U1343E-25H-2 W, 77.0--79.0 cm	228.87	876.384208		4	0	2	0	20	11	0	6	41	74	0	3	22	38	223
60193	U1343E-25H-2 W, 86.0--88.0 cm	228.96	876.782438		21	0	3	2	26	9	0	10	29	50	0	2	21	44	217
60194	U1343E-25H-2 W, 94.0--96.0 cm	229.04	877.136420		7	0	3	0	63	2	0	3	33	45	0	6	17	30	209
60195	U1343E-25H-2 W, 102.0--104.0 cm	229.12	877.490403		21	1	5	1	45	9	0	8	28	43	0	4	22	39	226
60196	U1343E-25H-2 W, 109.0--111.0 cm	229.19	877.800137		28	0	1	0	10	15	0	5	32	59	2	2	29	28	211
60197	U1343E-25H-2 W, 118.0--120.0 cm	229.28	878.198367		43	0	0	1	2	9	0	12	38	43	0	3	18	43	212
60198	U1343E-25H-2 W, 126.0--128.0 cm	229.36	878.552350		59	0	0	0	4	2	0	7	20	55	0	2	24	32	205
60200	U1343E-25H-3 W, 0.0--2.0 cm	229.60	879.614296		13	0	0	0	16	19	0	8	28	55	0	1	24	40	204
60201	U1343E-25H-3 W, 8.0--10.0 cm	229.68	879.968279		26	0	7	1	34	7	0	2	20	56	0	4	37	26	220
60202	U1343E-25H-3 W, 16.0--18.0 cm	229.76	880.322261		9	0	9	3	76	9	0	3	18	30	0	1	17	29	204
60203	U1343E-25H-3 W, 23.0--25.0 cm	229.83	880.631996		22	2	1	0	67	5	0	4	13	53	0	1	16	23	207
60204	U1343E-25H-3 W, 30.0--32.0 cm	229.90	880.941730		3	0	0	1	45	9	0	6	31	49	0	3	32	35	214
60206	U1343E-25H-3 W, 46.0--48.0 cm	230.06	881.649695		18	1	1	0	16	37	0	4	18	52	0	1	43	30	221
60207	U1343E-25H-3 W, 52.0--54.0 cm	230.12	881.915181		17	0	0	0	16	59	0	3	25	29	0	2	30	22	203
60208	U1343E-25H-3 W, 62.0--64.0 cm	230.22	882.357659		2	0	0	0	10	25	0	8	13	57	0	0	52	35	205
60209	U1343E-25H-3 W, 68.0--70.0 cm	230.28	882.623146		4	1	0	0	12	20	0	9	42	39	1	5	35	40	208
60210	U1343E-25H-3 W, 77.0--79.0 cm	230.37	883.021376		6	2	1	0	18	11	0	8	23	55	0	1	47	33	205

60212	U1343E-25H-3 W, 96.0--98.0 cm	230.56	883.862084		21	0	3	1	3	1	0	13	41	48	1	3	30	39	204
60213	U1343E-25H-3 W, 102.0--104.0 cm	230.62	884.127571		7	1	1	0	12	7	2	7	28	60	0	5	50	27	207
60214	U1343E-25H-3 W, 109.0--111.0 cm	230.69	884.437305		7	0	4	0	46	4	1	7	32	37	0	4	27	33	202
60215	U1343E-25H-3 W, 118.0--120.0 cm	230.78	884.835535		6	2	0	0	42	7	0	3	16	46	0	1	33	45	201
60216	U1343E-25H-3 W, 126.0--128.0 cm	230.86	885.189518		2	1	6	0	38	6	0	7	36	50	0	0	47	27	220
60218	U1343E-25H-4 W, 0.0--2.0 cm	231.10	886.251465		9	0	1	0	5	12	0	4	29	42	0	2	51	50	205
60219	U1343E-25H-4 W, 8.0--10.0 cm	231.18	886.605447		0	0	3	0	45	16	0	9	27	39	0	0	37	25	201
60220	U1343E-25H-4 W, 16.0--18.0 cm	231.26	886.959429		5	0	12	27	59	1	0	22	5	53	1	14	5	0	204
60221	U1343E-25H-4 W, 23.0--25.0 cm	231.33	887.269164		32	1	10	0	21	6	0	8	25	45	0	2	29	25	204
60222	U1343E-25H-4 W, 30.0--32.0 cm	231.40	887.578898		36	0	0	0	7	7	0	5	18	47	0	1	35	44	200
60223	U1343E-25H-4 W, 37.0--39.0 cm	231.47	887.888633		24	0	0	0	2	12	0	7	19	45	0	2	44	52	207
60225	U1343E-25H-4 W, 52.0--54.0 cm	231.62	888.552350		10	0	1	0	36	7	0	14	29	34	2	3	41	36	213
60226	U1343E-25H-4 W, 62.0--64.0 cm	231.72	888.994827		58	0	8	6	81	6	0	2	14	14	0	1	9	12	211
60227	U1343E-25H-4 W, 68.0--70.0 cm	231.78	889.260314		66	0	10	0	48	2	0	4	16	17	0	4	22	14	203
60228	U1343E-25H-4 W, 77.0--79.0 cm	231.87	889.658544		16	0	3	0	93	6	0	2	17	11	2	0	34	20	204
60229	U1343E-25H-4 W, 86.0--88.0 cm	231.96	890.056774		31	2	8	0	15	2	1	12	35	41	0	4	26	46	223
60231	U1343E-25H-4 W, 102.0--104.0 cm	232.12	890.764739		26	0	24	15	25	7	0	2	19	27	1	2	42	22	212
60232	U1343E-25H-4 W, 109.0--111.0 cm	232.19	891.074473		29	2	9	4	67	1	0	5	8	23	1	2	28	23	202
60233	U1343E-25H-4 W, 118.0--120.0 cm	232.28	891.472704		34	0	0	0	3	1	0	7	27	41	1	2	52	35	203
60234	U1343E-25H-4 W, 126.0--128.0 cm	232.36	891.826686		31	1	2	1	11	1	0	6	32	38	0	1	36	46	206
60235	U1343E-25H-4 W, 134.0--136.0 cm	232.44	892.180668		22	0	1	0	107	4	1	4	10	17	1	1	14	25	207
60237	U1343E-25H-5 W, 8.0--10.0 cm	232.68	893.242615		22	0	10	4	118	0	0	4	10	15	0	1	15	15	214
60238	U1343E-25H-5 W, 16.0--18.0 cm	232.76	893.596597		20	5	3	0	14	4	0	6	35	34	0	3	44	32	200
60239	U1343E-25H-5 W, 23.0--25.0 cm	232.83	893.906332		27	0	0	0	1	3	0	6	40	40	1	5	51	31	205
60240	U1343E-25H-5 W, 30.0--32.0 cm	232.90	894.216066		17	1	10	3	23	3	0	7	30	27	2	5	52	22	202
60241	U1343E-25H-5 W, 37.0--39.0 cm	232.97	894.525801		33	3	0	0	0	1	0	4	66	39	3	5	37	31	222
60242	U1343E-25H-5 W, 45.0--47.0 cm	233.05	894.879783		34	6	3	1	10	2	0	5	25	38	1	3	52	29	209
60244	U1343E-25H-5 W, 62.0--64.0 cm	233.22	895.631996		22	4	2	0	4	0	0	2	15	11	3	1	16	15	95
60245	U1343E-25H-5 W, 68.0--70.0 cm	233.28	895.897482		23	2	0	1	6	3	0	11	33	27	4	15	59	34	218
60246	U1343E-25H-5 W, 77.0--79.0 cm	233.37	896.295712		23	1	0	0	0	1	0	4	42	44	1	6	46	35	203
60247	U1343E-25H-5 W, 86.0--88.0 cm	233.46	896.693942		26	1	5	4	181	2	1	4	14	16	7	2	17	21	301
60248	U1343E-25H-5 W, 96.0--98.0 cm	233.56	897.136420		15	1	0	1	2	2	0	0	37	39	3	4	53	45	202
60249	U1343E-25H-5 W, 102.0--104.0 cm	233.62	897.401907		40	1	0	0	0	2	0	5	29	37	1	1	41	47	204
60251	U1343E-25H-5 W, 118.0--120.0 cm	233.78	898.109872		14	1	1	1	40	2	0	1	27	36	1	1	52	30	207

APPENDIX D

DATA FOR QUARTZ GRAIN CHARACTERISTICS

Age of Sample Source (ka)	grain #	Sphericity: HS) 1:High LS) 2:Low	Angularity: WR 1: well-rounded RN 2: rounded SR 3: sub-rounded SA 4: sub-angular AN 5: angular VA 6 : very angular	Surface Freshness: AL 1: altered AM 2: altered>fresh AF 3: altered=fresh FM 4: altered<fresh FR 5:fresh
859.8	1	not qtz		
859.8	2	1	2	1
859.8	3	1	6	5
859.8	4	2	3	1
859.8	5	2	5	1
859.8	6	1	5	5
859.8	7	1	5	5
859.8	8	1	6	5
859.8	9	2	6	3
859.8	10	1	5	5
859.8	11	1	5	4
859.8	12	1	5	5
859.8	13	1	4	5
859.8	14	2	5	3
859.8	15	2	5	5
859.8	16	1	4	3
859.8	17	2	4	3
859.8	18	1	5	3
859.8	19	1	5	3
859.8	20	2	5	5
859.8	21	1	5	5
859.8	22	2	5	5
859.8	23	1	3	1
859.8	24	1	4	4
864.2	1	2	6	5
864.2	2	1	5	1
864.2	3	1	6	5
864.2	4	1	5	3
864.2	5	1	5	5
864.2	6	2	4	1
864.2	7	1	4	3
864.2	8	2	6	5
864.2	9	1	5	5
864.2	10	1	4	1
864.2	11	1	4	1
864.2	12	1	5	4

864.2	13	2	5	2
864.2	14	1	5	2
864.2	15	not quartz		
864.2	16	1	3	1
864.2	17	1	3	1
864.2	18	2	5	3
864.2	19	2	5	1
864.2	20	not quartz		
864.2	21	2	5	2
864.2	22	1	5	3
864.2	23	1	5	4
864.2	24	2	4	4
864.2	25	1	6	5
864.2	26	1	3	1
873.3	1	1	5	5
873.3	2	2	4	3
873.3	3	1	5	4
873.3	4	2	4	2
873.3	5	1	5	5
873.3	6	2	3	1
873.3	7	2	5	4
873.3	8	2	2	1
873.3	9	1	3	1
873.3	10	2	6	4
873.3	11	1	5	2
873.3	12	2	4	5
873.3	13	2	5	5
873.3	14	not quartz		
873.3	15	1	5	1
873.3	16	2	6	1
873.3	17	1	4	1
873.3	18	2	4	4
873.3	19	2	5	2
873.3	20	1	4	4
873.3	21	1	3	2
873.3	22	1	6	5
873.3	23	1	3	2
873.3	24	1	3	1
873.3	25	1	2	1
873.3	26	2	3	2
873.3	27	2	4	3
877.1	1	1	3	1

877.1	2	not quartz		
877.1	3	2	5	4
877.1	4	2	5	2
877.1	5	2	5	3
877.1	6	not quartz		
877.1	7	2	3	1
877.1	8	1	4	2
877.1	9	2	6	4
877.1	10	2	6	5
877.1	11	not quartz		
877.1	12	2	5	2
877.1	13	1	5	4
877.1	14	1	3	2
877.1	15	1	3	1
877.1	16	1	4	3
877.1	17	2	4	1
877.1	18	not quartz		
877.1	19	1	6	5
877.1	20	1	5	1
877.1	21	biogenic		
877.1	22	1	3	1
877.1	23	not quartz		
877.1	24	2	2	2
877.1	25	2	5	3
877.1	26	1	5	4
880.9	1	1	2	1
880.9	2	2	5	3
880.9	3	2	5	3
880.9	4	1	5	3
880.9	5	2	4	1
880.9	6	1	5	3
880.9	7	1	5	3
880.9	8	1	3	2
880.9	9	not quartz		
880.9	10	1	5	2
880.9	11	2	5	4
880.9	12	2	5	1
880.9	13	not quartz		
880.9	14	1	5	5
880.9	15	2	4	1
880.9	16	1	5	4
880.9	17	1	4	1
880.9	18	1	2	1

880.9	19	1	4	2
880.9	20	2	5	1
880.9	21	1	5	2
880.9	22	2	4	2
880.9	23	1	5	4
880.9	24	2	5	4
880.9	25	2	5	5
880.9	26	1	4	1
880.9	27	1	5	3
894.9	1	2	2	1
894.9	2	2	6	5
894.9	3	1	6	2
894.9	4	2	2	1
894.9	5	1	5	1
894.9	6	2	5	5
894.9	7	1	5	3
894.9	8	2	2	1
894.9	9	2	3	1
894.9	10	2	3	1
894.9	11	2	4	1
894.9	12	1	3	1
894.9	13	1	2	1
894.9	14	not quartz		
894.9	15	2	5	4
894.9	16	2	6	5
894.9	17	1	4	2
894.9	18	2	4	1
894.9	19	1	4	3
894.9	20	1	5	2
894.9	21	2	5	1
894.9	22	2	5	5
894.9	23	1	5	1
894.9	24	1	5	1
894.9	25	not quartz		
902.5	1	1	2	1
902.5	2	1	5	2
902.5	3	1	2	1
902.5	4	2	2	1
902.5	5	1	2	2
902.5	6	2	2	1
902.5	7	1	5	1
902.5	8	1	5	5

902.5	9	1	3	1
902.5	10	2	2	1
902.5	11	not quartz		
902.5	12	2	5	3
902.5	13	2	4	4
902.5	14	2	2	1
902.5	15	1	5	1
902.5	16	not quartz		
902.5	17	1	2	1
902.5	18	2	6	4
902.5	19	1	3	3
902.5	20	1	5	3
902.5	21	2	5	4
902.5	22	1	4	2
902.5	23	1	3	4
902.5	24	2	5	5
902.5	25	2	2	2
902.5	26	2	2	1
902.5	27	2	5	1
902.5	28	2	5	1
902.5	29	2	5	1
902.5	30	2	5	1
902.5	31	not quartz		
902.5	32	1	5	2
902.5	33	not quartz		
902.5	34	1	6	3
902.5	35	2	2	1
908.9	1	1	3	1
908.9	2	not quartz		
908.9	3	2	4	3
908.9	4	1	5	1
908.9	5	not quartz		
908.9	6	1	4	1
908.9	7	2	5	2
908.9	8	1	4	1
908.9	9	1	5	3
908.9	10	1	3	1
908.9	11	2	2	1
908.9	12	not quartz		
908.9	13	not quartz		
908.9	14	1	2	1
908.9	15	2	2	1
908.9	16	2	2	1

908.9	17	1	5	2
908.9	18	1	3	1
908.9	19	2	3	1
908.9	20	1	4	1
908.9	21	1	2	2
908.9	22	1	3	2
908.9	23	not quartz		
908.9	24	2	4	4
908.9	25	2	3	1
908.9	26	1	5	1
908.9	27	2	3	1
908.9	28	2	4	2
908.9	29	2	4	1
908.9	30	not quartz		
908.9	31	2	3	1
908.9	32	not quartz		
908.9	33	2	5	1